High Contrast Nanophotonics for Scalable Photovoltaics and Solar Fuels

Thesis by

Haley C. Bauser

In Partial Fulfillment of the Requirements for
the Degree of
Doctor of Philosophy

CALIFORNIA INSTITUTE OF TECHNOLOGY
Pasadena, California

2022
(Defended March 1st, 2022)

Haley C. Bauser
ORCID: 0000-0002-9677-3301

ACKNOWLEDGEMENTS

Completing this work has been equally challenging and rewarding and has been made immeasurably better by all the colleagues, family, and friends who have supported me along the way. In this section, I intend to fully acknowledge everyone in my support system to show appreciation that I am not always the best at expressing. First, I would like to express my gratitude to my advisor Harry Atwater. In academia, it is easy to become cynical, but Harry remains unceasingly optimistic and passionate. I also admire his inability to be complacent, inspiring all of us to think big about the work we do and the directions we can go. However, most importantly, Harry has created a great and supportive lab environment. I am endlessly thankful for the opportunity to work in his group and for the trust he put in me as a researcher.

I have been very fortunate to work with the lovely LSC team. Thank you first to David Needell who I have spent my entire time at Caltech working with. We've been through it all together from tech booths next to an open bar and getting to present our research in Hawaii, to soul-crushing defeats of having a module break less than 12 hours before flying to CO for testing. I have never collaborated with someone with a more different brain than mine, and I am so grateful that we had the opportunity to work together. I would not have the success in research that I have had without Colton Bukowsky. I am so lucky that you took the time to help me fully learn and understand the world of photonic crystals. Thank you for taking the time to teach me everything about photonic crystals and helping me carve my niche in the LSC world. Megan Phelan has been an amazing friend and collaborator to have on the LSC project. I appreciate all of her encouragement and that she never makes fun of me for all the dumb big picture questions I ask her. Maggie Potter and I have been best LSC clean room pals, and I'm very happy we were able to work together for the last few years of your PhD. I am delighted to pass over the torch on all this work to Catherine Ryczek, who is going to do an absolutely kick ass job bringing these projects over the finish line. Thank you to Mike Deceglie, John Geisz, San Theingi, Brett Koscher, Zach Nett, Hanxiao Su, Pauls Stradins, and Paul Alivisatos for all their contributions to the LSC project. Thank you also to my committee members Oskar Painter, Stevan Nadj-Perge, and Austin Minnich.

I would like to acknowledge everyone who has helped me with measurements, fabrication, and insightful conversations. Thank you Morgan Foley, Souvik Biswas, Magel Su, Pilar Espinet-Gonzalez, Mike Kelzenberg, Cora Went, Alex Welch, Benjamin Vest, Yongwhi Kim, and Lucy Li. I would specifically like to highlight Phil Jahelka, Colton Bukowsky, Ryan Ng, and Claudio Hail, who all gave more time that I deserved to help me with troubleshooting, problem solving, and to just generally give great advice. I have tried my best to continue the spirit of mentorship that they have graced me with. I am grateful for the large community of women in the Atwater group. My time would not have been the same without Ladies Night with Lucy Li, Alex Welch, Melissa Li, Prachi Thureja, Megan Phelan, Aisulu Aitbekova, Rebecca Glaudell, Cora Went, Dagny Fleishman, Kelly Mauser, Y-Rung Lin, and Sophia Cheng.

I spent nearly all of my time at Caltech in the Kavli Nanoscience Institute. None of my work would be possibly without their facilities and equipment. Thank you to Guy DeRose, Nathan Lee, Matt Hunt, Bert Mendoza, Kelly McKenzie and Alireza Ghaffari for training me and keeping the lab running smoothly. I specifically want to thank Alex Wertheim, the ultimate deposition guru of the KNI. Alex was the first person to train me on pretty much anything and knows basically everything. Thank you for always being game to discuss fabrication tips and tricks. Lastly thank you to Tiffany Kimoto, Kam Flower, Johnathan Gross, Jennifer Blankenship, and Christy Jenstad for handling literally everything and keeping someone as scatterbrained as me on the right track. Thank you to the Caltech CCID staff for your continued work in making Caltech a better and more equitable place. I've learned a lot from the staff and students I met through the CCID.

I don't necessarily subscribe to the belief that people are destined for a certain career. However, I do know that for much of my life, there was zero chance I would have any sort of career in science. I took physics in high school because I had to and was so scared of both the material and the teacher, Charles S. Merriam II. I struggle to think of anyone who has changed the trajectory as significantly as Mr. Merriam did. I tried to drop out of physics and math multiple times in high school because it did not come easily for me. Mr. Merriam never let me. One year when I was on break from college, I went to visit him and he told me he did not let girls drop out of his class, and was certainly never going to let me no matter how many times I asked. He somehow saw something in me that I did not know was there. He always expected and pushed for the best from me and even recruited me onto the engineering team my senior year. He also always checked on me and my family during a time when I very much needed people who cared. I would not have gotten a scholarship to college without him. I would not have majored in physics without him. I would not be myself without him. I could honestly write a whole thesis about his influence on my life, but I will simply say thank you because no words will ever suffice. I so badly wish he could be here to see how it all worked out, but I am so grateful he was able to see his impact and know that because of him I was going to get a PhD in Applied Physics.

Professor Irina Novikova welcomed me into her lab my sophomore year of college. Under her guidance, physics went from "the most tolerable science class" to an actual career that I am excited to pursue. I spent three years in her research lab learning all about the fascinating world of quantum information and table top optics. Through working with Irina, I discovered my passion for research. Irina is a brilliant researcher and I am so lucky that I got to learn from her. She encouraged me and promoted my work consistently, and without her, I would not be pursuing a PhD. I am grateful for all of her wisdom and encouragement and am happy we still keep in touch. I am additionally grateful for my REU advisors Paola Barbara, Xinran Zhang, and Stephen Forrest.

I do not know how I became so fortunate to have such an incredible support system. Thank you to my parents Charlotte Bauser and Larry Lewis who have always encouraged me to pursue whatever I want. I know that I can always rely on them for anything and everything even when they're 3000 miles away. Thank you to the Mazzas, Janice, Tom, Genny, and Tommy for your support over the years. Through your continued kindness, I've never felt too far from family. Thank you to my friends Cora Went, Emily Wyatt, Natalie Bernat, Chris Tang, Sarah Beery, and Cary Wilton for your friendship throughout my time at Caltech. Long live Grad Prom. Thank you to Azhar Carim for being my ride or die. Thank you to Sisir Yalamanchili, Fadl Saadi, Katie Hamman, and Sophia Cheng for many Bar Zar nights. Thank you to Matt Heffernan and Eve Chase for being my physics friends since college. It's been a wild ride for all of us together, and I celebrate all of our successes. Thank you to Li-Hsueh Lu, Yohance Whitaker, and Claire Penix for your lifelong friendship. I would not have mentally survived from 2020 onward without Jake Evans, Zach Ifkovits, Elizabeth Littlefield, Christian Goodnow, and Madeline Meier. What started as a group of people meeting up to watch The Bachelor turned into my greatest and most reliable support system. I am so lucky to call you all my friends.

Most importantly, I am eternally grateful to Michael Mazza. Whether we're seeing the Grand Canyon for the first time, keeping our "one concert per month" streak, cruising Ventura Blvd. searching for the grossest things at each liquor store, watching every single Dodger game, getting burritos from Cactus after a morning movie at Arclight (RIP), or just cooking a meal together after a bad lab day, we can make anything fun as long as we're together. Thank you for your kindness, brilliance, unwavering belief, encouragement, and for being my best friend. You are the most supportive person I know and I am unbelievably fortunate to have you in my life.

ABSTRACT

Anthropogenic climate change is a massive threat to our planet's stability and habitability. Carbon dioxide makes up the majority of the greenhouse gas emissions leading to rising global temperatures. In order to reduce the global temperature, it is imperative to reduce dependency on fossil fuels by mass adaptation of renewable energy with net-zero carbon emissions. In this work, we present designs to convert incident solar energy to power through scalable nanophotonic systems.

We first introduce a tandem luminescent solar concentrator (LSC). LSCs are of interest due to their ability to concentrate both direct and diffuse light expanding the regions in which LSCs can be deployed. The tandem LSC uses a novel architecture in which InGaP micro-cells lie co-planar and optically coupled to the waveguide as opposed to the traditional edge-lined LSC. The waveguide consists of highly efficient CdSe/CdS quantum dots with emissions tuned to the band edge of the InGaP cells. This LSC is then coupled to a Si sub-cell allowing the tandem LSC to effectively convert a greater portion of the incident solar spectrum. We fabricate and perform outdoor testing on the first co-planar tandem LSC demonstrating a path to high efficiency LSCs.

We then introduce two methods to more efficiently trap light within the LSC. The first is a high contrast grating spectrally selective reflector. By using a high contrast grating, we can achieve high reflectivity with a single layer of high index materially patterned at a sub-wavelength scale on a low index substrate. While we explore both AlSb and a-SiC:H as grating materials, we pursue a-SiC:H and fabricate such a spectrally selective reflector with over 94% reflectivity at 642 nm. We then move to eliminate the need for spectrally selective filters by using photonic crystal waveguides to trap quantum dot emission within the LSC. We present two designs in which over 90% of emission remains trapped in the photonic crystal waveguide and is therefore able to travel to the photovoltaic material. We demonstrate how such a design can be used for LSCs in terrestrial and space solar power applications.

Lastly, we expand on the photonic crystal waveguide and introduce a thermal concentrator for production of scalable solar fuels. The thermal concentrator absorbs incident sunlight and traps the generated heat within the photonic crystal. This elevates the temperature within the thermal concentrator creating conditions under which catalytic reactions producing solar fuels can occur. We design a thermal concentrator that can heat up to 507.3 Kelvin under 1 sun illumination and 729.4 Kelvin under 3 sun illumination.

PUBLISHED CONTENT AND CONTRIBUTIONS

1. Bauser, H.C., Foley, M.D., Phelan, M.E., Weigand, W., Needell, D.R., Holman, Z.C., Atwater, H.A. “Amorphous Silicon Carbide High Contrast Gratings as Highly Efficient Spectrally Selective Visible Reflectors.” *Under Review* 2022

   H.C.B. participated in the conceptualization of the project, simulation, design, and fabrication of the samples, analysis of the results, and writing of the manuscript.

   Chapter 3 is adapted from this paper.

2. Bauser, H.C., Su, M.P., Li, X., Atwater, H.A. “Photonic Crystal Waveguides as Thermal Concentrators for Production of Scalable Solar Fuels.” *In Progress* 2022

   H.C.B. participated in the conceptualization of the project, design and simulation of the thermal concentrator, and writing of the manuscript.

   Chapter 6 is adapted from this paper.

3. Needell, D.R., Potter, M.M., Phelan, M.E., Jahelka, P.R., Bauser, H.C., Horus, D., Velarde, A., Balaji, P., Augusto, A., McDaniel, H., Geisz, J.F., Nuzzo, R.G., Atwater, H.A. “Performance Limits and Applications of Area-scalable Luminescent Solar Concentrator Photovoltaic Devices.” *Under Review* 2022

   H.C.B. participated in the conceptualization of the project, design of the samples, and writing of the manuscript.

4. Yang, F, Jha, P.K., Akbari, H., Bauser, H.C., Atwater, H.A. “A Hybrid Coupler for Directing Quantum Light Emission with High Radiative Purcell Enhancement to a Dielectric Metasurface Lens.” *Journal of Applied Physics* **2021,** 130, 163103. doi: 10.1063/5.0059012

   H.C.B. participated in the conceptualization of the project and construction of the model inputs.

5. Potter, M.M., Phelan, M.E., Balaji, P., Jahelka, P., Bauser, H.C., Glaudell, R.D., Went, C.M., Enright, M.J., Needell, D.R., Augusto, A., Atwater, H.A., Nuzzo, R.G. “Silicon Heterojunction Microcells” *ACS Applied Materials Interfaces* **2021,** 13, 38, 45600-45608. doi:10.1021/acsami.1c11122

   H.C.B. participated in the analysis and microcopy of the samples.

6. Phelan, M.E., Potter, M.M., Palaji, P., Jahelka, P.R., Bauser, H.C., Glaudell, R., Needell, D.R., Enright, M., Augusto, A., Nuzzo, R., Atwater, H.A. “Fabrication Techniques for High-performance Si Heterojunction (SHJ) Microcells.” *2021 IEEE 48th Photovoltaic Spectialists conference (PVSC)* **2021,** 0330-0334. doi: 10.1109/PVSC43889.2021.9518579

   H.C.B. participated in the analysis and microscopy of the samples.

7. Jha, P.K., Yank, F., Akbari, H., Bauser, H.C., Atwater, H.A. “Hybrid Metaphotonics for Fast and Efficient Collection of Photons from Quantum Emitters.” *OSA Optical Design and Fabrication 2021 (Flat Optics, Freeform, IODC, OFT)* **2021**, paper FTh2C.4.

   H.C.B. participated in the conceptualization of the project and construction of the model inputs.

8. Bauser, H.C., Needell, D.R., Atwater, H.A. “AlSb as a Material for High Index Contrast Nanophotonics.” *Optical Materials Express* **2021**, 11, 5, 1334-1342. doi: 10.1364/OME.422163

   H.C.B. participated in the conceptualization of the project, simulation, design, and fabrication of the samples, measurement and analysis of the results, and writing of the manuscript.

   Chapter 3 is adapted from this paper

9. Bauser, H.C., Bukowsky, C.R., Phelan, M.E., Weigand, W., Needell, D.R., Holman, Z.C., Atwater, H.A. “Luminescent Solar Concentrators with High Concentration Using Photonic Crystal Waveguides.” *Proceedings Volume 11695, High Contrast Metastructures X* **2021**, 11695, 116950H.

   H.C.B. participated in the conceptualization of the project, simulation and design of the photonic crystal waveguides, analysis of the results, and writing of the manuscript.

10. Phelan, M.E., Needell, D.R., Bauser, H.C., Su, H., Deceglie, M., Theingi, S., Kocher, B., Nett, Z., Alivisatos, A.P. “Outdoor Performance of a Tandem InGaP/Si Photovoltaic Luminescent Solar Concentrator.” *Solar Energy Materials and Solar Cells* **2021**, 223, 110945. doi: 10.1364/OME.422163

    H.C.B. participated in the conceptualization of the project, design, fabrication, and assembly of the samples, construction of the model inputs, analysis of the results, and writing of the manuscript.

    Chapter 2 is adapted from this paper

11. Bauser, H.C., Bukowsky, C.R., Phelan, M.E., Weigand, W., Needell, D.R., Holman, Z.C., Atwater, H.A. “Photonic Crystal Waveguides for >90% Light Trapping Efficiency in Luminescent Solar Concentrators.” *ACS Photonics* **2020**, 7, 8, 2122-2131. doi: 10.1364/OME.422163

    H.C.B. participated in the conceptualization of the project, simulation and design of the photonic crystal waveguides, analysis of the results, and writing of the manuscript.

    Chapter 4 is adapted from this paper

12. Lunardi, M.M., Needell, D.R., Bauser, H.C., Phelan, M.E., Atwater, H.A., Corkish, R. “Life Cycle Assessment of Tandem LSC/Si Devices.” *Energy* **2019**, 181, 1-10. doi: 10.1364/OME.422163

H.C.B. participated in the conceptualization of the project, construction of the model inputs, analysis of results, and writing of the manuscript.

13. Needell, D.R., Bauser, H.C., Phelan, M.E., Bukowsky, C.R., Ilic, O., Kelzenberg, M.D., Atwater, H.A. "Ultralight Luminescent Solar Concentrators for Space Solar Power Systems." *2019 IEEE 46th Photovoltaic Specialists Conference (PVSC)* **2019**, 2798-2801. doi:10.1364/OME.422163

    H.C.B. participated in the conceptualization of the project, construction of the model inputs, analysis of results, and writing of the manuscript.

14. Theingi, S., Needell, D.R., Bauser, H.C., Phelan, M.E., Nemeth, W., Findley, D., Su, H., Koscher, B., Nett, Z., Ilic, O., Bukowsky, C.R., Nuzzo, R., Alivisatos, A.P., Geisz, J., Stradins, P., Atwater, H.A. "Luminescent Solare Concentrator Tandem-on-Silicon with above 700mV Passivated Contact Silicon Bottom Cell." *2019 IEEE 46th Photovoltaic Specialists Conference (PVSC)* **2019**, 0747-0749. doi:10.1364/OME.422163

    H.C.B. participated in the conceptualization of the project and construction of the model inputs.

15. Needell, D.R., Bukowsky, C.R., Darbe, S., Bauser, H.C., Ilic, O., Atwater, H.A. "Spectrally Matched Quantum Dot Photoluminescence in GaAs-Si Tandem Luminescent Solar Concentrators." *IEEE Journal of Photovoltaics* **2019**, 9, 2, 397-401. doi:10.1364/OME.422163

    H.C.B. participated in the conceptualization of the project, construction of the model inputs, analysis of results, and writing of the manuscript.

16. Bauser, H.C., Needell, D.R., Bukowsky, C.R., Ilic, O., Nett, Z., Lee, B.G., Geisz, J.F., Alivisatos, A.P., Atwater, H.A. "Metasurfaces as Wavelength Selective Mirrors in Tandem Luminescent Solar Concentrators." *2018 IEEE 45th Photovoltaic Specialist Conference (PVSC)* **2018.**

    H.C.B. participated in the conceptualization of the project, simulation and design of the metasurfaces, analysis of the results, and writing of the manuscript.

17. Needell, D.R., Ilic, O., Bukowsky, C.R., Nett, Z., Xu, L., He, J., Bauser, H.C., Lee, B.G., Geisz, J.F., Nuzzo, R.G., Alivisatos, A.P., Atwater, H.A. "Design Criteria for Micro-Optical Tandem Luminescent Solar Concentrators." *IEEE Journal of Photovoltaics* **2018**, 8, 6, 1560-1567. doi:10.1364/OME.422163

    H.C.B. participated in the conceptualization of the projection and construction of the model inputs.

TABLE OF CONTENTS

LIST OF ILLUSTRATIONS

Number *Page*

LIST OF TABLES

Chapter 1

INTRODUCTION

1.1 Current Climate Landscape

Rising global temperatures pose a massive threat to the global ecosystem, national stability, and planet habitability[1-7]. Furthermore, many policy makers describe anthropogenic climate change as the greatest threat to national security[8-11]. The effects of the rapidly increasing global temperature is already visible through increasingly dangerous fire seasons in California, unprecedented snow storms in Texas, and other natural disasters both in the U.S and abroad[9, 12-14]. As shown in Figure 1.1, the NASA Goddard Center has tracked a rapid rise in global temperature over the last one hundred years[15]. Greenhouse gas emissions are responsible for much of the increase in global temperature[16-19]. Of these greenhouse gases, the most dominant is carbon dioxide (CO_2)[16].

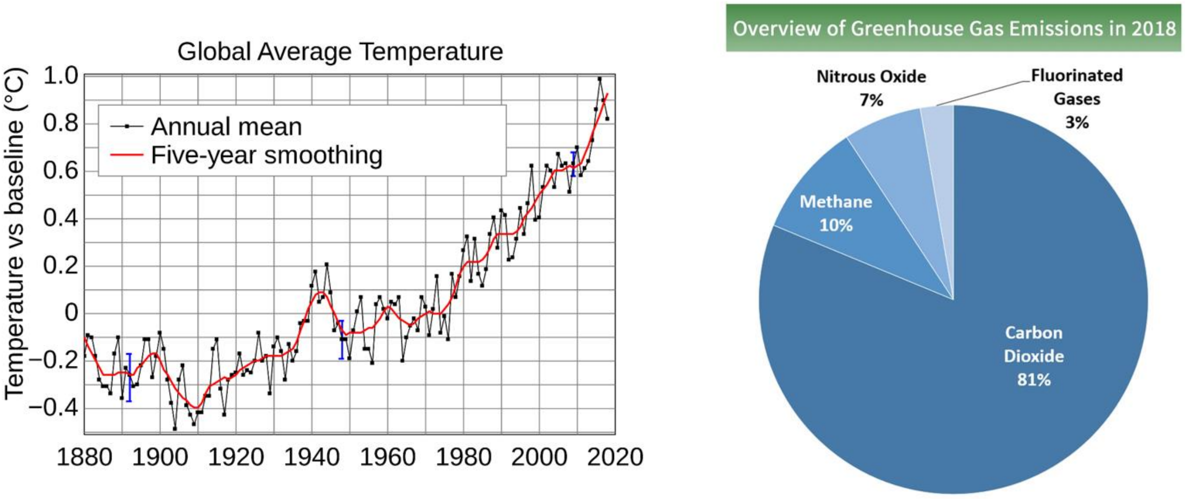

Figure 1.1: Image from the NASA Goddard Center showing the rapid increase in global temperature compared to the baseline global temperature[15]. The right panel is an overview of gases contributing to greenhouse gas emissions, courtesy of the Environmental Protection Agency[16].

In order to reduce global temperature, it is imperative that we reduce global CO_2 emissions. One such path to reduce CO_2 emissions is to reduce the global dependency on fossil fuels[19-

[22]. Alternatives to fossil fuels must be efficient, cost effective, and scalable[22]. Nanophotonic systems presented in this thesis provide a path towards scalable net-zero emission energy conversion technologies[22].

1.2 Scope of Thesis

The presented thesis contains a variety of nanophotonic contributions to technology for net-zero emission energy production. Chapter 1 will continue below where we will review some of the fundamental concepts crucial in the work comprising the remainder of the presented thesis. Chapter 2 will discuss a novel tandem luminescent solar concentrator (LSC) design. Through such a design, a photovoltaic module can more efficiently convert a greater wavelength range within the incident solar spectrum. Furthermore, LSCs provide a path towards photovoltaic technologies in diffuse environments. This chapter will cover the initial design, analysis, and prototyping of such a module.

Chapters 3 through 5 will discuss photonic concepts to improve the performance of luminescent solar concentrators. Chapter 3 will focus on the design and fabrication of a highly efficient spectrally selective high contrast grating reflector for use in the tandem luminescent solar concentrator. We first explore AlSb as a material for such a reflector. We then demonstrate how hydrogenated amorphous silicon carbide can be used to fabricate a spectrally selective filter with a reflectance of over 94% in the visible spectrum. Chapter 4 will present photonic crystal waveguides as a light trapping method for luminescent solar concentrators without the use of external reflectors. This chapter will cover design and initial fabrication for a photonic crystal waveguide tuned to trap emission at 635nm. We demonstrate that such a photonic crystal can trap over 90% of emission. Chapter 5 will expand this photonic crystal waveguide concept to extra terrestrial photovoltaic applications. This chapter will demonstrate the tunability of photonic crystal waveguides and make the case for why photonic crystal waveguides are specifically advantageous for space-based photovoltaics.

Chapter 6 will expand upon the use of light trapping photonic crystals to instead trap heat in order to provide conditions under which solar thermochemical reactions can occur to produce solar fuels. We demonstrate that thermal concentrators can be used as a medium for solar thermal catalytic reactions. By performing a reaction through such a thermal concentrator, we can achieve temperatures beyond 700 K in vacuum, and 500K in ambient. This chapter will cover an extensive theoretical study of such a thermal concentrator as well as a discussion of some initial fabrication steps. The final chapter will consist of a summary of the presented work and a discussion of potential future work and directions for each project.

Lastly, and arguable most importantly for any current graduate student reading this, the Appendix includes an adaptation of a talk on nanofabrication. In the Appendix, you will find descriptions of different systems as well as tips and tricks for various nanofabrication steps.

1.3 Conversion of Incident Sunlight as a Carbon Neutral Energy Source

The common thread through all work presented in this thesis is the pursuit of using incident sunlight for net-zero energy conversion. The incident solar spectrum is referred to as atomic mass (AM) 1.5 and accounts for the makeup of the atmosphere that hinders the full spectrum from reaching the Earth[23]. Here, we explore two primary methods of solar conversion: photovoltaics and solar thermochemical catalytic reactions. In this section, we briefly cover some of the basics of these two methods of generating renewable energy.

1.3.1 Photovoltaics

Photovoltaics is the fastest growing renewable energy conversion method due in part to a decrease in raw material cost[24]. Photovoltaics are used in residential power conversion as well as in large-scale solar farms[24,25]. Photovoltaic devices most simply convert incident solar energy directly into electricity. Such devices are most commonly made up of semiconductor material due to the importance of the photovoltaic material's internal bandgap. The semiconducting photovoltaic material uses the incident sunlight to promote electrons from the lower energy valence band to the higher energy conduction band. The excited electron can then be run through an external circuit to generate electricity. Crucial to this process is the band gap or the minimum energy required to promote an electron from its ground state to an excited state. Insulators have very wide bandgaps that make this promotion of energy nearly impossible without a very large energy source. Likewise, conductors have no bandgap and therefore electrons move freely across states limiting the potential of a driving force for the current. Semiconductors have a finite number of electrons that occupy specific energy levels and therefore the flow of electrons can be used to generate a current. The electrons will relax to thermal equilibrium unless they are continuously excited by a steady state of energy from a light source allowing a steady state of excited electrons.

Simplistically, the power generated by a solar cell is the product of the voltage and current. In order to generate electricity, the photovoltaic must have some sort of driving force to induce a current. The electromotive force needed to sustain a current is provided by an interfacing junction between two semiconducting materials. In intrinsic semiconductors, the Fermi level, or the energy at which there is a 50% probability of electron occupation, is defined as the chemical potential of the semiconducting material. In intrinsic semiconductors, the Fermi level is equidistance to the conduction and valence band. However, when you introduce defects in the semiconductor via doping, these intrinsic properties change. An n-type semiconductor has added donor states and the Fermi level is closer to the conduction band. Likewise, a p-type semiconductor has additional acceptor states and the Fermi level is closer to the valence band. When combining p-type and n-type semiconductors in a junction, an electric field forms due to the energy difference between the two semiconductors. When illuminated, a current flows through this junction. When applying an external voltage in a forward bias to the system, the Fermi level is split and quasi-Fermi levels form as the system is no longer in equilibrium which therefore increases the chemical potential. As the applied bias increases, the current flow also increases. The product of this generated current and voltage is the power output of the photovoltaic. For photovoltaics, when considering the various loss mechanisms of the solar cell, both internally (radiative recombination, thermal loss, etc.) and externally (reflection of the solar spectrum, circuit loss, etc.), the maximum theoretical efficiency for a photovoltaic is 32.9%[26]. Common, commercial single-junction Si-based photovoltaics have an efficiency of around between 15% and 20%[27]. In order to expand the applications for photovoltaic energy, it is important to create inexpensive, scalable, and efficient alternatives to expand the market beyond the current Si-based photovoltaic standard.

1.3.2 Solar Thermochemical Catalysis

Solar fuels are broadly defined as fuels that can be produced via chemical reactions that use incident sunlight as an aid in the catalytic reaction[28]. For the scope of this work, we will focus on thermochemical catalytic reactions as a method to produce solar fuels. Rather than using the incident light to excite electrons, we instead use the heat provided by the incident sunlight to produce conditions for catalytic reactions[29]. In photovoltaics, excess heat generated by incident sunlight can be damaging to the photovoltaic effect as at elevated temperatures, semiconductors are more prone to radiative recombination limiting the generation of electrons. However, the heat of incident sunlight can be quite useful for the generation of solar fuels. Fuels such as methane, ethane, hydrogen fuel, and other synthetic gases can be produced using incident sunlight and Earth abundant materials, providing a path to reduce dependency on fossil fuels[28-36]. In addition to the generation of solar fuels, we can use similar chemical reactions to sustainably produce plastics via ethylene oligomerization[37].

Many reactions using abundant materials like carbon dioxide, carbon monoxide, and nitrogen require elevated temperatures to operate[29-36]. By using incident sunlight to generate the conditions necessary for solar fuel productions, we can replace large-scale industrial production processes that typically operate under high temperatures and elevated pressures. A common way to use incident sunlight to generate temperatures required for such catalytic reactions is through a geometric concentrating system. In a geometric concentrating system, many mirrors and lenses are used to focus incident sunlight to a small area, therefore increasing the temperature at the focal point[38]. Through these types of systems, temperatures exceeding 2000 degrees Celsius can be achieved[38]. However, such systems are not scalable due to their large footprint, need for high direct solar irradiance limiting potential locations, and geometric limitations. Such high temperature concentrators need solar trackers in order to maintain the high concentration required to achieve the necessary temperatures for the catalytic reaction[38,39]. Scalable solar fuel production must operate under milder conditions and pressures while using only incident sunlight to induce the necessary conditions for catalytic solar fuel production.

1.4 Relevant Photonic Concepts

The majority of the work presented in this thesis is an analysis or demonstration of how light interacts within various mediums. It is therefore important to review some of the principle concepts in light-matter interactions. Fundamentally, light is defined as electromagnetic waves travelling in space carrying electromagnetic radient energy. Visible light refers to such waves with a wavelength from 400-700nm. In this thesis, we will be primarily considering a wavelength range from 300-1100nm which covers the electromagnetic radiation emitted by the sun available for photovoltaic energy conversion. Macroscopically, the movement and propagation of light in any medium can be evaluated by the fundamental Maxwell equations:

$$\nabla \cdot \mathrm{B}(\mathrm{r},\mathrm{t}) = 0 \tag{1.1}$$

$$\nabla \cdot D(r,t) = \rho \tag{1.2}$$

$$\nabla \times \mathrm{E}(\mathrm{r},\mathrm{t}) + \frac{\partial \mathrm{B}(\mathrm{r},\mathrm{t})}{\partial t} = 0 \tag{1.3}$$

$$\nabla \times \mathrm{H}(\mathrm{r},\mathrm{t}) - \frac{\partial \mathrm{D}(\mathrm{r},\mathrm{t})}{\partial t} = J(r,t) \tag{1.4}$$

where **D** and **B** are the displacement and magnetic induction fields, respectively, **E** and **H** are the electric and magnetic fields, and ρ and **J** are the free charge and current densities. These equations are the bases for all of the calculations and simulations for how light travels in respective mediums. When considering mixed medium through which light travels, Maxwell's equations evolve to consider the relative permittivity (ε) and permeability (μ) of the mixed medium. Permittivity is the quantification of a material's inclination to polarize and therefore store more energy. The relationship of permittivity and permeability to the displacement and magnetic induction fields is given in Equations 1.5 and 1.6, where ε_0 and μ_0 are the respective permittivity and permeability of free space and ε_r and μ_r are the permittivity and permeability in the respective medium.

$$D = \varepsilon_0\varepsilon_r \mathrm{E} \quad (1.5)$$

$$H = \frac{1}{\mu_0\mu_r}\mathrm{B} \quad (1.6)$$

With these constants defined, Maxwell's equations (Eq. 1.1-1.4) become the following:

$$\nabla \cdot \mathrm{H}(\mathrm{r},\mathrm{t}) = 0 \quad (1.7)$$

$$\nabla \cdot [\varepsilon_r E(r,t)] = \rho \quad (1.8)$$

$$\nabla \times \mathrm{E}(\mathrm{r},\mathrm{t}) + \mu_0\frac{\partial \mathrm{H}(\mathrm{r,t})}{\partial t} = 0 \quad (1.9)$$

$$\nabla \times \mathrm{H}(\mathrm{r},\mathrm{t}) - \varepsilon_0\varepsilon_r\frac{\partial \mathrm{E}(\mathrm{r,t})}{\partial t} = 0 \quad (1.10)$$

By taking the curl of Equations 1.9 and 1.10, we can achieve the classical three-dimensional wave equations given in Equations 1.11 and 1.12.

$$\nabla^2 \cdot \mathrm{E}(\mathrm{r},\mathrm{t}) = \mu_0\varepsilon_0\varepsilon_r\frac{\partial^2 \mathrm{E}(\mathrm{r,t})}{\partial t^2} \quad (1.11)$$

$$\nabla^2 \cdot \mathrm{H}(\mathrm{r},\mathrm{t}) = \mu_0\varepsilon_0\varepsilon_r\frac{\partial^2 \mathrm{H}(\mathrm{r,t})}{\partial t^2} \quad (1.12)$$

Given the complexity of solving these equations, we utilize software such as Lumerical finite-difference time-domain (FDTD) to solve Maxwell's equations to analyze how light travels within varied mixed medium systems. FDTD methods solve Maxwell's equations at various points throughout a mesh grid to give a holistic analysis of the behavior of the transverse electric (TE) and transverse magnetic (TM) modes of light.

In addition to being crucial components in the classical wave equation, the permittivity and the permeability contribute to a more intuitive photonic concept which is the index of refraction, *n*, of a material. When light travels through a medium outside of a vacuum, the index of refraction is defined in Equation 1.13.

$$n = \sqrt{\varepsilon\mu} \tag{1.13}$$

Since the materials discussed in this work are non-magnetic, this can be reduced to Equation 1.14.

$$n = \sqrt{\varepsilon} \tag{1.14}$$

The index of refraction is intuitive in that it is an optical phenomenon that most people are familiar with. We demonstrate a common visualization of how refractive index affects how light travels in Figure 1.2 using a chopstick and a glass of water. The index of refraction of air is approximately n = 1 whereas for water n = 1.3. We see that the chopstick appears to be broken when we view the portion in the water. This is because higher index of the material decreases the speed at which light travels through the higher index medium. This relation is given in Equation 1.15 where c is the speed of light, v_p is the phase velocity, k is the wavenumber, and ω is the angular frequency.

$$n = \frac{c}{v_p} = ck/\omega \tag{1.15}$$

The angle at which the chopstick appears bent can be calculated via Snell's law given in Equation 1.16

$$n_1 sin\theta_1 = n_2 sin\theta_2 \tag{1.16}$$

Figure 1.2: A demonstration of how the index of refraction affects light traveling in mixed media using a chopstick in a glass of water.

From Equation 1.16, we can derive the conditions for the phenomenon of total internal reflection (TIR) where light stays trapped within the medium. TIR can only occur within the medium that has a higher index of refraction. This condition is given below in Equation 1.17.

$$\frac{n_1}{n_2} sin\theta_1 > 1 \tag{1.17}$$

We previously defined the permittivity as the quantification of a material's ability to store energy. Therefore we can assume that materials with higher indices of fraction have a higher density of states. Therefore, light preferentially is guided into said higher density of states materials. For further reading on these concepts, see Reference 40.

1.5 Photonic Crystals

In this thesis, we will frequently discuss photonic crystal waveguides. For further reading on photonic crystals, see Reference 41. Photonic crystals are most simply structures made up of materials with alternating indices of refraction, periodic in either one, two, or three dimensions. It is therefore important to have a basic understanding of the principles of crystalline structures and periodicity. Crystalline structures are defined by their discrete translational symmetry. The translational symmetry is defined by the step length called the lattice constant, a, and the primitive lattice vector that defines the direction for the lattice constant. The primitive lattice vector can exist in one, two, or three dimensions. When considering each primitive lattice vector, we can build a primitive unit cell, defining the discrete symmetry of a crystalline structure. Electromagnetic waves travelling through such crystalline structures can be analyzed via Bloch's theorem which states that in a periodic potential, such as a crystalline structure with discrete translational symmetry, the periodic potential is in the form of a plane wave modulated by a corresponding periodic function. Equation 1.18 where r is the position, k is the wavenumber, and u is a periodic function. This periodicity is the basis by which we can analyze how light travels through photonic crystals as the function $u(r)$ shares periodicity with the crystal.

$$E_k = E_0 e^{(ik \cdot r)} \cdot u_k(r) \tag{1.18}$$

Each primitive lattice has a corresponding reciprocal lattice that can be derived from the Fourier transform. The requirement for the reciprocal lattice is given in Equation 1.19 where G is the reciprocal lattice vector, R is the lattice vector, and N is an integer.

$$G \cdot R = 2\pi N \tag{1.19}$$

From here, we can define the Brillouin zone. The Brillouin zone, rather than being defined by the wavenumber, is the primitive unit cell in the reciprocal lattice space. Figure 1.3 demonstrates the construction of such a Brillouin zone in a hexagonal lattice. From the Brillouin zone, we can build band diagrams showing the occupation of TE and TM modes within the Brillouin zone which can then be applied across the photonic crystal.

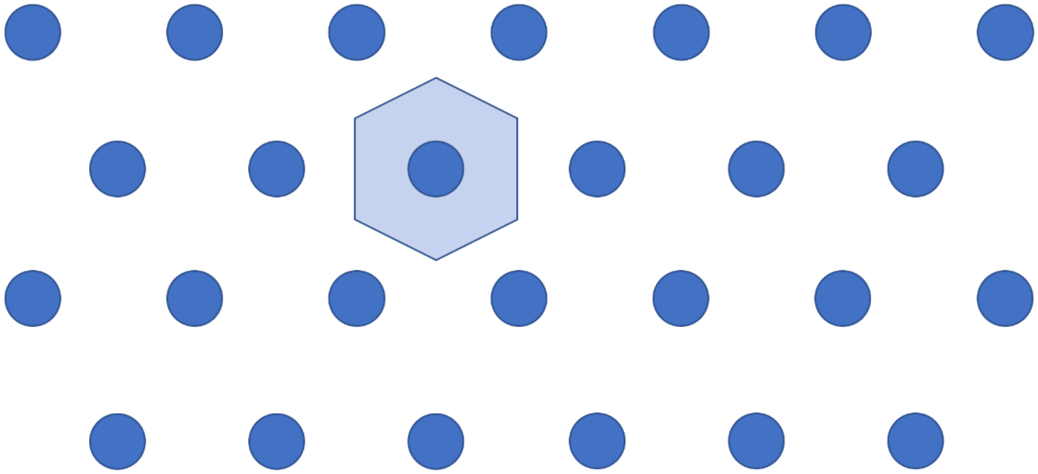

Figure 1.3: A demonstration of the Brillouin zone in a two dimensional hexagonal lattice. The shaded region is the Brillouin zone.

References

1. Butler, C.D. “Climate Change, Health and Existential Risks to Civilization: A Comprehensive Review,” *International Journal of Environmental Research and Public Health* **2018**, 15 (10).

2. Jackson, R. “The Effects of Climate Change: Vital Signs of the Planet,” *NASA* **2022** https://climate.nasa.gov/effects/

3. Caesar, L., Rahmstorf, S., Robinson, A., Feulner, G., Saba, V. “Observed Fingerprin of a Weakening Atlantic Ocean Overturning Circulation,” *Nature* **2018** 556 (7700) 191-196.

4. Cohen, J., Pfeiffer, K., Francis, J.A. “Warm Arctic Episodes Linked with Increased Frequency of Extreme Winter Weather in the United States,” *Nature Communications* **2018** 9 (1) 869.

5. Lenton, T.M., Rockstrom, J., Geffeny, O., Rahmstrorf, S., Richardson, K., Steffan, W., Schellnhuber, H. J. “Climate Tipping Points – Too Risky to be Against,” *Nature* **2019** 575, 592-595.

6. Butler, C. D., Keford, B. J. “Climate Change as a Contributor to Human Conflict,” *Nature* **2018** 555 (7698), 587.

7. Nicholls, R. J., Brown, S., Goodwin, P., Wahl, T., Lowe, H., Solan, M., Bodbold, J. A., Haigh, I. D., Lincke, D., Hinkel, J., Woll, C., Merkens, J. "Stabilization of Global Temperatures at 1.5°C and 2.0°C: Implications for Coastal Areas," *Philosophical Transactions of the Royal Society A* **2018** 376.

8. American Security Project "Climate Security is National Security," **2022** https://www.americansecurityproject.org/climate-security/

9. United States Department of Defense "Department of Defense Climate Risk Analysis," **2021.**

10. Climate Power, "Senator Sanders: Climate Change is the Existential Threat to Our Planet," **2020** https://climatepower.us/resources/climate-change-is-the-existential-threat-to-our-planet/

11. Duckworth, T. "Senator Tammy Duckworth on Climate Change and National Security," *U.S. Senator Tammy Duckworth of Illinois* **2019.**

12. Buis, A. "The Climate Connections of a Record Fire Year in the U.S." *NASA's Jet Propulsion Laboratory* **2021** https://climate.nasa.gov/ask-nasa-climate/3066/the-climate-connections-of-a-record-fire-year-in-the-us-west/

13. Zhuang, Y., Fu, R., Santer, B. D., Dickinson, R. E., Hall, A. "Quantifying Contributions of Natural Variability and Anthropogenetic Forcings on Increased Fire Weather Risk Over the Western United States," *Proceedings of the National Academy of Sciences* **2021** 118, (45).

14. Cohen, J., Agel, L., Barlow, M., Carfinkel, C., White, I., "Linking Arctic Variability and Change with Extreme Winter Weather in the United States," *Science* **2021** 373 (6559), 1116-1121.

15. NASA Goddard Institute for Space Studies "GISS Surface Temperature Analysis (GISTEMP v4)," *NASA* **2022** https://data.giss.nasa.gov/gistemp/

16. United States Environmental Protection Agency "Inventory of U.S. Greenhouse Gas Emissions and Sinks," *United States EPA* **2021.**

17. Friedlingstein, P., Andrew, R., Rogeli, J., *et al* "Persistent Growth of CO2 Emissions and Implications for Reaching Climate Targets," *Nature Geoscience* **2014,** 7, 709-1715.

18. Butler, J., Montzka, S., "The NOAA Annual Greenhouse Gas Index (AGGI) Earth System Research Laboratory," *Global Monitoring Division Website* **2019.**

19. Huntingfor,d C., Mercado, L.M. “High Chance that Current Atmospheric Greenhouse Concentrations Commit to Warmings Greater than 1.5°C Over Land,” *Scientific Reports* **2016** 6, 1-7.

20. Rogelj, J *et al* “Zero Emission Targets as Long-term Global Goals for Climate Change,” *Environmental Research Letters* **2015** 10 105007.

21. Figueres, C.; *et al*. “Emissions are Still Rising: Ramp up the Cuts,” *Nature* **2018**, 564, 27−30.

22. Davis, S. J. *et al* “Net-zero Emissions Energy Systems,” *Science* **2018** 360,6396.

23. National Renewable Energy Laboratories “Reference Air Mass 1.5 Spectra,” **2022.**

24. Center for Climate and Energy Solutions “Renewable Energy,” **2022.**

25. Green, M.A., Bremmer, S. P. “Energy Conversion Approaches and Materials for High-Efficiency Photovoltaics,” *Nature Materials* **2017** 16, 23-34.

26. Shockley, W., Queisser, O.J. “Detailed Balance Lmit of Efficiency of p-n Junction Solar Cells,” *Journal of Applied Physics* **1961** 32, 3, 510–519.

27. University of Michigan Center for Sustainable Systems “Photovoltaic Energy Factsheet,” *University of Michigan Center for Sustainable Systems* **2021.**

28. Department of Energy Office of Science “DOE Explains…Solar Fuels,” *Department of Energy Office of Science* **2022.**

29. Steinfeld, A. “Solar Thermochemical Production of Hydrogen-A Review,” *Energy* **2005** 78, 5, 603-615 .

30. Yadav, D., Banrejee, R. “A Review of Solar Thermochemical Processes,” *Renewable and Sustainable Energy Reviews* **2016**, 54, 497-532.

31. Rao, C. N. R and Dey, S. “Solar Thermochemical Splitting of Water to Generate Hydrogen,” *PNAS* **2017** 114 (51) 12285-13393.

32. Stangeland, K; *et al* CO_2 “Methanation: The Effect of Catalyst and Reaction Conditions,” *Energy Procedia* **2017** 105, 2022-2027.

33. Vogt, C., Monei, M., Kramer, G.J. *et al* “The Renaissance of the Sabatier Reaction and its Applications on Earth and in Space,” *Nature Catalysis* **2019** 2, 188-197.

34. Smith, C., Hill, A.K., Torennte-Murciano, L. "Current and Future Role of Haber-Bosch Ammonia in a Carbon-free Energy Landscape," *Energy Environmental Science* **2020** 13, 331-344.

35. Mac Dowell, N., Fennell, P., Shah, N. *et al* "The Role of CO_2 Capture and Utilization in Mitigating Climate Change," *Nature Climate Change* **2017** 7, 243-249.

36. Xu, Y., Li, J., Li, W. *et al* "Direct Conversion of CO and H_2O into Liquid Fuels Under Mild Conditions," *Nature Communications* **2019** 10, 1389.

37. Goetien, T. A., Zhang, X., Liu, J., Hupp, J.T., Farha, O.K. "Metal-organic Framework Supported Single Site Chromium (III) Catalyst for Ethylene Oligomerization at Low Pressure and Temperature," *ACS Sustainable Chemistry and Engineering* **2019**, 7 (2) 2553-2557.

38. Boretti, A., Castelletto, S., Al-Zubaidy, S. "Concentrating Solar Power technology: Present Status and Outlook," *Nonlinear Engineering* **2019** 8, 10-31.

39. Phillipps, S., Bett, A.W., Horowitz, K., Kurtz, S., "Current Status of Concentrator Photovoltaic (CPV) Technology," *ISE and NREL* **2015.**

40. Novotny, L.; Hecht, B. "Principles of Nano-Optics," Cambridge, U.K., **2006**.

41. Joannopoulos, J. D.; Johnson, S. G.; Winn, J. N.; Meade, R. D." Photonic Crystals: Molding the Flow of Light," 2nd ed.; Princeton University Press: Princeton, **2008.**

Chapter 2

THE TANDEM LUMINESCENT SOLAR CONCENTRATOR

2.1 Luminescent Solar Concentrators

The efficiency of photovoltaics can be improved by converting incident spectral light to monochromic light at the band edge of a photovoltaic material allowing the photovoltaic to operate in solely its optimal wavelength range[1,2]. One method to do such is via luminescent solar concentrators. Luminescent solar concentrators (LSCs) were first presented in the late 1970s and are defined as a layer of material with some variation of luminophores that absorb incident light and re-emit the light at a red-shifted wavelength with high quantum efficiency[3]. The emission is then guided to a small-area photovoltaic via total internal reflection of the medium through which the luminophores are dispersed. In most cases, the photovoltaic material lines the edges of the waveguiding layer of the LSC[3]. LSCs are unique in their ability to capture diffuse sunlight due to the isotropy of the luminophore absorption, making them a promising technology for Nordic or sub-tropical areas with less direct incident sunlight[3]. Originally, LSCs were fabricated using fluorescent dyes as the red-shifting luminophores[3-5]. While dyes have high quantum efficiencies, their limited Stokes ratio and absorption limits the maximum possible LSC efficiency[3, 6-8]. However, recent developments in cadmium selenide core, cadmium sulfide shell (CdSe/CdS) quantum dots (QDs) demonstrating near unity photoluminescence quantum yields (PLQYs) and high Stokes shifts has allowed the potential for more efficient LSCs[9]. The Stokes shift is defined as the difference between the luminophore's absorption wavelength and the luminophore's emission wavelength. Having a high Stokes ration is important because overlap of the absorption and emission wavelengths increases the chance of parasitic re-absorption of luminophore emissions[9,10]. CdSe/CdS QDs also demonstrate high Stokes ratios, a more internal QD property defined as the ratio of the absorption at the CdS band edge to the CdSe band edge[9]. A high Stokes ratio similarly results in a more efficient QD luminophore as absorbed light is more efficiently converted with minimal parasitic effects caused by the respective bands of the two distinct QD semiconducting materials[10]. CdSe/CdS QDs absorb light up to 500 nm and re-emit at 635 nm, though the emission wavelength can be slightly tuned by changing the size of the QDs. They are highlight efficient, with a PLQY of 99.6% ± 0.3# with a Stokes shift of 52 eV, and a Stokes ratio of over 100. CdSe/CdS QDs therefore have the potential to drastically improve the performance of LSCs[9,10].

While many original LSC designs relied on TIR to trap luminophore emission, escape cone losses were a major source of loss in LSCs[3,11]. For example, if a polymer has an index of refraction of n=1.44, only 73% of luminophore emission remains within the waveguiding material. The rest is lost and unable to be converted by the photovoltaic. Equation 2.1 shows a simplified calculation for escape cone loss which assumes isotropic emitters, where n_0 is the index of the surrounding medium and n_1 is the index of refraction of the waveguide medium. Equation 2.1 does not consider Fresnel reflections or emission diffusion rate and is not valid for directionally oriented luminophores such as quantum rods. For a more thorough derivation of escape cone loss, see Reference 12 by McDowall *et al* (2013).

$$P(esc) = 1 - \sqrt{1 - \left(\frac{n_0}{n_1}\right)^2} \tag{2.1}$$

One such method to overcome escape cone loss is the integration of wavelength selective filters[11,13-16]. One-dimensional photonic crystal Bragg filters consist of 10s to 100s of layers of alternating materials with different indices of refraction. Based on the index of refraction of each respective material of the Bragg filter and the number of repetitions of the periodic array, one can design a spectrally selective wide-band filter[15,16]. Bragg filters can be designed to have reflection bands with near unity reflectivity[10,15,16]. While Bragg filters add cost and weight to the module, they are ultimately worth the increases by increasing the trapping efficiency of a LSC[10]. Figure 2.1 shows a schematic of light trapping in LSCs with and without such a Bragg filter, overlayed with the absorption and emission profile of a CdSe/CdS QD.

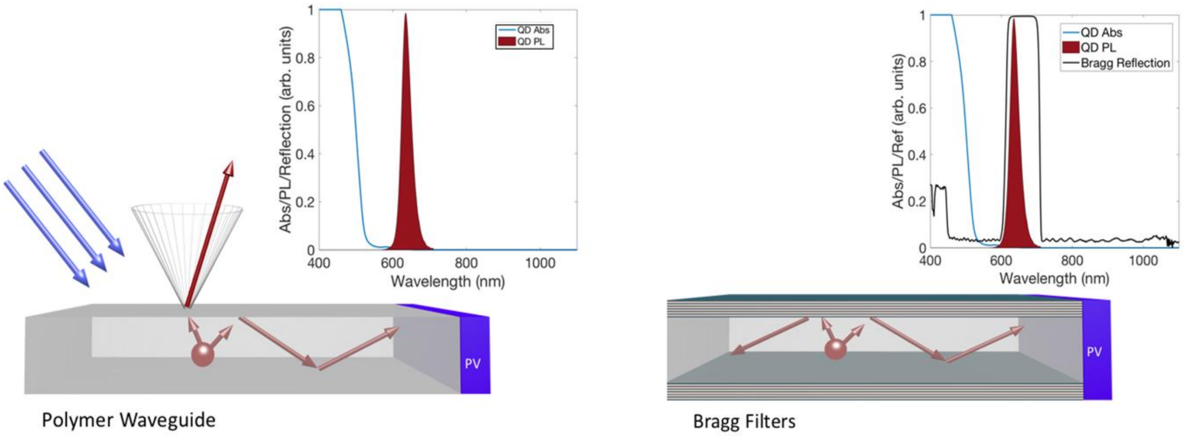

Figure 2.1: Left panel, a LSC using a polymer waveguide as the sole trapping mechanism for CdSe/CdS QD emission. Right panel, a demonstration of Bragg filters as spectrally selective filters along with their optical properties plotted alongside the QD emission.

Since a LSC is predominantly an optical module, performance of a LSC is not typically evaluated based on overall photovoltaic performance[3,17-19]. Concentration factor is a metric that considers optical efficiency and is therefore considered more appropriate for analyzing the efficacy of a LSC. The concentration factor of a LSC can have many definitions, including ones that consider the thermalization of the emission within the LSC. It is helpful to first understand the concentration factor qualitatively. Most simply, the concentration factor is defined as an effective enlargement of the PV material caused by the increase in light guided to PV material by coupling to a LSC. Equation 2.2 gives a simple definition of the concentration factor as a function of optical efficiency, where the optical efficiency is defined as ratio of the flux guided to PV material when coupled to a LSC to the flux guided to PV material without being coupled to a LSC, and the geometric gain (G) is defined as the ratio of LSC area to the area of active PV material. The increase in QD PLQY, Stokes shift, and Stokes ratio, along with improved Bragg filter metrics allow to higher potential concentration factors than previously possible with luminophores such as fluorescent dyes[1,3,10,18-19].Concentration factor is the LSC community standard metric, and therefore will be referenced throughout this work. However, it is important to note the limitations of concentration factor. Since concentration factor is simply a function of optical efficiency and geometric gain, it is possible to achieve very high concentration factors with modules that have a very low power conversion efficiency[18]. Similarly, concentration factors can be manipulated by using very high geometric gains. High geometric gains can result in lower power conversion efficiencies because more optical loss mechanisms are introduced as a smaller area of the overall LSC module is populated by active PV material[10]. While these limitation are important in the overall analysis of LSCs as technology disruptive to the PV market, concentration factor remains a simple and effective metric to quantize LSC performance, independent of the PV material which can have significant effects on the achievable power conversion efficiency of the module.

$$Concentration\ Factor = G\eta_{opt} \tag{2.2}$$

While the recent improvements in CdSe/CdS QDs and Bragg filters provides a path for increased efficiencies and concentration factors in LSCs, they are still ultimately limited by the attainable geometric gain in an edge-lined photovoltaic architecture. In an edge-lined LSC, the overall module efficiency is directly proportional to the size of the LSC. As the area of the LSC increases, the luminophore emission has to travel a longer distance in order to reach the photovoltaic material. The longer distance leads to an increased chance of the emission being parasitically absorbed by the waveguide or the QD, escaping the LSC module, or decaying within the LSC module before reaching photovoltaic material[3,10,18]. This architecture limits the use of LSCs to small scale modules where the emission will be more effectively converted. The current record for power conversion efficiency in a LSC is 7.1%[11]. While LSCs can be produced at a fairly low cost, the current efficiencies are not competitive in efficiency or cost to Si-PV modules, which are inexpensive and have efficiencies of around 18-21%[20,21]. Therefore current LSCs are often used as smart windows due to trancparency of QDs in the NIR or due specifically to the color of the QD allowing for a stained-glass appearance. However, these modules suffer from very low efficiencies as the LSC area is so large that typically over 97% of the emission is lost[22]. This limits the utility of LSCs to niche markets rather than large scale energy production applications, as the power conversion efficiencies are simply not high enough to be economically competitive[20,22].

2.2 The Tandem Luminescent Solar Concentrator

Tandem solar modules consist of multiple photovoltaic materials tuned to operate at different band gaps. These different PV materials can more effectively convert a larger portion of the incident solar spectrum. Tandem photovoltaics have been a focus of high-efficiency PV research due to their high achievable efficiencies through power accumulation of multiple junctions with different PV materials[20]. While these modules are able to attain high efficiencies, they are ultimately limited in application due to the high cost of the numerous layers of PV materials, some of which are made of more expensive materials such as GaAs and other III-V semiconductors[20]. Since LSCs are not opaque and can be fabricated with low cost materials, tandem LSCs have been explored as a method to create more efficient PV modules[10,23,24]. While overall power conversion efficiencies increase in such tandem LSC modules, they are still limited by the high geometric gains caused by the use of edge-lined photovoltaic material[23,24].

In collaboration with NREL, UC Berkeley, and UIUC, we have presented a new tandem LSC architecture, in which the PV material is an array of InGaP microcells placed co-planar to the LSC rather than edge-lined. The InGaP microcells have an efficiency of 19.3% under AM 1.5g conditions. The co-planar microcell orientation allows the LSC component to maintain efficiencies across a range of areas due to the geometric gain staying consistent at any size. The InGaP microcell array with a geometric gain of 100, is optically coupled to a waveguide of poly(lauryl) methacrylate (PLMA) with the previously described highly efficient CdSe/CdS QDs dispersed within the PLMA. The emission of the CdSe/CdS QDs at 635nm is tuned to the band edge of the InGaP microcells. The LSC layer is then encased with spectrally selective Bragg filters with a band tuned to reflect the QD emission. The LSC layer is coupled to a Si sub-cell. All incident light below 700nm interacts with the LSC layer. Light longer than 700nm travels to the Si sub-cell (η=19%) to be converted. Figure 2.2 shows a schematic of the tandem LSC along with the spectral properties of each LSC material. Through Monte Carlo ray tracing analysis performed by David R. Needell, we have determined that the maximum theoretical efficiency for such a tandem module is 28.2%[10].

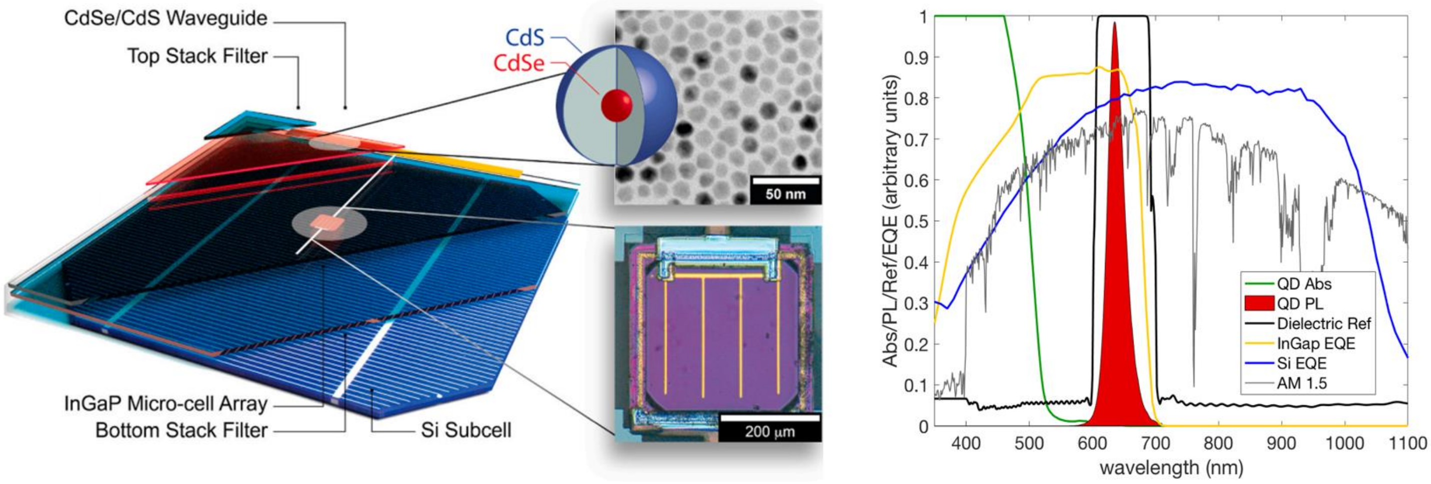

Figure 2.2: The left shows a schematic of the tandem LSC. Image from Phelan et al (2021)[25]. The right shows the spectral properties of each component of the tandem LSC overlayed with the AM 1.5g spectrum. This demonstrates how each component of the LSC fully utilizes the full range of the AM 1.5g spectrum.

2.3 Prototype Fabrication

The initial goal set by ARPA-E for the protype was the fabrication of a 100 cm^2 tandem LSC module, to be tested at the NREL's field testing site in Golden, CO. As previously discussed, due to the isotropic nature of the QD absorption, theoretically a LSC should maintain efficiency in diffuse and direct sunlight[3,25]. Therefore, testing at the NREL facility in CO is an ideal way to test this theory given the cloudy and snowy conditions in November 2018. While many of the components were fabricable at this scale, there were many obstacles found in the effort to assemble the full 100 cm^2 LSC module.

In this prototype, the top and bottom Bragg reflectors were provided at scale by Evaporated Coatings Inc. (ECI). While the ECI mirrors have strong reflection at the QD emission spectrum, they suffer from the blue-shifting mechanism inherent in such Bragg filters at increasing angles of incidence[10,16]. Furthermore, the reflection shown in the short wavelength range adds some loss mechanisms as the Bragg filters reflect light that could otherwise be absorbed by the QDs. The spectral properties of the Bragg filter is shown in Figure 2.3.

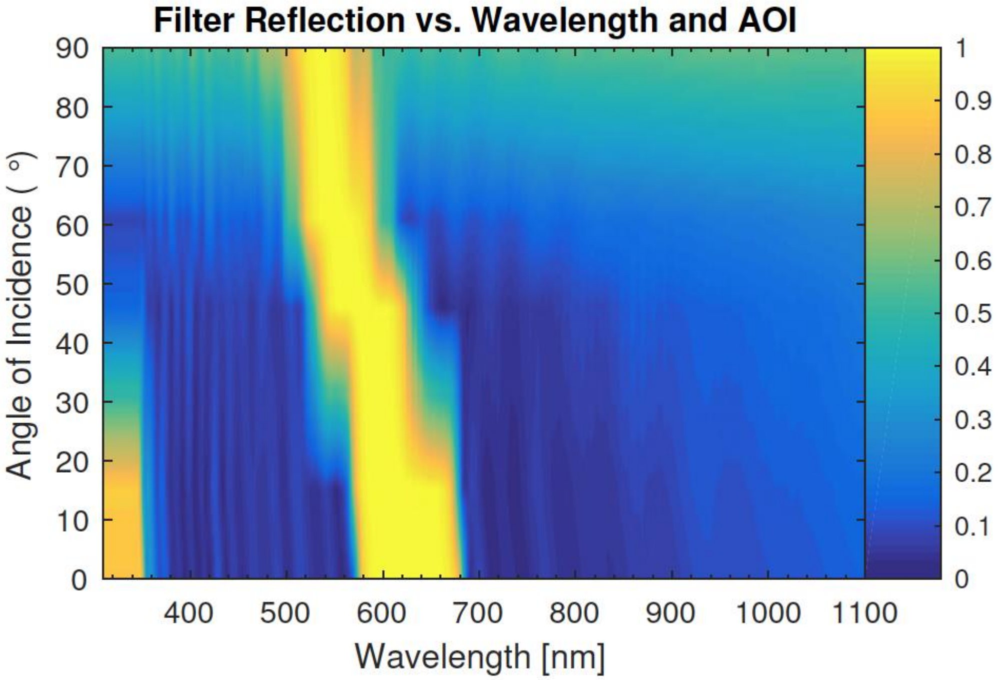

Figure 2.3: ECI fabricated Bragg filter reflection profile at increasing angles of incidence, showing the blue-shifting mechanism of Bragg filters.

The waveguide was fabricated by UIUC, but Caltech has also since acquired the capabilities to integrate the QDs with PLMA in house. However, one limitation is the light and air sensitivity of the QDs even when suspended in PLMA. The waveguide was frequently damaged if not kept in an Argon purged container. The QDs also suffer a performance hit when suspended in PLMA. The PLQY drops from ~99.6% to ~95%. While this is still a high PLQY, the decrease does ultimately make a difference in module performance[1,9,10].

The individual InGaP cells are fabricated and diced by our collaborators at NREL and perform as initially modelled. However, connecting the InGaP micro-cell array was the greatest limitation in fabricating and assembling a full 100 cm^2 module. Even before fabrication, there is difficulty considering the goal geometric gain of such an array. The optimized geometric gain for the tandem LSC is 100, which translates to 1% of the module area being covered by InGaP micro-cells. The micro-cells have an area of 400 $microns^2$. This would require 625 microcells to be placed in an array to reach a geometric gain of 100. To place 625 micro-cells, it would require some manufacturing tool such as a pick-and-place machine capable of high volume. Our collaborators at UIUC anchor each InGaP cell onto the glass substrate by hand. The leads connecting the cells are then sputtered. We instead opted for a 5x5 array of the InGaP cells. This is a substantially larger geometric gain that what is optimized and therefore the LSC module will not be particularly efficient. However, it is the maximum amount that was feasible at this stage of the project, since the cells are placed by hand.

At Caltech, we received the InGaP array to then optically couple to the QD waveguide. Ideally, the QD waveguide is deposited directly onto the InGaP array to ensure full optical coupling. However, given the current stage of the project, it was deemed too risky to do so as we wanted to protect the InGaP cells and the array, potentially making it testable for multiple assembly iterations. While UIUC fabricated the standalone array, the Caltech team was responsible for the electrical connection of the array. Based on the Monte Carlo ray trace analysis, the ideal thickness for the waveguide is 30 microns. We therefore wanted to minimize the thickness of any encapsulant for the microcell array, since the QD waveguide was already 30 microns. However, in order to electrically connect the InGaP array to the necessary electrical leads, we have to employ some sort of connector that is unfortunately thicker than 30 microns. We first tried using 80 micron thick copper tape which we then doctor bladed 20 microns of PDMS over. We use PDMS because it is an optically clear and durable polymer. However, the copper tape was not conductive enough for such a set up. We then used high conductive silver epoxy to attach leads. Unfortunately, the application of epoxy durable enough to ensure security of the leads resulted in an even thicker encapsulation layer on the order of 100 microns. We had to make the layer thick enough to create a smooth even surface so that the QD waveguide layer can couple to the InGaP array encapsulation with minimal airgaps to best approximate optical coupling.

The Silicon sub-cell was delivered by NREL. We had similar encapsulation issues with the Si cell as we had to attach the leads to the bus bars in a method that ultimately increased the encapsulation thickness. With increased encapsulation thickness comes increases in loss mechanisms for light as more can be parasitically absorbed by the polymer. In both the InGaP and Si encapsulation, we experience particles that caused defects. Full fabrication in at least a class 100 clean room is recommended for future iterations.

This first attempt at full device fabrication ultimately was unsuccessful. The mechanical strains and the interconnects in the InGaP array itself were unreliable and experienced shorting and disconnects. We were unable to test this full device in the indoor four point probe current-voltage sweep or in the outdoor testing configuration. However, through this effort we learned of many fault points that could be optimized for future module assembly.

2.4 Outdoor Testing of a Tandem Luminescent Solar Concentrator Module

In the second generation of the tandem LSC module assembly, we built upon the lessons we learned from the prior unsuccessful assembly attempt. The first change we made was the array size. For the first version of the module discussed in the prior section, even if the module did not short, the dimensions would result in a geometric gain so high that an analysis of the LSC component would not be particularly compelling. The dimensions of the new LSC are 2.5 cm^2 with a 4x4 InGaP array. This results in a geometric gain of 625, as opposed to the previous module where the geometric gain was 2,500. For a more detailed discussion of the methods by which each individual component was fabricated, refer to Phelan et al, Reference 25 of this chapter. The Bragg filters were again provided by ECI, but at a smaller size to match the module dimensions. In this trial, the QD waveguide was deposited directly onto the InGaP array to ensure optical coupling. In order to allow the Caltech team a method to attach the leads, the QD waveguide was only deposited over the InGaP array, leaving the bus bars clear for lead coupling without having to worry about thickness of epoxy or other connection methods. The Si cell was fabricated to match the dimensions of the module and demonstrated an efficiency of 20.6% under 1 sun illumination in solar simulator tests, and 14.4% when the waveguide and Bragg filters are placed on top of the cub-cell. The Si cell was still encapsulated in thick PDMS which adds some loss mechanisms to the module. The leads were attached to larger clips that were more mechanically durable, allowing us to connect and un-connect the electrical connections without moving the more delicate leads attached directly to the Si or InGaP bus bars. The module is attached to a more rigid box that can be placed on a testing platform. An image of the LSC module as a standalone and coupled within the system mounted on the testing platform is shown in Figure 2.4. As stated in the previous section, we performed this testing at the NREL field testing site in Golden, CO. The tests were performed in November 2018.

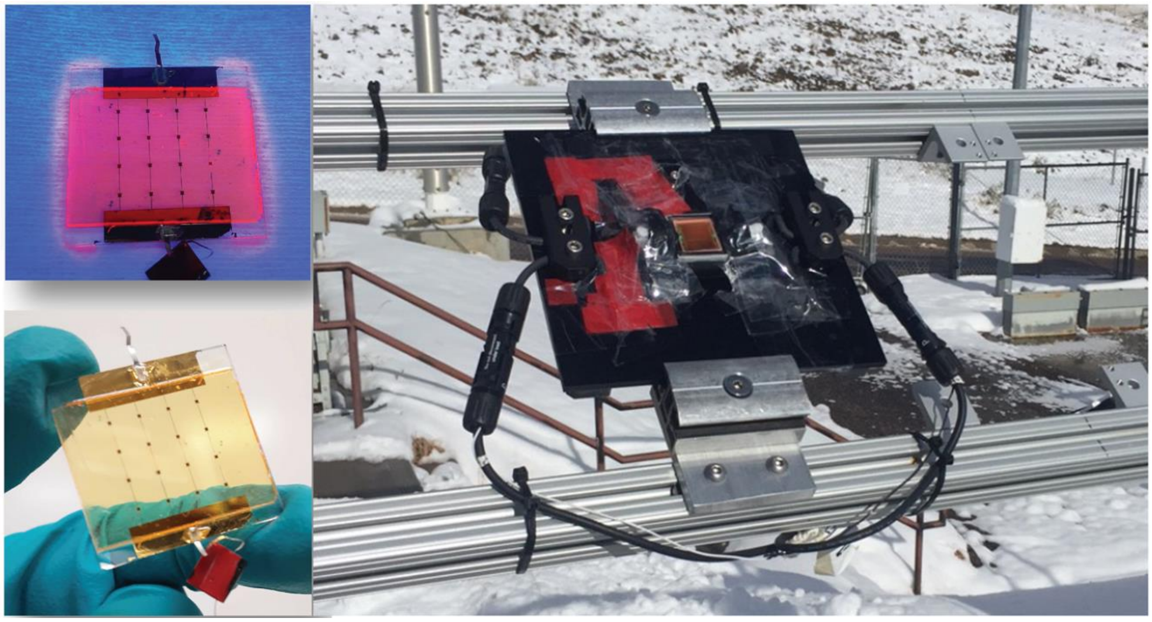

Figure 2.4: The top left shows the LSC InGaP array with the optically coupled QD waveguide under blue light illumination. Bottom left shows the LSC component in ambient indoor lighting. The right image shows the LSC component coupled to the Si sub-cell mounted on the testing site.

In outdoor field testing, the tandem LSC was tilted at a fixed 40° axis. Given the location and time zone, the testing concluded every day around 4:00 pm due to the large off-normal angle of incidence from the sunset resulting in negligible power output from the LSC. The resulting measured power conversion efficiency of the LSC component was 0.04%. While the efficiency is low in outdoor testing, we can attribute many of these loss mechanisms to individual component faults. One factor contributing to this low average power conversion efficiency is the degradation over time of the LSC component. This degradation is likely caused by air exposure of the QDs. Fortunately, this can be remedied by a waveguide resin fabricated by Nanosys that has shown to prevent QD degradation. This can easily be applied to future modules. The Bragg filters are a substantial source of loss. The Bragg filters reflect a band of 600-700nm which helps some QD emission travel to the InGaP cells, but it also blocks a substantial portion of that light from entering the LSC or Si sub-cell component for conversion. Furthermore, the blue-shifting of the Bragg filter reflection bands contributes to loss as the transmission window in the short wavelength range decreases allowing less incident light to be absorbed by the QDs. Lastly, the geometric gain of such a module is sufficiently large that lower efficiencies are expected even without these loss mechanisms. Manufacturing a scalable printing method of such a micro-cell array is of great importance in the fabrication of an efficient LSC module. Figure 2.5 shows how improvement of each loss mechanism can improve the overall efficiency of each tandem LSC component and the module as a whole.

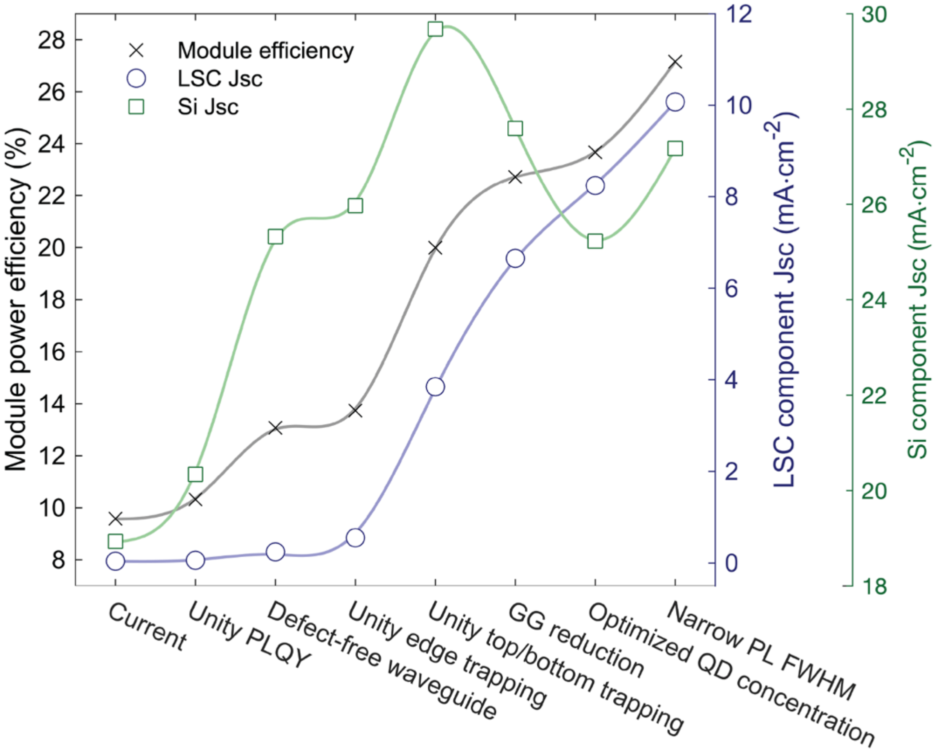

Figure 2.5: Image from Phelan et al (2021). A study of performance as a function of component efficiency[25].

2.5 Discussion

In this section, we have presented a novel architecture for a tandem LSC that can be added to current PV farms to increase overall module efficiency beyond 25% using low cost materials. With so many components, each imperfection compounds to create defects in the overall module. This means that every component must be as close to a perfect material as possible, and there is little room for error since compounding errors could lead to minimal boosts in efficiency when coupled to a Si sub-cell; or worse, the LSC component can actually decrease the performance of a Si sub-cell. We fabricated a full tandem LSC module and performed outdoor testing to show the viability of such a module. Each component of the LSC contributes loss mechanisms when they do not perform to near-unity standards. The blue-shifting of the Bragg filters is a significant source of loss in the LSC. Of the many improvements to be made on the module, I have focused on improving the spectrally-selective filters.

References

1. Needell, D.R., Bukowsky, C.R., Darbe, S., Bauser, H., Ilic, O., Atwater, H.A. "Spectrally Matched Quantum Dot Photoluminescence in GaAs-Si Tandem Luminescent Solar Concentrators," *IEEE Journal of Photovoltaics"* **2019** 9, 2, 397-401.

2. Bett, A.W., Dimroght, R., Lockenhoff, R., Olivia, E., Schubert, J. "III-V Solar Cells Under Monochromatic Illumination," *2008 33rd IEEE Photovoltacis Specialists Conference* **2008** 1-5.

3. M. G. Debije and P. P. C. Verbunt, "Thirty Years of Luminescent Solar Concentrator Research: Solar Energy for the Built Environment," *Advanced Energy Materials,* **2012** 2, 1, 12–35.

4. Wittwer, V., Stahl, W., Goetzberger, A. "Fluorescent Planar Concentrators," *Solar Energy Materials*, **1984** 11, 3, 187–197.

5. Yablonovitch, E. "Thermodynamics of the Fluorescent Planar Concentrator," *Journal of the Optical Society of America*, **1980,** 70, 11, 1362–1363.

6. F. Vollmer and W. Rettig, "Fluorescence Loss Mechanism Due to Large-Amplitude Motions in Derivatives of 2,2′-bipyridyl Exhibiting Excited-State Intramolecular

Proton Transfer and Perspectives of Luminescence Solar Concentrators," *Journal of Photochemistry and Photobiology A Chemistry.*, **1996**, 95, 2, 143–155.

7. J. S. Batchelder, a H. Zewail, and T. Cole, "Luminescent Solar Concentrators . 1 : Theory of Operation and Techniques for Performance Evaluation," *Applied Optics*, **1979,** 18, 18, 090–110.

8. B. A. Swartz, T. Cole, and A. H. Zewail, "Photon Trapping and Energy Transfer in Multiple-Dye Plastic Matrices: An Efficient Solar-Energy Concentrator," *Optics Letters*, **1977,** 1, 2, 73–75.

9. Hanifi, D. A.; Bronstein, N. D.; Koscher, B. A.; Nett, Z.; Swabeck, J. K.; Takano, K.; Schwartzberg, A. M.; Maserati, L.; Vandewal, K.; van de Burgt, Y.; Salleo, A.; Alivisatos, A. P. "Redefining Near-Unity Luminescence in Quantum Dots with Photothermal Threshold Quantum Yield," *Science* **2019**, *363*, 1199−1202.

10. Needell D.R. *et al* "Design Criteria for Micro-Optical Tandem Luminescent Solar Concentrators," *IEEE Journal of Photovoltaics*, **2018** *8* 1560-1567.

11. Slooff, L.H., Bende, E.E., Burgers, A.R., Budel, T., Pravettoni, M., Kenny, R.P., Dunlop, E.D. and Büchtemann, A. "A Luminescent Solar Concentrator with 7.1% Power Conversion Efficiency," phys. stat. sol. *RRL*, **2008** *2*: 257-259.

12. McDowall, S.; Butler, T.; Bain, E.; Scharnhorst, K. and Patrick, D. "Comprehensive Analysis of Escape-Cone Losses from Luminescent Waveguides," *Applied Optics.* **2013** *52*, 1230-1239.

13. Debije, M. G.; Van, M.-P.; Verbunt, P. P. C.; Kastelijn, M. J.; van der Blom, R. H. L.; Broer, D. J. and Bastiaansen, C. W. M. "Effect on the Output of a Luminescent Solar Concentrator on Spplication of Organic Wavelength-Selective Mirrors," *Applied Optics,* **2010** vol. *49, no. 4*, 745–51.

14. Verbunt, P. P. C. ; Tsoi, S.; Debije, M.G.; Boer, D. J., Bastiaansen, C.W.M.; Lin, C. de Boer, D.K.G. "Increased Efficiency of Luminescent Solar Concentrators After Application of Organic Wavelength Selective Mirrors," *Opt. Express* **2012** *20,* 655-668.

15. Leem, J. W., Guan, X.-Y. & Yu, J. S. "Tunable Distributed Bragg Reflectors with Wide-Angle and Broadband High-Reflectivity using Nanoporous/dense Titanium Dioxide Film stacks for Visible Wavelength Applications," *Opt. Express* **2014** *22,* 18519–18526.

16. Baumeister, P. "Optical Coating Technology". SPIE Press, Bellingham, Washington USA: 2004.

17. Yablanovich. E. “Thermodynamics of the Fluorescent Planar Concentrator,” *Journal of the Optical Society of America*, **1980** Vol. *70*, No. *11* 1362-1363.

18. Bronstein, N. D.; Yao, Y.; Xu, L.; O’Brien, E.; Powers, A. S.; Ferry, V. E.; Alivisatos, A. P.; and Nuzzo, R. G. “Quantum Dot Luminescent Concentrator Cavity Exhibiting 30-fold Concentration,” *ACS Photonics*, **2015**, *2, 11,* 1576-1583.

19. Klimov, V.I.; Baker, T. A.; Lim, J.; Velizhanin, K.A. and McDaniel, H. “Quality Factor of Luminescent Solar Concentrators and Practical Concentration Limits Attainable with Semiconductor Quantum Dots,” *ACS Photonics* **2016** *3* (6), 1138-1148.

20. Horowitz, K. A. W.; Remo, T.; Smith, B.; and Ptak, A. “Techno-Economic Analysis and Cost Reduction Roadmap for III-V Solar Cells,” Golden, CO: National Renewable Energy Laboratory. **2018** NREL/TP-6A20-72103.

21. University of Michigan Center for Sustainable Systems “Photovoltaic Energy Factsheet,” *University of Michigan Center for Sustainable Systems* **2021.**

22. Meinardi, F., Bruni, F. & Brovelli, S. “Luminescent Solar Concentrators for Building-Integrated Photovoltaics,” *Nature Review Mater* **2017** *2***,** 17072.

23. Wu, K., Li, h., Klimov, V. “Tandem Luminescent Solar Concentrators Based on Engineered Quantum Dots.” *Nature Photonics* **2018** 12, 105-110.

24. Baldo, M. “Luminescent Solar Concentrators,” *Optics and Photonics for Advanced Energy Technology* **2009.**

25. Phelan, M., Needell, D.R., Bauser, H., Su, H., Deceglie, M., Theingi, S., Koscher, B., Nett, Z., Bukowsky, C., Ilic, O., Stradins, P., Geisz, J., Nuzzo, R., Alivisatos, A.P., Atwater, H.A. “Outdoor Performance of a Tandem InGaP/Si Photovoltaic Luminescent Solar Concentrator,” *Solar Energy Materials and Solar Cells* **2021**, 223, 110945.

Chapter 3

SPECTRALLY SELECTIVE HIGH CONTRAST GRATING REFLECTORS FOR LUMINESCENT SOLAR CONCENTRATORS

3.1 Introduction to High Contrast Gratings in the Visible Spectrum

The ability to manipulate light in the visible spectrum via high index, lossless photonic systems is of great importance for many applications across the field of nanotechnology. nanotechnology including photonic sensors, beam steering components for lidar, photonic integrated circuits, on-chip resonators, and meta-lenses[1-7]. One design to induce such optical phenomenon is a high-contrast grating. High-contrast gratings (HCGs) consist of a single layer of high index material patterned at a near or sub-wavelength scale on a low index substrate. HCGs have frequently been studied as an alternative to costly and angularly sensitive Bragg stack filters, making them a particularly promising direction for applications in the tandem LSC[8-12]. HCGs also have applications in vertical-cavity surface-emitting lasers, high quality factor resonators, and high aperture focusing reflectors[8]. More recently, the field of HCGs has been shaped by the exploration of resonant dielectric metasurfaces for visible frequency meta-lenses[13–18]. Instead of the high index contrast producing a reflection peak, the high contrast enables the induction of a phase gradient tunable from 0 to 2π, allowing for broadband applications and cross-wavelength tunability[4,16-18]. Lossless HCG materials for metalenses have wide ranging applications including diagnostic imaging, unmanned automobiles, high resolution imaging optical sensors, holograms, and optical communication[17]. An understanding of the spectrally selective high reflectivity of HCGs can in part be derived from analytical Mie theory, in which the pillars act as Mie resonators creating interference in the transverse electric and magnetic modes of the incident light[19-21]. The incident light therefore couples to guided modes within the resonating array[22]. Given this mechanism, HCG reflectance patterns differ from Bragg filters (which rely upon constructive and destructive wave interference through many layers of alternating low/high index materials) by exhibiting a resonant peak, where modes are guided into the HCG substrates or any coverings for the HCG array[8,22]. By adjusting the physical parameters of the HCG array geometry (pitch, feature size, thickness), we can alter the guided modes' resonant wavelength, thereby tuning the peak reflectivity[8,19,22]. The overall thickness and spectral tunability of HCGs could enable such structures to technologically disrupt various photonic applications (e.g., metalenses, broadband spectral reflectors[7,19,]).

3.2 Materials and design requirements

In order to generate the index contrast between the grating material and the substrate necessary to induce a strong resonance, we need to choose a grating material with an index of refraction above 3. Indices of refraction less than 3 are able of producing reflection peaks, but not one efficient enough to achieve the near-unity required for adaptation in an LSC. Furthermore, the ideal high-contrast grating material as a near-zero absorption coefficient so that the photonic components themselves do not parasitically absorb the light resulting in decreased overall module performance. These requirements make wide bandgap semiconductors the most promising option for such applications. Many materials currently used in such high contrast systems have limitations to their performance such as high absorption in the visible spectrum (Si, a-Si, GaP), or lower indices of refraction than what is typically required for strong resonance (TiO_2)[23,24]. Crystalline Si and a-Si both have high indices of refraction (n >3), but also exhibit loss in the visible wavelength range, limiting their optimal performance to the NIR[19,24]. TiO_2 is rather lossless in the visible wavelength range, but has a maximum index of refraction of 2.5, necessitating high aspect ratio resonant structures to enable the phase gradients requires by visible wavelength metasurfaces and other nanophotonic applications[23,25,26.] GaP exhibits both a high index of refraction (n>3) and near zero absorption coefficient for much of the visible and NIR, but with the limited suitable substrate materials and technically involved substrate transfer process, there exists a compelling need for high refractive index, low absorption materials that can be fabricated with common and durable processes[24]. One limitation of all such wide-bandgap materials is a high absorption coefficient in the QD absorption range. This is intrinsic to wide-bandgap semiconductors and therefore limits the applications of such a spectrally selective HCG reflector as the bottom mirror in the LSC. If the HCG were employed as a top mirror, it would ultimately parasitically absorb the incident light that must be converted by the QD. I explored two different materials with properties theoretically ideal for a HCG spectrally selective reflector in the visible spectrum: AlSb and a-SiC:H. The substrate for each HCG is fused silica as it is the most transparent form of glass. As stated in the introduction, HCGs are of particular interest due to their potential insensitivity to varying angles of incidence. However, this property is not intrinsic to all HCG designs. For example, HCGs consisting of a periodic grating of bars is particularly sensitive to angle of incidence[8]. Work by Darbe et al demonstrated that by designing a HCG made up of a hexagonal array of pillars with a pitch inducing in a relatively high fill fraction of grating-to-substrate exposure, we can produce a highly efficient reflection peak that is robust at a wide range of angles of incidence[27]. We therefore opt for a hexagonal array of pillars in all the following spectrally selective HCG reflector designs.

3.3 AlSb High Contrast Grating Reflectors

Given that the goal of this work is to design a spectrally-elective high-contrast grating reflector to re-reflect CdSe/CdS QD emission at 635nm, we must consider the optical components' performance at 635 nm. One such wide bandgap material that appears to satisfy these conditions is AlSb. Figure 3.1 shows the n,k data for thin film AlSb, as measured by Zollner et al[28].

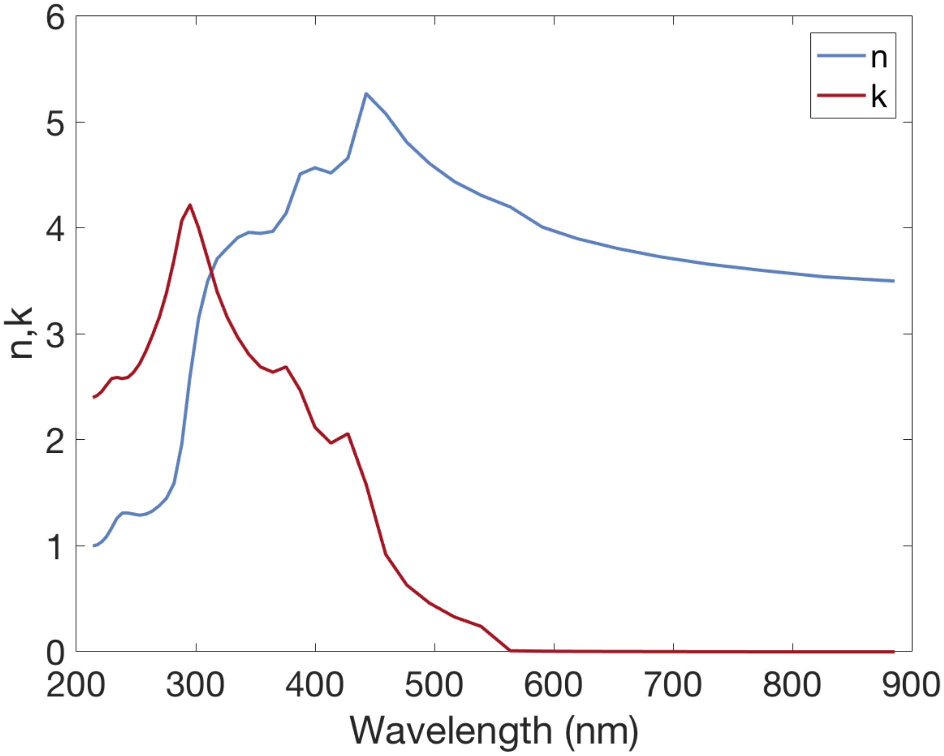

Figure 3.1: The index of refraction and absorption coefficient of AlSb. The index of refraction is 3.8 and the absorption coefficient is 0.004 at 635nm.

The n,k profile of AlSb makes it a promising candidate for other high-contrast nanophotonic applications in the visible wavelength range due to its low absorption coefficient beyond 600nm. As stated in section 3.1, the optical behavior of a spectrally-selective grating is determined by the geometric parameters of the HCG design. In the case of a hexagonal array of nanopillars, the tuned geometric components are the pitch, radius, and height of the pillars. In order to analyze the reflection peak with different geometric parameters, we use Lumerical FDTD method electromagnetic simulations. Given that we consider the performance of the HCG under incident sunlight, we perform broadband FDTD simulations across a wavelength range of 300-1100nm, matching the AM 1.5 spectrum. over the maximum number of iterations for the entire duration of the FDTD resolution. If these modes are not resolved, the FDTD results can be greatly affected and ultimately inaccurate. Figure 3.2 demonstrates such tunability of a hexagonal array of AlSb throughout the visible spectrum. The limitation for such a mirror eventually becomes the increasing absorption coefficient.

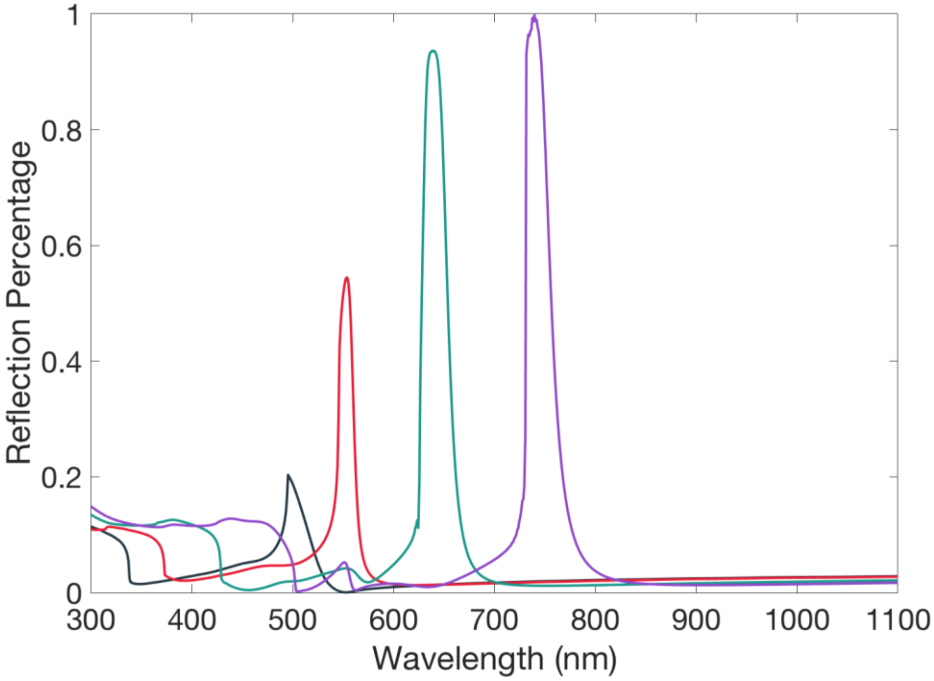

Figure 3.2: A demonstration of the variation in the resonance wavelength of a AlSb HCG as a function of varying geometric parameters.

Using Lumerical with a MATLAB script sweeping program, we performed FDTD simulations iteratively, sweeping across the pitch, radius, and thickness in order to find the optimal parameters to produce a reflection peak at 635 nm with a full-width-half-mx matching that of the CdSe/CdS luminescence. The MATLAB code allows for a single parameter to be swept in a given trial and therefore this simulation process underwent many iterations to narrow down the ideal parameters. Figure 3.3 shows the optimized reflection peak of an AlSb metasurface designed around the QD luminescence peak. The resulting peak has a maximum reflection of 93.5% at 635 nm. The necessary geometric parameters are a pitch of 494nm, a radius of 100nm, and a height of 95nm.

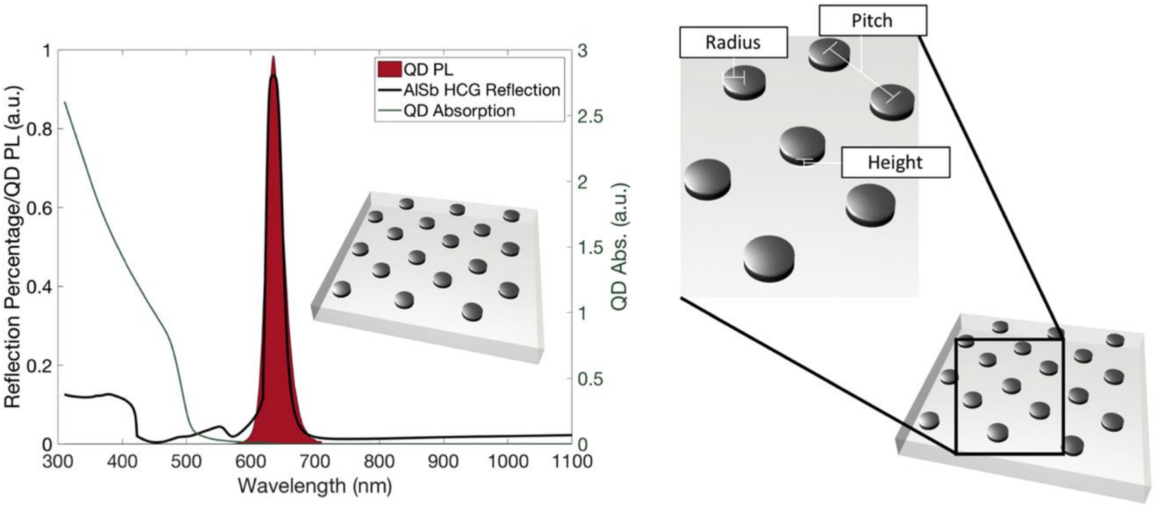

Figure 3.3: Simulated reflection peak of an AlSb HCG reflector overlayed with the relevant QD absorption and photoluminescence properties. The insert shows a schematic of such a hexagonal array, highlighting the radius, pitch, and height that we optimize to induce the given reflection peak.

While this specific AlSb design is for a LSC using CdSe/CdS quantum dots tuned to the band edge of an InGaP microcell, such an AlSb metasurface can be tuned for a variety emitter wavelengths tuned to other photovoltaic band edges. By simply scaling the geometric parameters, one can design a HCG that is spectrally selective at a wide variety of wavelengths. By increasing the geometric parameters, the reflection peak is moved to longer wavelengths. This expands the utility of a spectrally selective HCG reflector for a variety of LSC applications such as stained glass LSCs with a variety of colors, potentially higher efficiency LSCS with GaAs photovoltaics, and building integrated modules operating in the near-infrared spectrum for maximum transparency. Figure 3.4 demonstrates the tunability of an AlSb to the band edge of different photovoltaic materials[12,29,30].

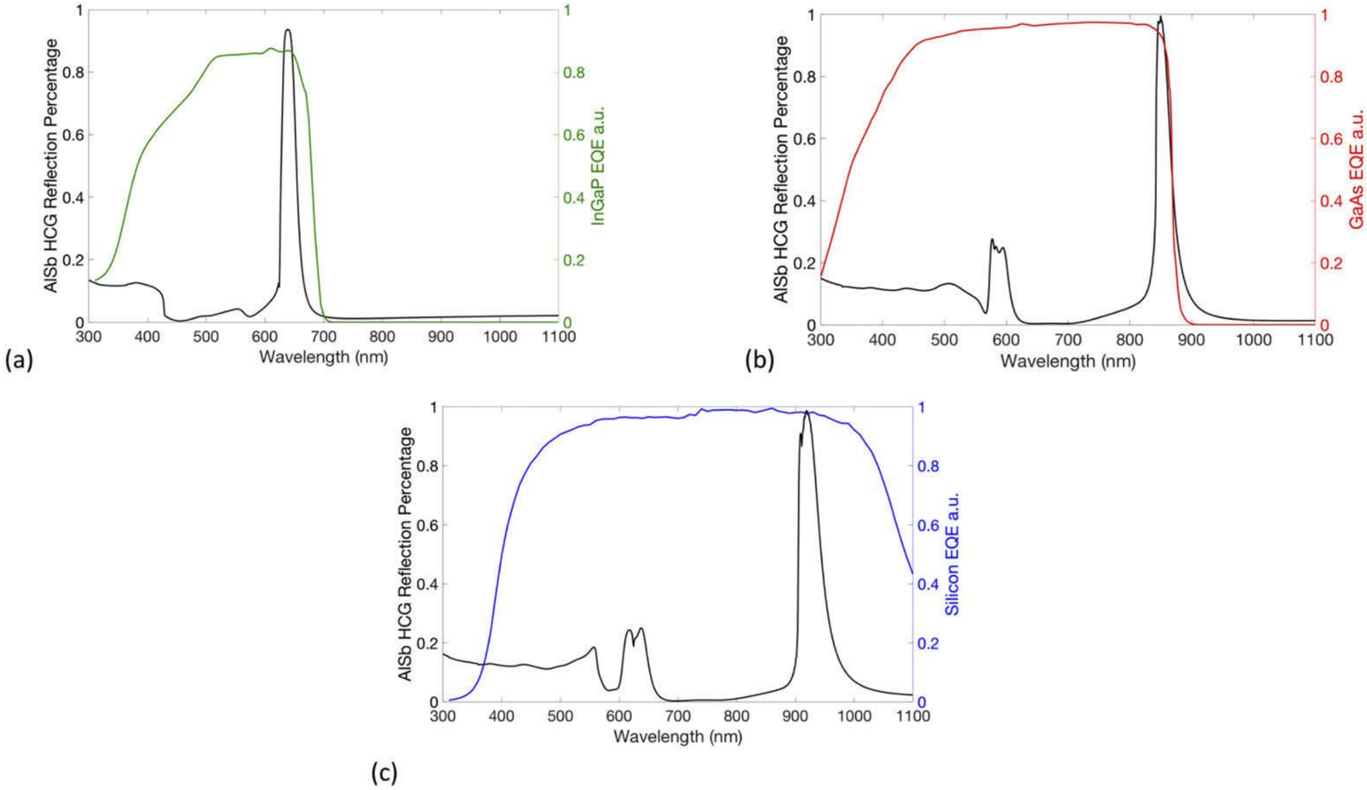

Figure 3.4: An example of how by scaling the pitch, radius, and height of the pillars in a hexagonal array, an AlSb HCG can be tuned to various photovoltaic materials band edges. In (a) we show the reflection peak tuned to the band edge of InGaP. In (b) we show the reflection peak tuned to the band edge of GaAs. In (c) we show the reflection peak tuned to the near IR at the band edge of Si. The peaks in the long wavelength range show more reflection modes in the short wavelength region, but this would not be relevant as a back reflector or potentially when applied to different luminophores with different absorption profiles. The peaks are higher for the longer wavelength band edges due to the AlSb's near zero absorption beyond 700 nm

The greatest challenge that AlSb presents is its fabrication. AlSb is a III-V semiconducting material. III-V semiconductors are typically fabricated via MOCVD, or metal organic chemical vapor deposition. MOCVD is a costly and arduous deposition technique which would ultimately increase the overall module cost beyond what would be competitive for a photovoltaic module. We therefore opted to deposit thin films of AlSb via co-sputtering from separate Al and Sb targets. In addition to the decrease in cost, co-sputtering from separate targets is advantageous for fine control of the stoichiometric properties of the thin film. When sputtering from a bulk AlSb, the stoichiometric properties are already set and therefore the n,k properties are already set and are not necessarily optimal for lossless spectrally selective reflectors. To co-sputter the targets, we used an AJA UHV Orion system designated for chalcogenides. Using a pressure-power-rate table generated by the staff in the Kavli Nanoscience Institute, we started by setting the Al and Sb rates equal to one another at 1 Angstrom/second under a deposition pressure of 1mtorr. The Al target uses a DC power supply, while the Sb target uses a RF power supply. For this specific sputter system, a 1:1 deposition rate ratio corresponded to a power of 120 Watts of DC voltage for the Al target and 48 Watts of RF voltage for the Sb target. We opt for a 1:1 ratio to best promote even growth of AlSb. After deposition, the film is annealed *in situ* at 550 degrees Celsius for one hour to promote crystallization and inhibit oxidation. Annealing beyond one hour did not further improve the film composition. During the annealing of the thin film, there was a continuous flow of Argon at 10 sccm under a pressure of 1 mtorr, matching the conditions of the deposition. The first challenge when working with AlSb was the pervasive oxidation. While annealing *in situ* decreased the rate of oxidation and improved the film composition, it ultimately did not prevent the oxidation from occurring, as shown in Figure 3.5

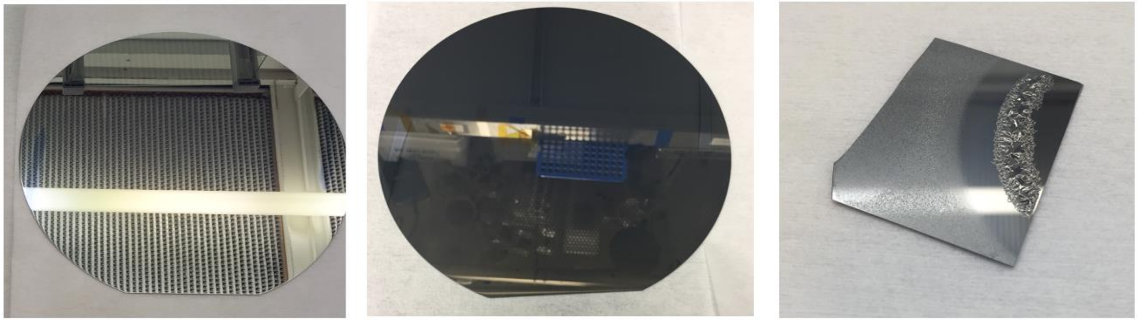

Figure 3.5: Demonstration of the oxidation effects of a co-sputtered AlSb thin film on a Si wafter substrate. The left image is a wafer directly after deposition. The center image is a wafer after 2 hours in oxygen exposure. The right image is a wafer after 2 days of exposure to an ambient environment.

The effects of oxidation is inherently problematic for an optical component that will ultimately be used in a photovoltaic module, exposed to light, air, and other elements like rain. Therefore, we are forced to consider both short term and long term mitigation effects. In the short term, a vacuum suitcase was used to transfer the samples from each tool and all samples were ultimately stored in a glove box. As a long term solution, FDTD simulations were performed for an AlSb high contrast grating with a 10nm cap of SiO_2 as encapsulation layer. These simulations showed that the reflection peak with an encapsulation layer was consistent with previous simulations therefore showing a long term viable solution to the oxidation if it can be inhibited in the analysis process. Furthermore, an SiO_2 cap could be added *in situ* directly after the AlSb deposition step.

In order to fine tune the optimal deposition rate ratio for the separate Al and Sb targets, we started by analyzing via x-ray photoelectron spectroscopy (XPS). XPS uses an x-ray source to measure the binding energy of the materials on the film. XPS is an powerful method for analyzing a film composition because it is capable of not only measuring the amount of material on a surface, but also can show how each material is bonded to one another. However, it was quickly clear that XPS would not be a viable analysis method for films composed of Al, Sb, and O_2. The location of the photoelectron peaks for antimony and oxygen make such a composition analysis virtually impossible. The oxygen 1s peak is located approximately at 531 eV and the antimony 3d5/2 peak occurs at roughly 529 eV for AlSb. Given the sensitivity and full width half max of these energy peaks, they become extremely difficult to differentiate[31]. While possible to use the antimony 3p3/2 peak at 770 eV, we would not be able to analyze the oxidation which is crucial in the analysis of AlSb[31]. Another common way to measure film composition is energy dispersive x-ray spectroscopy (EDS). Rather than using an x-ray source, EDS using an electron source within a Scanning Electron Microscope (SEM) to detect the x-rays scattered from a film based on the photoelectron peaks. This method is quicker and typically more common as it can be performed within a SEM. However, the convolution of the O_2 and Sb peaks is similarly problematic in this analysis as well. Furthermore, without a method like XPS to analyze where the bonds are actually occurring, the EDS data become difficult to disentangle as both

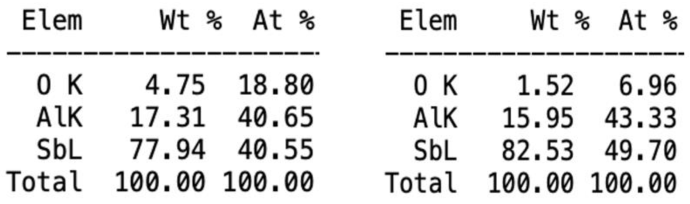

```
Elem     Wt %  At %      Elem     Wt %  At %
---------------------    ---------------------
 O K    4.75  18.80       O K    1.52   6.96
 AlK   17.31  40.65       AlK   15.95  43.33
 SbL   77.94  40.55       SbL   82.53  49.70
Total 100.00 100.00      Total 100.00 100.00
```

Figure 3.6: Two sets of EDS data for thin films with different deposited rates of Al and Sb. While the set on the left has an even ratio of Al to Sb, the oxidation is substantial. The data set on the right has an uneven rate of Al to Sb, but has a much more limited rate of oxidation

Al and Sb are prone to oxidation. Without showing where the oxidation is actually occurring, it can become difficult to adjust a deposition recipe accordingly. Figure 3.6 shows two sets of EDS data and demonstrates why EDS poses a challenge.

Given these setbacks with film composition analyses, we opted for ellipsometry as our figure of merit by which we would tune the deposition recipe. While x-ray analysis methods could provide a film composition, out ultimate figure of merit for a thin film of AlSb is the optical properties of the film. Therefore, we are able to bypass the limitations caused by the convolution of the Sb and O_2 photoelectron peaks. Ellipsometry measures the polarization changes caused by incident light interacting with a surface. From these changes in polarization, a user can fit the data to obtain the optical constants of a film, given a known film thickness. Likewise, a user can obtain the thickness of a film if the optical constants are known. Since we are aiming to obtain the optical constants, we determined the thickness of each measured film via cross-sectional SEM. Figure 3.7 shows an example of such a SEM image.

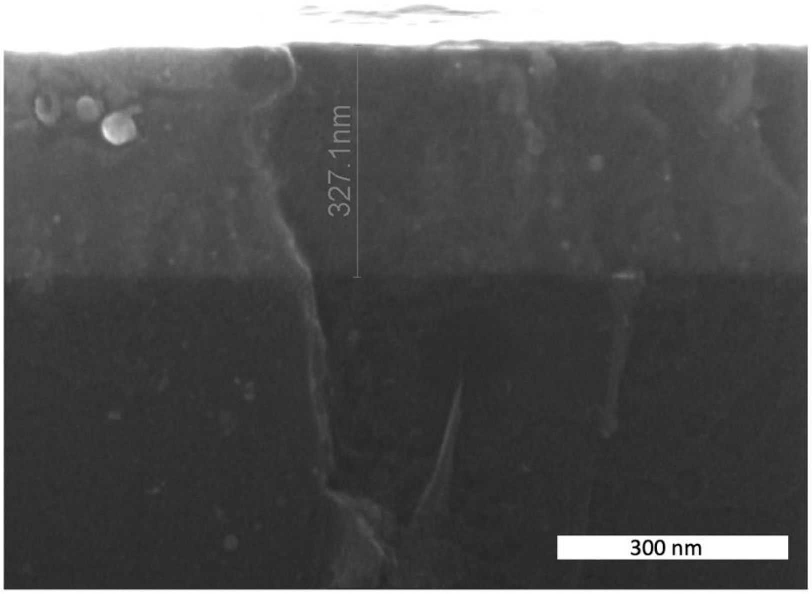

Figure 3.7: Cross-sectional SEM of a thin film of AlSb.

While ellipsometry does not result in a quantitative analysis of the film composition, the resulting qualitative data informs the deposition recipe. If the deposition parameters result in a sample that is stoichiometric Al heavy due to a high Al deposition rate, the n and k data resemble that of aluminum. Likewise, when the stoichiometric ratio is Sb heavy, the n and k data better resemble that of antimony. Only when the deposition rates are nearly even between the Al and the Sb do we observe semiconductor properties such as the appearance of an energy bandgap. Figure 3.8 provides an example of some of the raw n,k data upon which we iterated a deposition recipe. As shown in Figure 3.8, a film that has too much Sb results in n,k data closer to that of Sb or a heavy metal. A film that has too much Al begins to resemble the n,k data of Al or Al_2O_3. From these plots we are able to adjust the deposition rate of the Al and Sb accordingly to fine tune to a ratio promoting the growth of a wide bandgap semiconducting material.

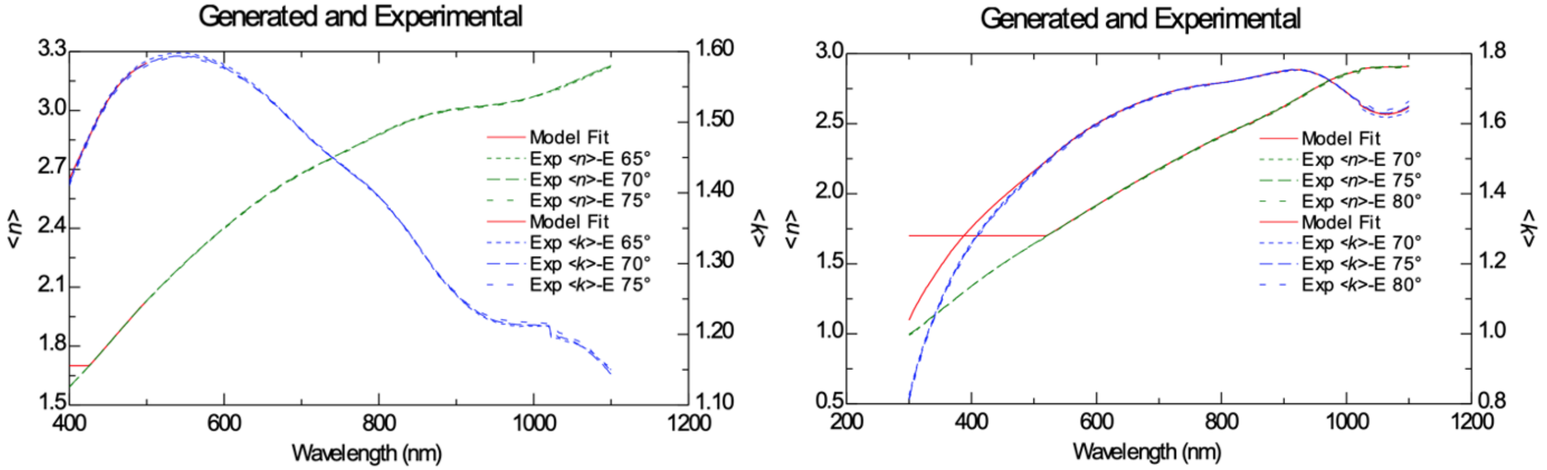

Figure 3.8: Raw fitted n,k data of films with deposited Al and Sb. The film on the left plot is Sb heavy. The film on the right plot is Al heavy.

We unfortunately found that the parasitic oxidation occurred in all films, regardless of initial n,k measurements, and we therefore stored all films in inert environments between depositions and analysis. Even with this careful treatment of samples, oxidation consistently occurred and negatively impacted the n,k behavior of the films by decreasing the index and increasing the extinction coefficient. Upon iterations, it was determined that the optimum rate of Al was 0.8 angstroms per second, corresponding to a power of 100 Watts, and a Sb rate of 1.05 angstroms per second corresponding to a power of 54 Watts. The n,k data of this film is demonstrated in Figure 3.9. The index of refractions is 3.5 and the extinction coefficient is 0.6 at 635 nm.

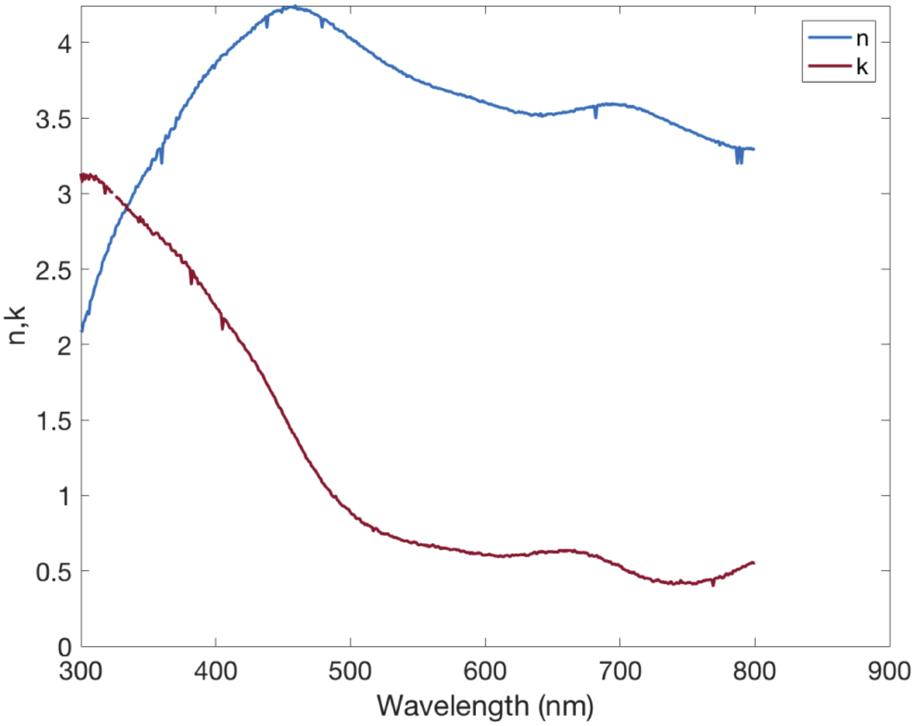

Figure 3.9: Index of refraction and extinction coefficient of a fabricated AlSb thin film stored in an inert environment.

In order to evaluate the potential of AlSb films as high contrast gratings, we incorporated films with the experimentally-determined n,k data from Figure 3.9 in our electromagnetic Lumerical simulations. Figure 3.10 shows maximum theoretical reflection of a high-contrast grating spectrally selective reflector using the experimentally demonstrated n,k data. While we achieve an index of refraction n = 3.5 and, therefore, a high enough value to induce a reflection peak, the absorption coefficient is consistently too high to induce a resonant reflection peak strong enough to serve as a useful spectrally selective reflector to improve the photovoltaic conversion efficiency of LSCs.

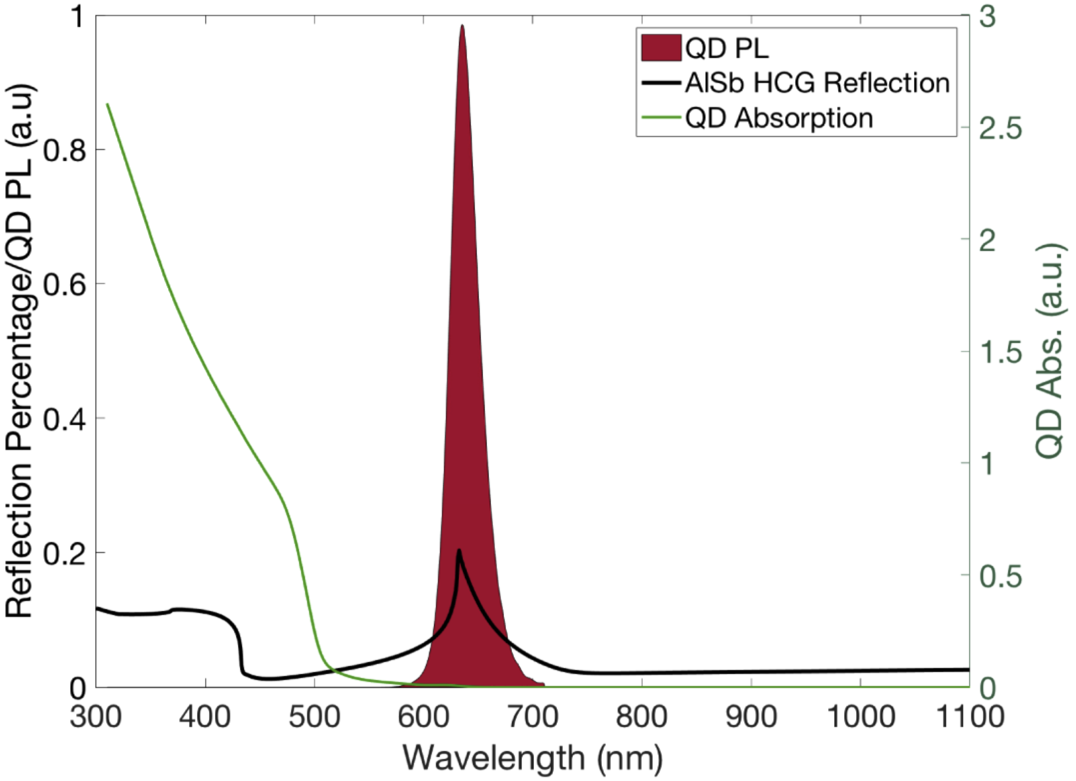

Figure 3.10: FDTD simulation of a HCG using the experimental n,k data from a co-sputtered AlSb film. The reflection peak is 22% at 635 nm and the absorption coefficient is 0.6.

If the extinction coefficient could be decreased closer to the known value for single crystal AlSb films, sputtered films could be used as HCG wavelength selective reflectors. We infer that the co-sputtering process results in AlSb semiconducting thin films with defects and disorder that induce below-bandgap absorption, which is detrimental in high contrast nanophotonics applications. Such defects are shown in Figure 3.11. We found that oxidation begins very soon following film exposure to an ambient environment and causes the film's semiconductor n,k characteristics to become severely degraded. The timescale required for material durability is determined first by the time required to verify the characteristics of the HCG (on the order of hours), and then ultimately by the application deployed in LSC modules (on the order of months-years). The necessary durability of an AlSb film could potentially be achieved via MOCVD or sputtering with forming gas or hydrogen, as these are methods more common in III-V fabrication[32]. However, even with these additional methods, it would be advantageous to employ an environment barrier coating to further inhibit oxidation after ambient exposure.

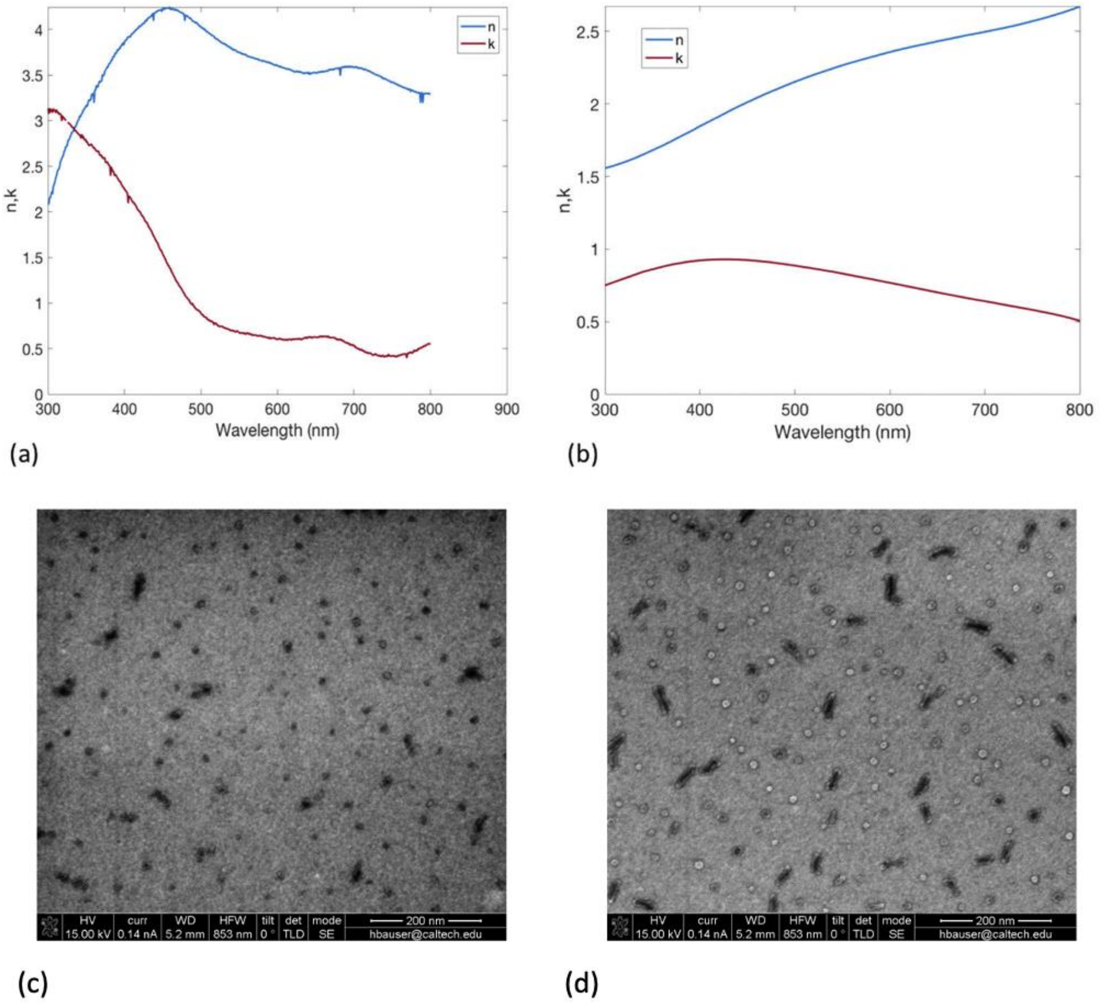

Figure 3.11: A demonstration of the oxidation effects on a thin film of sputtered AlSb. (a) shows the n,k data of a thin film kept in an inert atmosphere. (b) shows the n,k data of the same thin film after terminally oxidizing. (c) is a SEM image of the thin film producing the n,k data in (a). Likewise, (d) shows the same film after terminally oxidizing. The index of refraction decreases and the extinction coefficient increases. The defects on the film also expand and morph after undergoing oxidation.

3.4 a-SiC:H High Contrast Grating Reflectors

After realizing the limitations of AlSb as a HCG material, we pivoted to hydrogenated amorphous silicon carbide (a-SiC:H). a-SiC:H is also a wide bandgap semiconducting material, but is usually deposited via low-cost PECVD as opposed to III-Vs which are often deposited via costly MOCVD. While a-SiC:H was considered as a HCG material before, most data available showed too high of an absorption co-efficient to fully make the case for a-SiC:H as a HCG material when compared to materials like AlSb that are theoretically more lossless. However, a study by Boccard and Holman showed that by using a mixture of silane, methane, and hydrogen a-SiC:H films can become virtually lossless beyond 590 nm while maintaining an index of refraction above 3 across the QD photoluminescence spectrum[33]. Figure 3.12 shows the n,k data of a PECVD deposited a-SiC:H film. During PECVD, when the Hydrogen flow is increased, the index of refraction increases significantly, but with this increase also comes an increase in the absorption coefficient. Increasing the flow of methane however results in a lower index of refraction, but creates the lossless property needed for applications in the visible range.

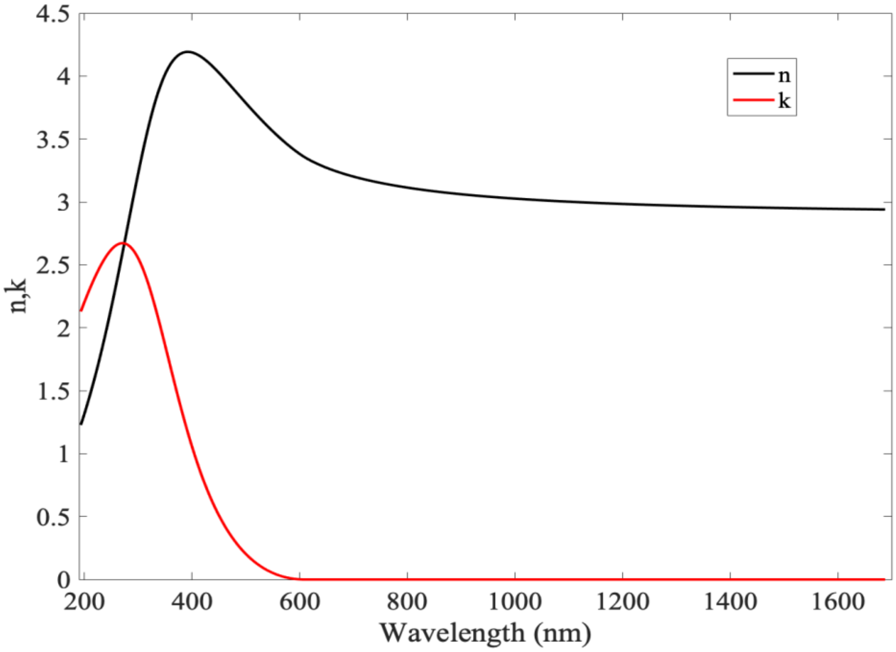

Figure 3.12: Index of refraction and absorption coefficient of a-SiC:H measured via spectroscopic ellipsometry.

The Lumerical FDTD simulation details match the description given in section 3.3, but instead of using the n,k data of AlSb, we of course use the n,k data measured via ellipsometry from the deposited a-SiC:H films. Likewise, the reflection behavior depends on the geometric parameters of radius, thickness, and pitch of the hexagonal nanopillar array. Due to the lossless regime of a-SiC:H appearing at such a comparatively short wavelength, the potential of a-SiC:H for high contrast applications in the visible range extends far beyond those of the just the tandem LSC. Figure 3.13 demonstrates the tunability of a spectrally selective a-SiC:H HCG reflector. The a-SiC:H HCG is not only able to achieve highly efficient reflectivity beyond the lossless region of >600 nm, but also maintains compelling reflective responses as low as 500 nm, demonstrating optical applications throughout nearly the entire visible spectrum.

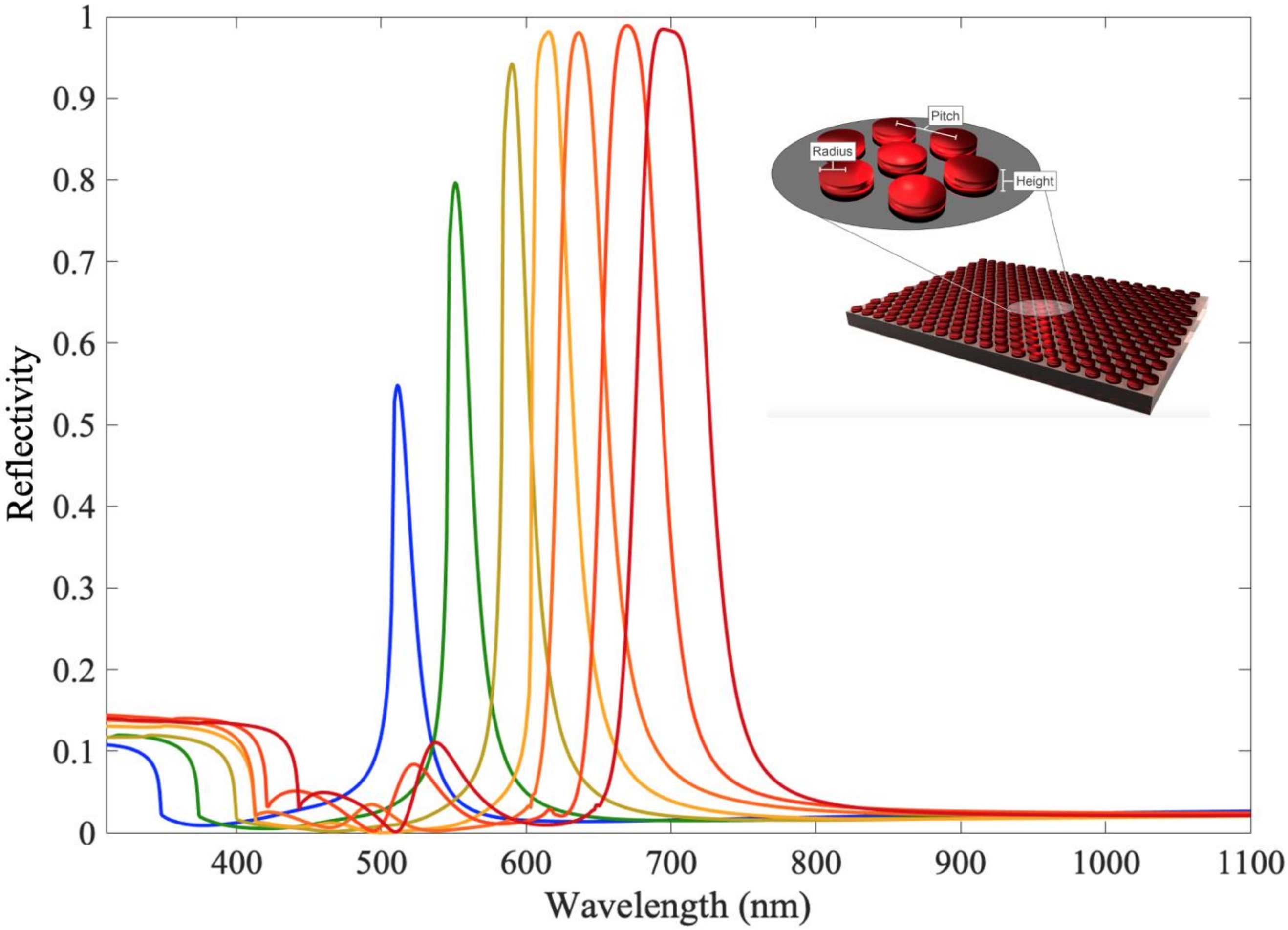

Figure 3.13: Demonstration of how adjusting the geometric parameters of the high contrast grating reflector (pitch, radius, and thickness) shifts the resonance wavelength. By decreasing the geometric parameters, we can tune resonances down to 500nm. By increasing the geometric parameters, we can observe resonance to the edge of the visible spectrum.

Given that we are aiming to design a HCG that is spectrally selective about the photoluminescence of a CdSe/CdS QD, we optimize to reflect 635nm. Given our target reflectance spectrum, we determine the optimal pitch, pillar radius, and pillar thickness to be 475nm, 125nm, and 120nm, respectively. These parameters result in a reflection plot shown in Figure 3.14, where the reflection peak is 97.8% at the QD emission wavelength of 635nm.

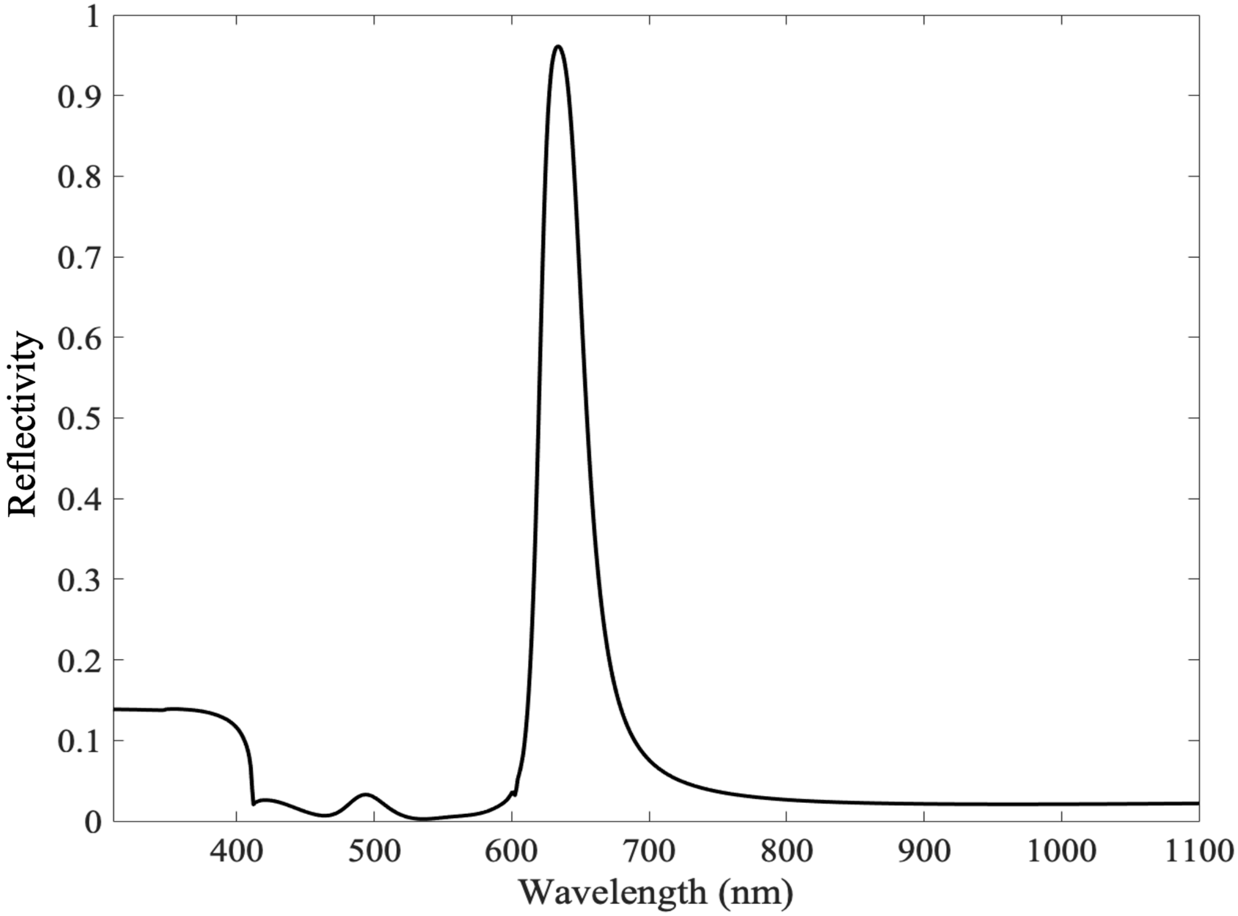

Figure 3.14: Simulated a-SiC:H high contrast reflector with a reflectivity of 97.8% at 635nm, matching the emission of a CdSe/CdS quantum dot.

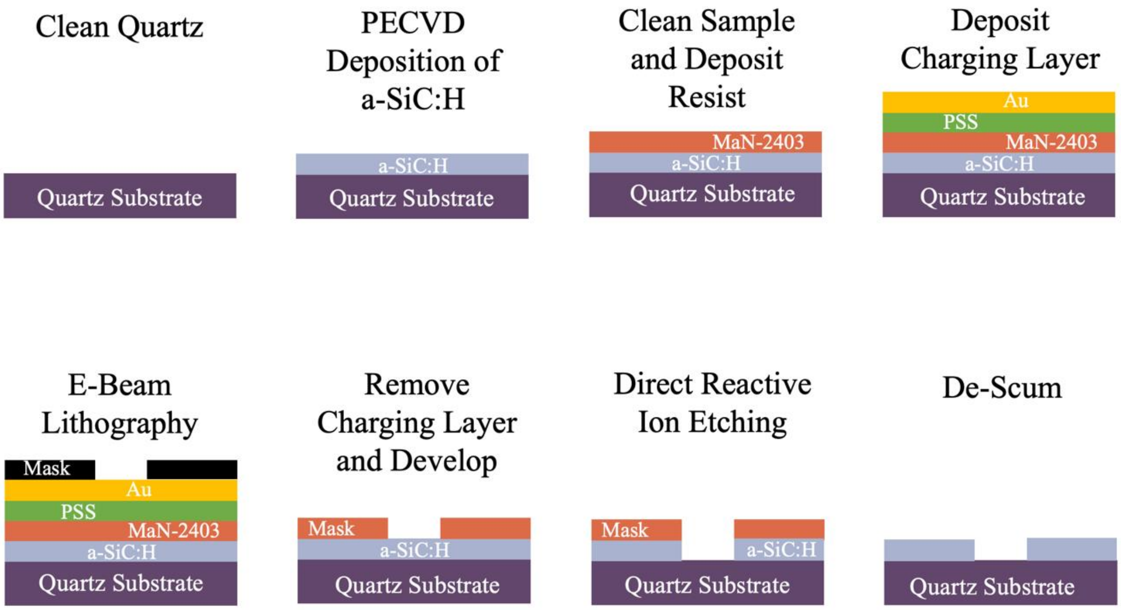

Figure 3.15: Schematic of fabrication steps for a spectrally selective a-SiC:H reflector.

In order to fabricate the sub-wavelength geometric features necessary to induce the desired optical response, we must perform e-beam lithography to write the desired nanopillar pattern into the a-SiC:H thin film. A schematic of the fabrication process is shown in Figure 3.15.

We received disks of quartz with a 150 nm thin film of a-SiC:H deposited onto the films via PECVD. We received the films at a greater thickness than required so that we could fine tune the thickness upon receiving samples. In order to achieve the desired thickness, we removed layers of the a-SiC:H via plasmatherm RIE. The layer removal parameters for the RIE is a gas flow of 50 sccm of CF_4 under a pressure of 40 mtorr and 80 Watts of applied power. The temperature of the tool is set to 25 degrees Celsius. The etch rate is roughly 35 nm/min, though this is not always reliable for short etches (<20 seconds) because the tool takes about 15 seconds into the process to fully settle and function as programmed. Through this etch step, we were able to analyze HCGs at a range of thicknesses from 105-150nm in order to determine the fabricated optimum thickness. Thickness was measured using spectroscopic ellipsometry with a Cody-Lorentz fit. The n,k data used in this model was the n,k data measured after PECVD deposition. In order to perform e-beam lithography, we choose a negative tone resist to maximize tool use efficiency. The negative resist MaN-2403 has substantial issues with sample adhesion. In order to overcome this, before applying the resist the sample was dipped in IPA and Acetone, and then set on a hot plate for 2 minutes at 180 degrees Celsius. After the cleaning step, we applied MaN-2403, via spincoating onto the sample at a rpm of 3000 for 30 seconds. After applying the resist, we applying a charging layer. A charging layer is a necessity for any e-beam lithography performed on an insulating substrate, otherwise the pattern will completely deform. An example of pattern disfiguration via surface charging is shown in the Appendix Figure A.4. A common method to overcome destructive charging is the deposition of a layer of metal directly onto the resist. After exposure, the metal layer can be removed with TMAH. However, this method does not work if the resist develops in base as TMAH is a strong base that will quickly overdevelop any pattern. Since MaN-2403 is a base developing resist, we cannot simply apply a charging metal onto the resist. We instead use a method initially demonstrated by Ng et. al[19]. Instead of depositing the metal directly onto the resist, we instead spincoat a solution of 99% poly(4-stryenesulfonic acid) and 1% Triton X-100 surfactant directly onto the resist. This solution acts as a water soluble sacrificial layer upon which 10 nm of Au is deposited via thermal evaporation. The Au acts as a conductive agent to prevent charging and warping of the desired pattern. The array was written with a Raith 5200 electron beam writer with and electron source set at 100kV. The current of the beam was set to 5nA and the dose was $340\mu C/cm^2$. This dose is substantially lower than previous reported doses for the resist. This is based off of a change in the BEAMER software where doses wrote in the spiral mode were uniformly decreased. After the pattern was written, the Au and sacrificial layer were removed by a 1 minute water bath. The array was then developed in MF-319, a base developer, for 1 minute. The array was etched using an Oxford ICP-RIE with a pseudo-Bosch SF_6/C_4F_8 process using a forward power of 1500W and a 32W ICP power with a gas flow of 22 sccm of SF_6 and 30 sccm of C_4F_8. The remaining resist was then removed via O_2 plasma for 20 minutes at a pressure of 20 mTorr, power of 80W, and flow of 20 sccm.

Upon fabrication, the sample’s reflection is measured via a supercontinuum laser light source coupled with a monochromater to provide a narrow spot size (~10 μm) around each wavelength. Reflection measurements were taken between 450nm and 1100nm at normal incidence. Non-polarizing beam splitters were used to direct the reflected beam to a Si photodiode. A NIST Specular Reflectance Standard mirror is used to normalize raw reflectivity data thus removing the frequency-dependence of many optical components in the set-up. Using the absolute reflectivity of the mirror provided by the manufacturer, we were able to obtain accurate absolute reflectivity spectra for each measurement.

Figure 3.16 shows an optimized HCG with a reflection peak of 94.3% at the maximum, and 92% at the QD peak of 635 nm. The SEM image includes an 8nm layer of Chromium as a charging layer. Furthermore, over 94% of the QD emission spectrum is encased in the HCG reflection profile. Previous studies have showed that a reflection profile that encases the total emission is a more efficient reflector than one that has a higher maximum reflection with a smaller full width half maximum[34]. There are slight deviations in the resonance behavior of the fabricated HCGs compared to the simulation parameters. The radius was consistent with the simulation determining that 125 nm remains the optimal pillar radius. The reflection behavior was significantly more sensitive to the a-SiC:H thickness in fabrication than it was shown to be in the simulations. Previous studies and simulations show that when a HCG is too thick, multiple resonances appear, however if the HCG is too thin resonance will be weak24,26. While simulations suggest that 120 nm would be the ideal thickness, the optimized fabricated thickness is found to be 128nm. The largest variation between simulation and theory was the pitch. The fabricated optimized sample had a pitch of 455nm between the pillars whereas the simulated optimum pitch was 475nm. We found in our studies that a higher fill fraction generally resulted in a stronger resonance for fabricated HCG reflectors. These variations in geometric parameters are in part due to the spot-size of the reflectance measurements integrating across the entire 700umx700um area of the fabricated HCG. The FDTD simulation assumes infinite repetition of identical unit cells of the HCG. While integrating across the area of the fabricated HCG reflector includes imperfections on the HCG surface contributing to the variation in the optimal geometric parameters, opting for the full area measurement demonstrates a more realistic reflector performance.

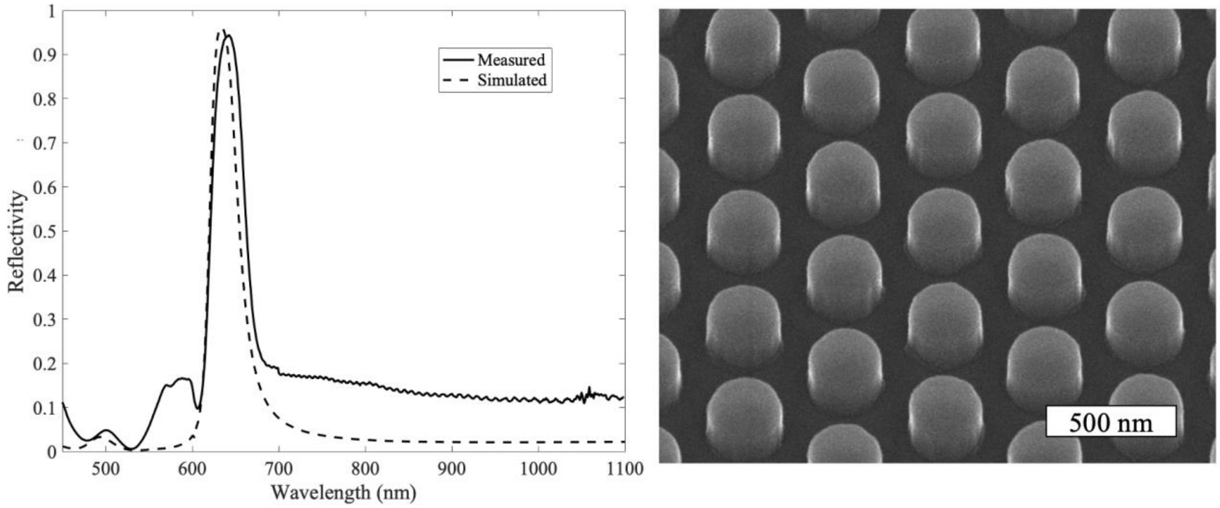

Figure 3.16: The left shows the reflection profile of a fabricated a-SiC:H spectrally selective reflector. The right is a SEM image of the hexagonal nanopillar array comprising the a-SiC:H reflector.

One promising factor previously mentioned is that the peak of the reflector can be shifted by altering the geometric features of the hexagonal array. While during this work we did not intentionally explore this, we did find that larger geometric features resulted in red shifted peaks. Likewise, smaller geometric features resulted in blue shifted peaks. Figure 3.17 shows this behavior. While neither of these peaks are optimized, Figure 3.17 demonstrates how such a HCG can be shifted to reflect at wavelengths throughout the visible spectrum, making a-SiC:H a promising material in the field of high contrast visible spectrum nanophotonics.

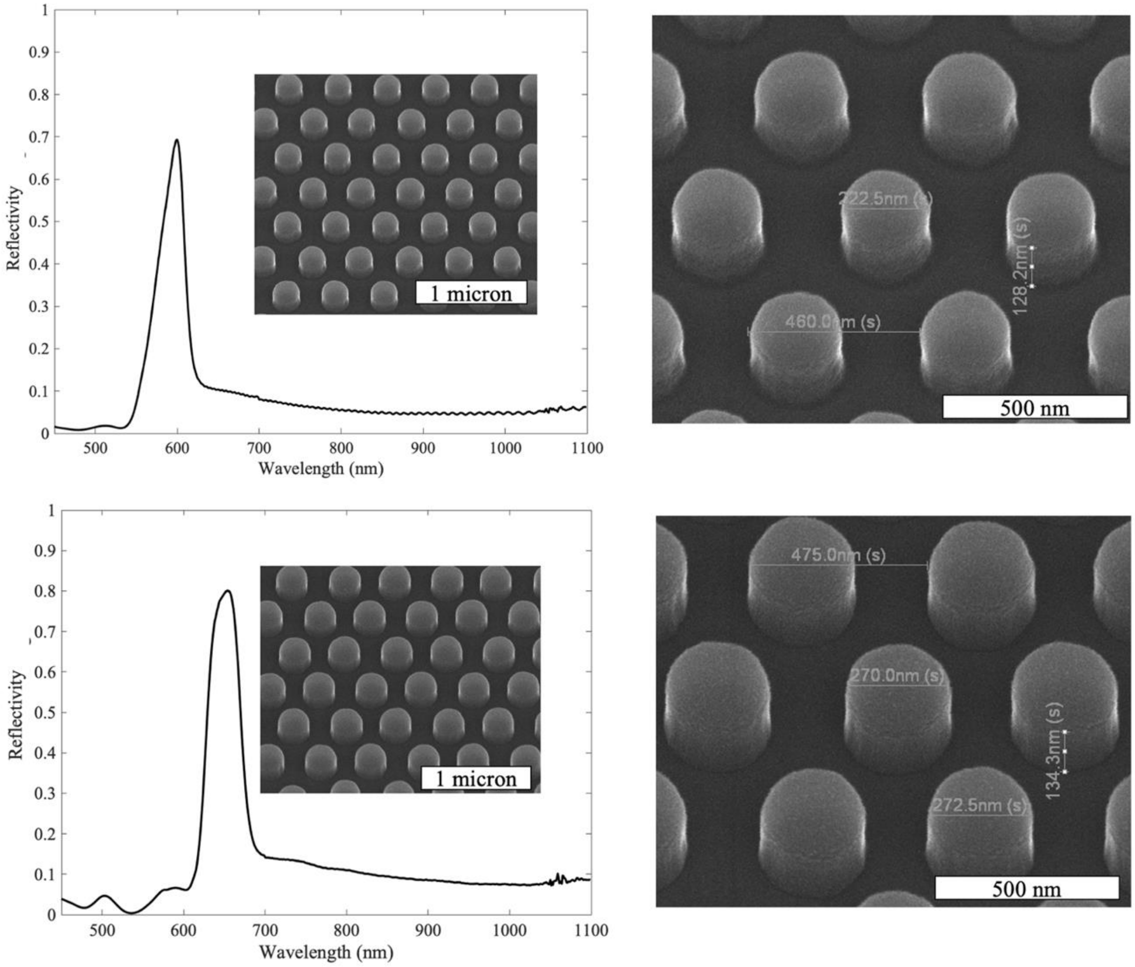

Figure 3.17: Measured reflectivity of a-SiC:H HCGs not optimized to reflect at 635nm. In the top image we see that the smaller features of the grating generate a reflection peak at 600nm. Likewise, in the bottom image we see that the larger geometric features of the grating generate a reflection peak at 675 nm.

3.5 Discussion

In this chapter, we have explored two different materials to act as a bottom mirror in a tandem LSC. AlSb ultimately was too absorbing to be an efficient reflector. We designed and fabricated an a-SiC:H spectrally-selective high-contrast grating tuned to reflect the emission of highly efficient CdSe/CdS QDs with an emission band centered around 635nm. Furthermore, we have demonstrated via FDTD simulation high reflectivity resonance peaks across the visible spectrum using spectrally-selective HCGs comprised of a hexagonal array of a-SiC:H nanopillars. While the presented experimentally validated example is specific to reflect QDs with emission tuned at 635nm, our work demonstrates the material's potential for many low-loss high index applications in the visible spectrum beyond LSCs.

Despite the successful reflectance of the a-SiC:H, by including mirrors in the LSC, we are adding additional costs and weight. Furthermore, the fabricated a-SiC:H reflector maintains too high of a reflectivity in the long wavelength range for integration in a tandem LSC module which relies on light travelling through the LSC component to the Si subcell. Further optimization of the etch process could aid in this limitation. Any future work could run more precise etch parameters sweeps ultimately aimed at eliminating all remaining a-SiC:H from the surface outside of the nanopillar array of the HCG that could potentially contribute to the added reflection in the long wavelength region. It is ultimately advantageous to eliminate as many LSC components as possible while maintaining efficiency. Therefore, the impact of this work will be more broadly to the visible spectrum nanophotonics community than for our specific LSC purpose.

References

1. Peng, W., Wu, H. "Flexible Stretchable Photonic Sensors Based on Modulation of Light Transmission," *Advanced Optical Materials* **2019**, 7, 1900329.

2. Parimi, P., Lu, W., Vodo, P. *et al.* "Imaging by Flat Lens Using Negative Refraction," *Nature* **2003**, 426, 404.

3. Camayad-Munoz, P. Ballew, C., Roberst, G. Faraon, A. "Multifunctional Volumetric Meta-Optics for Color and Polarization Image Sensors," *Optica* **2020**, 7, 4, 280-283.

4. Xu, J., Cua, M., Zhou, E.H., Horie, Y., Faraon, A., Yang, C. "Wide-Angular-Range and High-Resolution Beam Steering by a Metasurface-Coupled Phase Array," *Optics Letters* **2018**, 43, 21, 5255-5258.

5. Kish, F., *et al* "From Visible Light-Emitting Diodes to Large-Scale III-V Photonic Integrated Circuits," *Proceedings of the IEEE* 2**013,** 101, 10, 2255-2270.

6. Lu, X., Li, Q., Westly, D.A., Moille, G., Singh, A., Anant, V., Srinvasan, K. "Chip-Integrated Visible-telecom Entangled Photon Pair Source for Quantum Communication," *Nature Physics* **2019**, 15, 373-381.

7. Tan, S., Yang, F., Boominathan, V., Veeraraghavan, A., Naik, G.V. "3D Imaging Using Extreme Dispersion in Optical Metasurfaces," *ACS Photonics* **2021**, 8, 5, 1421-1429.

8. Chang-Hansain, C.J., Yang, W. "High-Contrast Gratings for Integrated Optoelectronics," *Advanced Optical Photonics* **2012,** 4, 379-440.

9. M. Khorasaninejad, W. T. Chen, R. C. Devlin, J. Oh, A. Y. Zhu, and F. Capasso, "Metalenses at Visible Wavelengths: Diffraction-limited Focusing and Subwavelength Resolution Imaging," *Science* **2016**, 352, 6290, 1190–1194.

10. B. Cheong, O. N. Prudnikov, F. Cho, H. Kim, J. Yu, Y. Cho, H. Choi, and S. T. Shin, "High Angular Tolerant Color Filter Using Subwavelength Grating," *Applied Physics Letters* **2009**, 94, 21.

11. M. Niraula, J. W. Yoon, and R. Magnusson, "Single-layer Optical Bandpass Filter Technology," *Optics Letters* **2015,** 40, 21, 5062–5065.

12. Needell D.R. *et al* "Design Criteria for Micro-Optical Tandem Luminescent Solar Concentrators," *IEEE Journal of Photovoltaics*, **2018** *8* 1560-1567.

13. M. Niraula, J. W. Yoon, and R. Magnusson, "Single-layer Optical Bandpass Filter Technology," *Optics Letters*, **2015,** 40, 21, 5062–5065.

14. W. Yang, S. Xiao, Q. Song, Y. Liu, Y. Wu, S. Wang, J. Yu, J. Han, and D. P. Tsai, "All-dielectric Metasurface for High Performance Structural Color," *Nature Communications* **2020,** 11,1, 1864.

15. P. Camayad-Munoz, C. Ballew, G. Roberst, and A. Faraon, "Multifunctional Volumetric meta-optics for Color and Polarization Image Sensors," *Optica* **2020,** 7,4, 280–283.

16. H. Sroor, Y. Huang, B. Sephton, D. Naidoo, A. Valles, V. Ginis, C. Qiu, A. Ambrosio, F. Capasso, and A. Forbes "High-purity Orbital Angular Momentum States from a Visible Metasurface Laser," *Nature Photonics* **2020,** 14,8, 498–503.

17. M. L. Tseng, H. Hsiao, C. H. Chu, M. K. Chen, G. Sun, A. Liu, and D. P. Tsai, "Metalenses: Advances and Applications," *Advanced Optical Materials* **2018,** 6,18), 1800554.

18. R. J. Lin, V. Su, S. Wang, M. K. Chen, T. L. Chung, Y. H. Chen, H. Y. Kuo, J. Chen, J. Chen, Y. Huang, J. Wang, C. H. Chu, P. C. Wu, T. Li, Z. Wang, S. Zhu, and D. P. Tsai, "Achromatic Metalens Array for Full-colour Light-field Imaging," *Nature Nanotechnology*, **2019,** 14,3, 227–231.

19. Ng, R. C., Garcia, J.C., Greer, J.R., Fountaine, K.T. “Polarization-Independent, Narrowband, Near-IR Spectral Filters via Guided Mode Resonances in Ultrathin a-Si Nanopillar Arrays,” *ACS Photonics* **2019**, 6, 265-271.

20. Iyer, P.P., Butakov, N.A., Schuller, J.A. “Reconfigurable Semiconductor Phased-array Metasurfaces,” *ACS Photonics* **2015**, 2, 8, 1077-1084.

21. Wriedt, T. Mie Theory: A Review. In: Herget, W., Wriedt, T. “The Mie Theory” *Springer Series in Optical Sciences* Berlin, Germany, vol 169 **2012**.

22. Ding, Y., Magnusson, R. “Band Gaps and Leaky-wave effects in Resonant Photonic-crystal Waveguides,” *Optics Express* **2007**, 15, 680-694.

23. Wu, Y., Yang, W., Fan, Y., Song, Q., Xiao, S. “TiO_2 Metasurfaces: From Visible Planar Photonics to Photochemistry,” *Science Advances* **2019**, 5, 11.

24. Aspnes, D.E., Stunda, A.A., “Dielectric Functions and Optical Parameters of Si, Ge, GaP, GaAs, GaSb, InP, InAs, and InSb from 1.5 to 6.0 eV,” *Physical Review Letters B* 1**983**, 27, 2.

25. N. M. Estakhri, V. Neder, M. W. Knight, A. Polman, and A. Alu, “Visible Light, Wide-angle Graded Metasurface for Back Reflection,” *ACS Photonics* **2017,** 4,2, 228–235.

26. X. Buet, D. E. Belharet, F. Lozes-Dupuy, A. Monmayrant, and O. Gauthier-Lafaye, “High Angular Tolerance and Reflectivity with Narrow Bandwidth Cavity-resonator-integrated Guided-mode Resonance Filter,” *Optics Express* **2012,** 20,8, 9322.

27. Darbe, S., Atwater, H.A.“Resonant Dielectric High-contrast Gratings as Spectrum Splitting Optical Elements for Ultrahigh Efficiency (>50%) photovoltaics*” 2015 PVSC, 42nd Conference Proceedings,* **2015**.

28. S. Zollner, C. Lin, E. Schonherr, A. Bohringer, and M. Cardona, “The Dielectric Function of AlSb from 1.4 to 5.8 eV Determined by Spectroscopic Ellipsometry,” *Journal of Applied Physics* **1989** 66,1, 383–387.

29. M. A. Green, Y. Hishikawa, W. Warta, E. D. Dunlop, D. H. Levi, J. Hohl-Ebinger, and A. W. Ho-Baillie, “Solar Cell Efficiency Tables (version 50),” *Progress in Photovoltaic Residential Applications* **2017,** 25,7, 668–676.

30. Theing, S., *et al*, “Luminescent Solar Concentrator Tandem-on-silicon with Above 700mV Passivated Contact Silicon Bottom Cell,” PVSC, 46th Conference Proceedings **2019.**

31. Moulder, J. F. "Handbook of X-Ray Photoelectron Spectroscopy: A Reference Book of Standard Spectra for Identification and Interpretation of XPS Data (Perkin-Elmer Corporation," **1992**.

32. Geisz J.F. and Friedman, C.J. "III-N-V Semiconductors for Solar Photovoltaics Applications," *Semiconducting Science Technology* **2002,** 17,8, 769–777.

33. Boccard, M.; Holman, Z. C. "Amorphous Silicon Carbide Passivating Layers for Crystalline-silicon-based Heterojunction Solar Cells," *Journal of Applied Physics* **2015**, 118 (6), No. 065704.

34. Bauser, H.C., Needell, D.R., Bukowsky, C.R., Ilic, O., Nett, Z., Lee, B.G., Geisz, J.F., Alivisatos, A.P., Atwater, H.A. "Metasurfaces as Wavelength Selective Mirrors in Tandem Luminescent Solar Concentrators" *2018 IEEE 45th Photovoltaic Specialist Conference (PVSC)* **2018.**

Chapter 4

PHOTONIC CRYSTAL WAVEGUIDES FOR LUMINESCENT SOLAR CONCENTRATORS

4.1 Introduction to Photonic Crystal Waveguides

Chapter 1 gave an overview of some of the concepts upon which the study of photonic crystals are built. In this chapter, we will discuss the methods by which photonic crystals can trap and guide emission and propose highly efficient emission trapping designs. This is an alternative to the macro-scale polymer waveguides utilized in the first generation of the tandem LSC as both the dispersion medium for the QDs and the primary trapping method for the QD emission. Guided modes in photonic crystal waveguides (PCWGs) have been extensively studied and experimentally realized for applications in magnetic mode control, nonlinear optics, high quality resonators, on-chip photonic lasers, and LSCs[1-8]. PCWGs are capable of guiding emitted light into waveguide modes within the PCWG structure, thus, increasing the optical efficiency of waveguides for LSCs without external reflection components[1-9]. When a QD is embedded in a micron scale polymer waveguide, the emission is trapped via TIR and can be analyzed via ray-optical calculations[10]. This is not the case for a QD coupled to a photonic crystal waveguide. PCWGs trap the TE and TM modes of luminophore emission by increasing the local density of optical states (LDOS) available to an emitter[9]. The emission couples into the LDOS of the PCWG, remaining within the PCWG[9,11]. For the purposes of light trapping in LSCs, we consider the 2-D PCWG that is periodic in the *x* and *y* plane with a defined thickness, *t*, in the *z* plane. The translational symmetry in the *x*-*y* plane forces the modes to be oscillatory without restriction of the wave vector in the *z* direction. If a mode is guided, it has a wave vector of zero in the z direction, meaning that all light is propagating in the plane of the PCWG. 2-D photonic crystals are typically consist of either a periodic array or rods, or a periodic array of holes. A general rule for 2-D photonic crystals is that a rod array generates a photonic bandgap in the TM modes, whereas a hole array generates a photonic bandgap in the TE modes[9,12,13]. The goal of a PCWG in the case of the LSC, is to trap as much QD emission as possible within the plane of the PCWG, agnostic to specific modality. We will therefore be considering both designs, a hole array and a rod array. In order to maximize the fill fraction of our PCWG, we will be again opting for hexagonal arrays of both variations of 2-D PCWGs. The periodicity of the hexagonal 2-D PCWG is determined by the following lattice and reciprocal lattice vectors.

$$a_1 = \frac{a}{2}(\hat{x} + \hat{y}\sqrt{3}), \qquad a_2 = \frac{a}{2}(\hat{x} - \hat{y}\sqrt{3}) \tag{4.1}$$

$$b_1 = \frac{2\pi}{a}(\hat{x} + \frac{\hat{y}}{\sqrt{3}}), \qquad b_2 = \frac{2\pi}{a}(\hat{x} - \frac{\hat{y}}{\sqrt{3}}) \tag{4.2}$$

Through these vectors, we can create the irreducible Brillouin zone of the hexagonal PCWG, by which we define the PCWG's symmetry.

4.2 The Case for Photonic Crystals LSCs

In all previous LSC designs, there are inherent loss mechanisms in every component. Increasing the number of components in the LSC simply adds more loss factors that build upon one another inducing paths for decreased efficiency as light travels through the structure. While the fabricated HCG reflectors demonstrated in Chapter 3 high strong reflectivity, they ultimately still contain loss mechanisms in the longer wavelength range of the incident solar spectrum. Furthermore, lossy Bragg filters still must be used as a top filter in the tandem LSC design. In addition to increasing loss mechanisms, the incorporation of both a top and bottom mirror adds cost, thickness, and weight to the overall module. While the cost addition is ultimately beneficial at the current LSC design iteration and application due to the added light trapping, designing a method to trap the light without external reflectors could make the cost even more competitive. Furthermore, by decreasing the thickness and weight of the module by removing external reflectors could expand the applications beyond tandem LSCs to building-integrated or space solar power modules.

Another promising component of PCWGs for LSCs is the effect the increased LDOS can have on the QDs. Deriving from Fermi's Golden Rule, placing a QD emitter in a nanostructured environment with a large LDOS enhances the spontaneous emission into specific optical modes relative to the emission to free space[9,14-19]. This phenomenon is called the Purcell enhancement and the quantification of this spontaneous emission is called the Purcell factor, F_P[14]. The Purcell factor, defined in Equation 4.3 quantifies the proportional increase in the spontaneous rate of emission of a dipole as a function of the environment in which the emitter is placed.

$$F_p = \frac{3}{4\pi^2}\left(\frac{\lambda_{free}}{n}\right)^3\left(\frac{Q}{V}\right) \tag{4.3}$$

V is the mode volume within the crystal, λ_{free}/n is the wavelength within the PCWG, and Q is the quality factor of the PCWG defined in Equation 4.4.

$$Q = \frac{2\pi f_0 E}{P} \tag{4.4}$$

f_0 is the frequency within the photonic crystal, E is the energy within the photonic crystal, and P is the dissipated power within the PCWG. In our simulation, we use Equation 4.3 and the simulated emission power from various coupling locations within the PCWG to determine F_P. Within Lumerical, the calculation of the Purcell factor is simplified to the ratio of the dipole power within the PCWG to the dipole power in free space[15-18]. Due to the detailed balance between photon absorption and emission, the converse is also true: emission into lossy modes and/or excited carrier thermalization losses can be reduced[18-22.] Nonradiative losses are reduced, and therefore increase the PLQY of the QDs. Equation 4.5 demonstrates this increase in PLQY.

$$PLQY_{enhanced} = \frac{F_p * PLQY_0}{F_p * PLQY_0 + (1 - PLQY_0)} \tag{4.5}$$

This increase in PLQY can have significant effects on the overall performance of a LSC. The effects on PLQY are shown in Figure 4.1

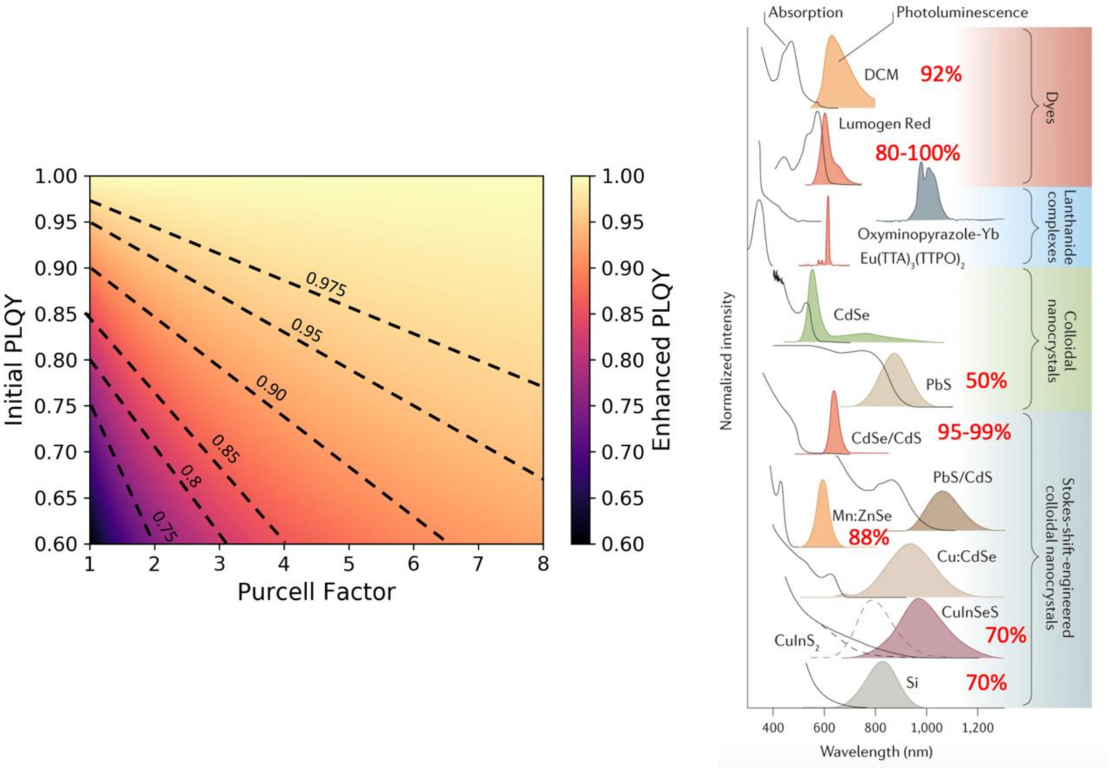

Figure 4.1: The left shows the enhancement of QD PLQY as a function of the Purcell factor given by Equation 4.5. The right figure is adapted from Meinardi *et al* and shows the emission wavelength and general PLQYs for various LSC luminophores[23].

By placing the QD in a photonic crystal with a modest Purcell factor (3-5), high efficient QDs (PLQY > 90%), such as the CdSe/CdS dots, can exhibit PLQYs approaching unity. A similarly modest Purcell factor can increase the performance of less efficient QDs (PLQY < 70%) to ~80-97%. Likewise, if we can achieve higher Purcell factors (>8), such lower performing QDs can achieve PLQYs above 90%. This is particularly promising for building-integrated LSCs which rely on luminophores emitting in the near-infrared. As shown in Figure 4.1, near-infrared emitting QDs typically suffer from lower PLQYs, but are important for building-integrated LSCs to maintain transparency[23].

Lastly, photonic crystals by definition are periodic. Particularly photonic crystals designed without intentional defects. The uniformity allows PCWGs to potentially be fabricated via nano-imprint lithography, facilitating a scalable and low-cost fabrication method.

4.3 High Trapping Efficiency Designs

We consider two types of 2-dimensional photonic crystals: the rod array and hole array. Both PCWGs are comprised of a-SiC:H on quartz. The case for using a-SiC:H with CdSe/CdS QDs was given Chapter 3, but to summarize, a-SiC:H is a compelling material for PCWGs because it maintains a high index of refraction while becoming virtually lossless at the photoluminescence peak of the QDs[24]. The high index of refraction not only leads to potentially higher trapping efficiencies than lower index material, but also increases the potential Purcell factor achievable in a PCWG. In order to design an experimentally realizable LSC system, the photonic crystal design should consider realistic materials properties and fabrication limitations related to the slab thickness and QD location within the waveguide. It has previously been shown that a z mirror symmetric 2D photonic crystal slab in air maximizes mode confinement and, in turn, achieves minimal light leakage[9,11]. Here we must include a substrate on which the photonic crystal material can be deposited. By including a substrate layer, the z symmetry of the photonic crystal is broken, introducing newly accessible leaky modes to the photonic crystal as TE and TM modes couple to each other and are no longer trapped within the photonic crystal plane[9].The light instead escapes the leaky modes of the photonic crystal to couple into the waveguide modes of the underlying substrate[9,11]. In the case of a quartz substrate, this index of refraction is n=1.5. Since light outside the angle of the quartz escape cone remains trapped within the guided TIR modes of the quartz substrate, that light can be effectively converted by photovoltaic material coupled to the PCWG module. Therefore, our design considers emission into the PCWG guided modes as well as the TIR guided modes of the substrate. Light escaping from the impinging plane of the PCWG is considering lost. Additionally, light emitted within the escape cone of the quartz substrate is also considered lost as it is unable to reach the photovoltaic.

When coupling a QD to a PCWG, we also must consider the absorption wavelengths of both the QD and the PCWG material, a-SiC:H. While a-SiC:H becomes lossless beyond 600nm, it has high absorption in the short wavelength range, as is intrinsic with any semiconducting material. By design, and also through the same intrinsic semiconducting property, the CdSe/CdS QDs also absorb in the short wavelength range, up to around 500nm[25]. Figure 4.2

shows the overlapping absorption profiles between the QDs and a rod array of a-SiC:H. This absorption property becomes a limitation when considering the rod array design, as trapping is highest when the luminophore is at a point of maximum symmetry within the PCWG. Previous work has explored directly embedding luminophores in visibly transparent, lower index materials, like TiO2 or ZnS; however, the low index leads to lower trapping efficiencies and lower Purcell enhancement[22]. Furthermore, even though the absorption length is decreased for the lower index materials, there is still some absorption overlap between the material and the QD profile, so less light is absorbed and converted by the QDs, which in turn results in a less-efficient module. Therefore, even with this limitation, a-SiC:H remains the preferable material for this application. The QD placement however must change accordingly.

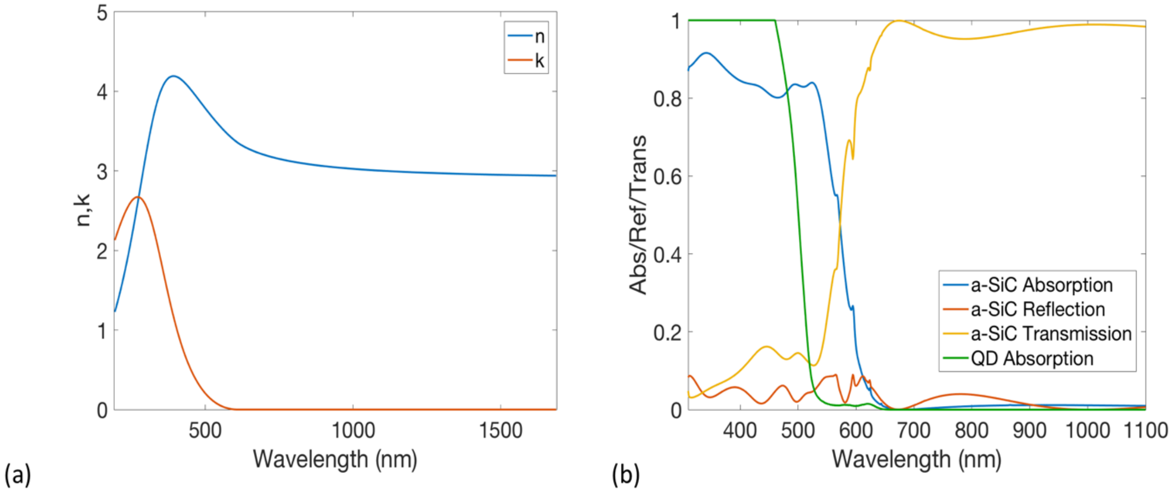

Figure 4.2: In (a), index of refraction and extinction coefficient of a-SiC:H, measured via spectroscopic ellipsometry. In (b), reflection, absorption, and transmission of a hexagonal array PCWG of a-SiC:H pillars at sufficient trapping thickness. QD absorption is also shown to indicate overlap in absorption of the QDs and the photonic crystal material.

We cannot locate the QDs inside of the pillars at the maximum point of symmetry due to the described absorption limitations. In order to ensure as much light as possible reaches to QDs to be successfully down-converted, we opt to locate the QDs at the bottom of the PCWG at the substrate interface. With the QDs at the substrate interface, the rod array will be inverted, with the substrate hence becoming a superstrate. With this inversion, incident light will first travel through the superstrate before reaching the QDs, as opposed to travelling through the a-SiC:H before reaching the QDs. This allows the majority of incident light in the short wavelength range to be absorbed and re-emitted by the QDs instead of travelling through the a-SiC:H and becoming parasitically absorbed. Once the QD re-emits, the emission will be guided in the optical modes of the PCWG, which is lossless across the emission spectrum, or will travel through the TIR modes of the substrate. We therefore opt for this configuration as opposed to placing the QDs at the top of the rods of the PCWG at the air interface in order to guide the modes escaping the PCWG into the TIR of the glass substrate, rather than lose escaped emission to air. While this configuration inevitably has lower trapping efficiency and Purcell enhancement, it ultimately is the best design to achieve an experimentally realizable and optically efficient photovoltaic module. Such a system can potentially be fabricated by first applying a layer of dispersed QDs to the substrate and then depositing the PCWG material[26-28].

The macro-scale design of the hole array is more simplistic. In the hole array configuration the QDs are placed within in holes etched into a film of a-SiC:H. The hole array does not have the same QD placement constraints as the rod array due to the QD placement outside the absorbing medium. The QDs are located throughout the volume of the holes, as opposed to being deposited in an effective single layer of QDs at a specific location, as is required for the rod array. Additionally, a hole array could be advantageous due to its greater effective index of refraction caused by a high fill fraction of high-index material. Similarly, the index of refraction between the rods is 1, to match the index of air between each of the rods. In the hole array, we set the index within the holes to 1.44 to simulate poly(laurel) methacrylate, a common polymer material used as a matrix for suspending CdSe/CdS QDs. The higher index of refraction in the holes further boosts the effective index of the PCWG and can therefore allow higher Purcell enhancement and trapping efficiency. A schematic of both the rod and hole array PCWG, coupled to a photovoltaic, is given in Figure 4.3.

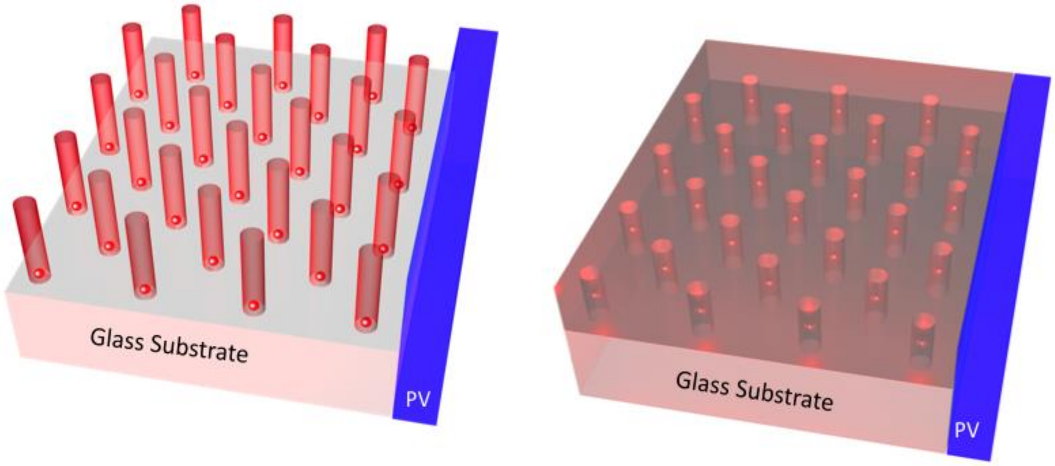

Photonic Crystal Rod Array

Photonic Crystal Hole Array

Figure 4.3: Schematic of the rod array (left) and hole array (right) a-SiC:H PCWGS.

In order to analyze the trapping efficiency and Purcell factor, we employ Lumerical FDTD simulations to calculate the trapping of light emitted from a QD. Given the QD capability to isotropically absorb light over all angles of incidence, this study does not analyze the incident absorbed light, but instead, looks specifically at QD emission within the LSC[25,29,30].We utilize Perfectly Matched Layer (PML) boundary conditions over a periodicity of 8 unit cells to accurately calculate behavior when the field emission has adequate distance to spatially decay while limiting coherent interference with the boundaries in each plane. In order to isolate emitters from coherent electric field phase interference, a supercell is required. Perfectly matched layer (PML) boundary conditions were used on all simulation boundaries in order to isolate the effects of coupling a single emitter to the PCWG optical environment. In order to approximate a QD, we use a dipole source. We simulate the source emission in the x, y, and z orientations then perform an average of the results weighted by the Purcell factor corresponding to each orientation. This averaging modeled the behavior of a single incoherent and nondirectional emitter. More than 20 positions for the rod array and more than 30 positions for the hole array were used to infer an ensemble average for a random dispersion of luminophores. The simulation consists of monitors surrounding the photonic crystal and the underlying substrate in order to record all light in every potential loss channel: the sides, the substrate, and the photonic crystal-to-air boundary. The monitors reported the percentage of emission that is lost to the ambient region above the photonic crystal, trapped in the plane of the photonic crystal, and propagated through the substrate. Monitors were placed in the substrate to record the fields that moved away from the photonic crystal and free space. These fields were then analytically propagated to the far-field to determine the power distribution incident on the flat, opposite surface of the substrate. The light that was trapped in plane and within these TIR angles of the substrate was considered trapped in the overall LSC system. Shape parameters such as the slab thickness, radius and so on, are all examined in normalized units, relative to the periodicity. Both the hexagonal rod and hole array are set with a radii equal to a quarter of the pitch or periodicity of the array. While the ratio of the pitch and radius is the same for both the rod and hole array, the designs deviate with respect to thickness. Since the QDs must be located at the substrate interface of the rod array, the PCWG must be thicker than the hole array in order to maximize the states that the QD emission can couple into. This corresponds to a thickness greater than the pitch by a factor of five. By contrast, the hole array has a thickness greater than the pitch by a factor of three. We find that in order to trap QD emission centered at 635nm, the optimal geometry for the rod array is a radius of 61 nm, a pitch of 242 nm, and a height of 1.21 μm. For the hole array, the optimal parameters are a radius of 58 nm, a pitch of 231 nm, and a height of 694 nm. Given the index of refraction of the PCWG, the index of the substrate, and the given geometric parameters, the band diagrams in Figure 4.4 were generated. For both the rod and hole array, there are many flat TE and TM bands at the QD emissions showing strong coupling the luminescence to the modes of the PCWG. The flat quality of the bands indicates a high LDOS with large, in plane wave vectors which agrees with the large percentages of light detected to travel laterally in the FDTD simulations. Figures 4.5 and 4.6 show the field profiles of the emission trapped in the PCWG generated by the FDTD simulations. All figures show strong emission trapping mechanisms within the PCWG.

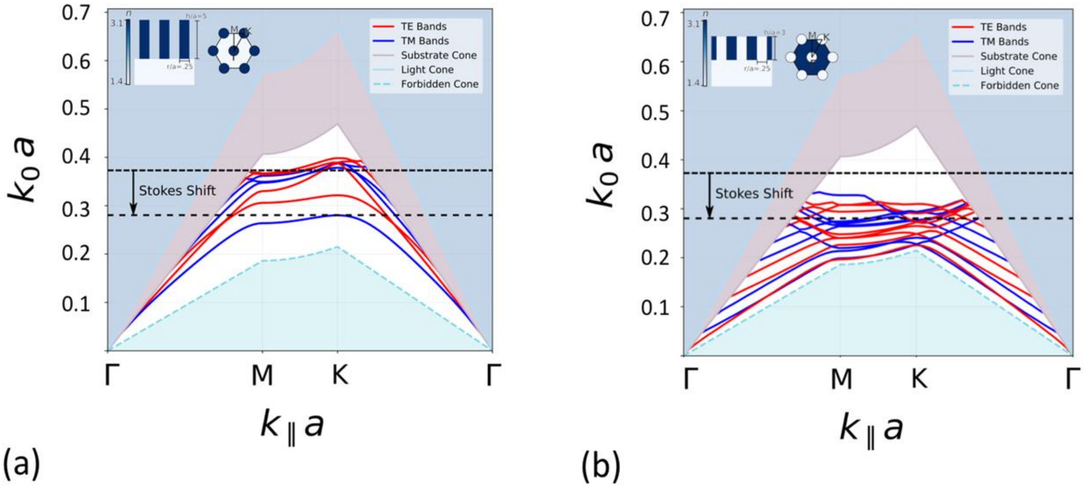

Figure 4.4: Band structures for optimized PCWGS. In (a), the band structure for the hexagonal rod array, (b) the band structure for the hexagonal hole array. The Stokes shifted QD emission couples to the TE and TM modes of the PCWG. The top right insets in both (a) and (b) show the unit cell and structure, color coded by the index of refraction of the PCWG and the surrounding material. Plots created by Colton Bukowsky, using MIT Photonic Band Software with 32k-points along each reciprocal space vector with a resolution and mesh of 24 and 8.

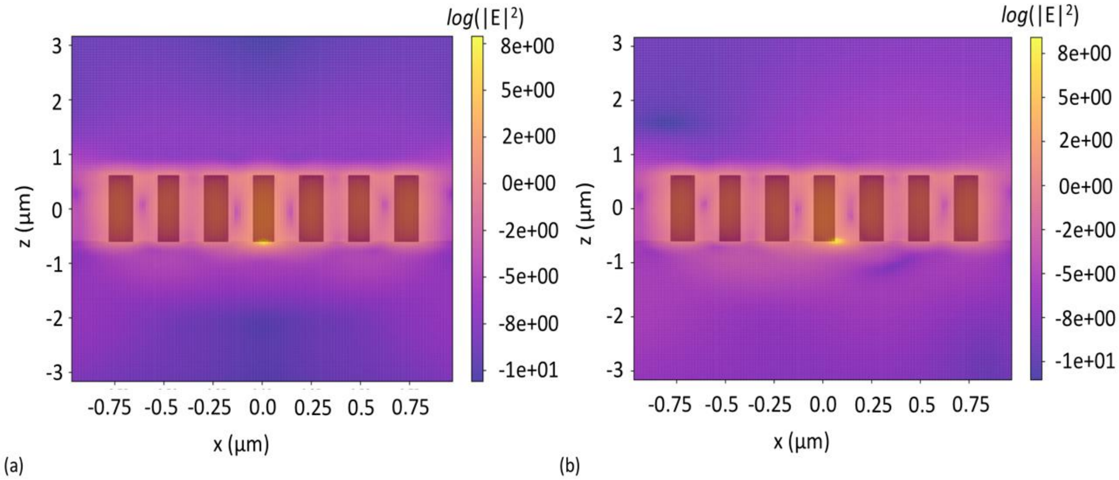

Figure 4.5: Magnitude of the electric field intensity of QD emission in an optimized hexagonal array of a-SiC:H rods with the QDs located at the glass interface. In order to simulate the entire area of the rod/glass interface, the QD was located in the center (a) then translated toward the edge (b) in order to optimize average trapping over the entire substrate interface containing QD emitters.

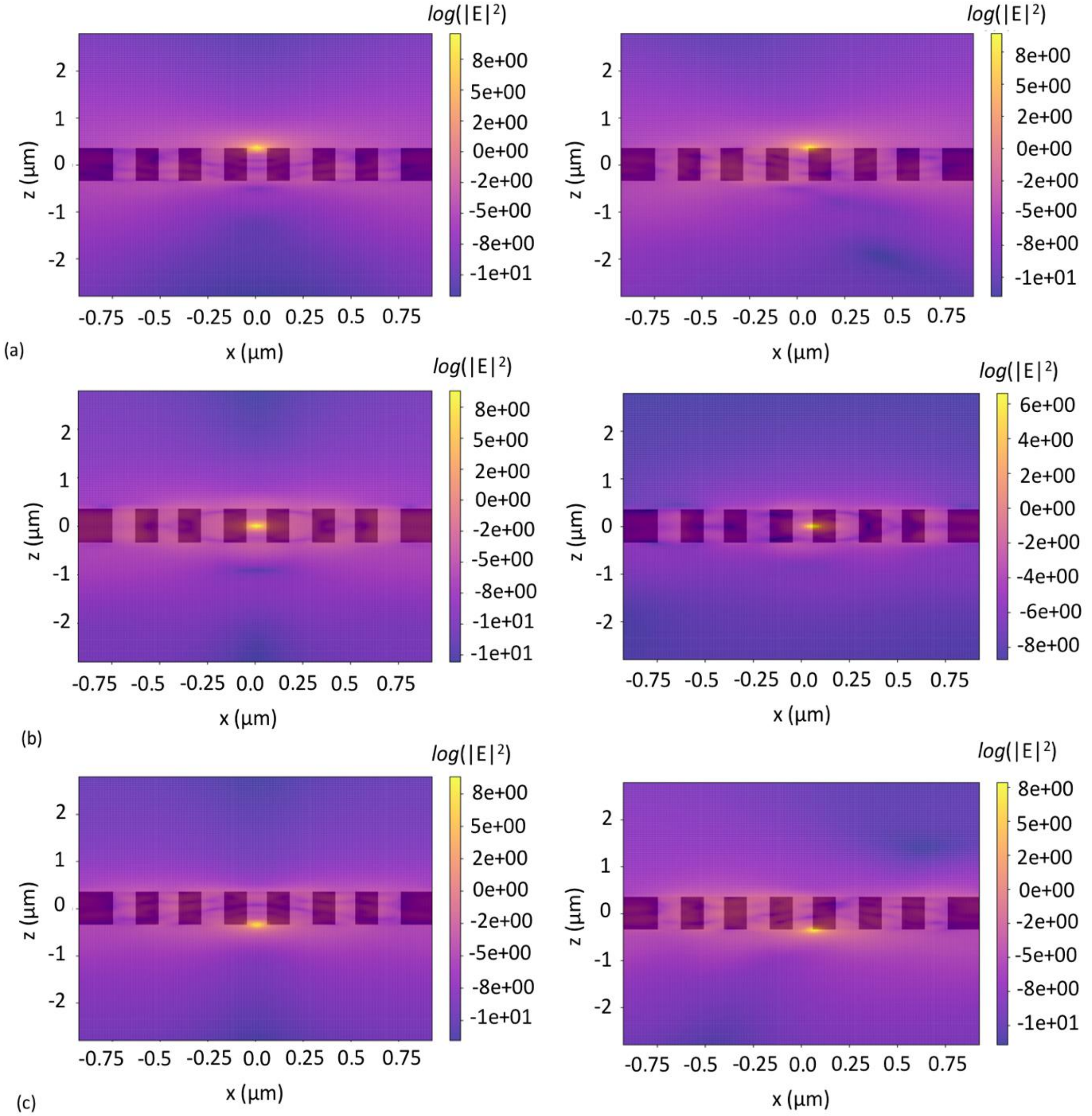

Figure 4.6: Magnitude of the electric field intensity for the optimized a-SiC hexagonal hole array. QD locations are translated to different x, y, and z locations to characterize QD emission trapping in the array. In (a), QD at the air interface; in (b), QD in the center of the hole array; in (c), QD emission located at the substrate interface. The left column shows the electric field intensity with the QD located in the x, y center, and the right columns shows the electric field intensity with the QD located at the edge of the hole radius for each respective z location.

We cannot experimentally precisely locate a QD to a fixed position within a PCWG. In order to generate a robust data set, it is imperative analyze the emission profile of QDs at many coupling locations within the PCWG to best approximate the random distribution that will inevitably occur in the fabrication process. In the case of the rod array, we analyzed the emission of QDs throughout the *x*, *y* plane at the waveguide/substrate interface. We assume that upon fabrication, the QD layer will be spin-coated across the substrate before the PCWG material is deposited. Approximating the random distribution in the rod array at the substrate interface is fairly straightforward. We first simulation the emission of a QD located at the center of the pillar in the *x*-*y* plane at the substrate interface, at maximum symmetry for the configuration. We then locate the QD at the edge of the pillar at the substrate interface. This breaks the maximum symmetry, but still allows most of the emission to be guided into either the optical modes of the PCWG, or the TIR modes of the substrate. The field profile of such emission is shown in Figure 4.5. We then integrate across the area of the disk making up the PCWG to substrate interface to best approximate overall trapping of a random distribution of the QDs at the interface. We find that the average trapping efficiency for the rod array with QDs dispersed across the area of the PCWG to substrate interface is 92.56% with a Purcell factor of 2.2. Figure 4.7 Shows the trapping profile of such a PCWG

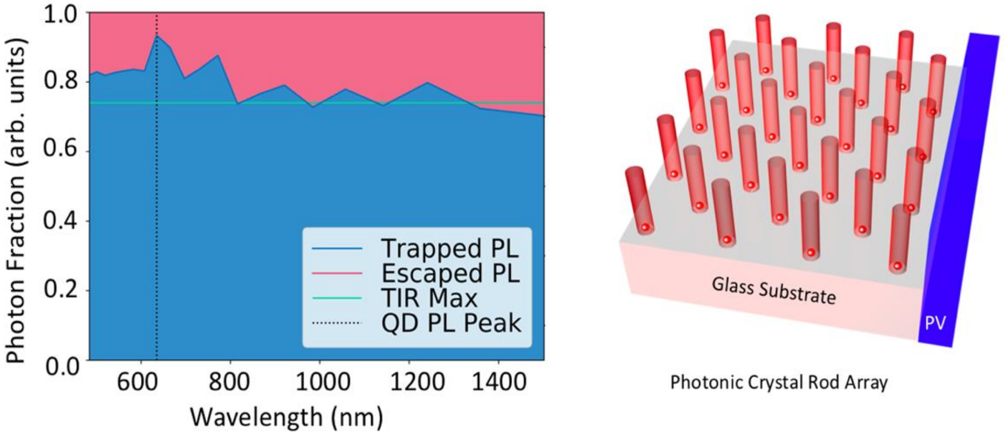

Figure 4.7: The left shows the trapping emission profile of a QD coupled to a PCWG rod array. 92.56% of the emission is trapped. The green line shows the TIR maximum for a polymer waveguide with an index of refraction of 1.44.

In the hole array, we approximate for a random distribution of QDs throughout the *x,y* and *z* plane, performing a sensitivity study over a volume of potential QD locations. Figure 4.6 shows similarity to Figure 4.5 in that the profile is maximally trapped at the point of symmetry in the PCWG, but trapping efficiency maintains fairly robust through the *x* and *y* plane. However, more emission escapes the PCWG and the TIR modes of the substrate when the QD location is moved closer to the air or substrate interface, breaking the symmetry in the PCWG volume. We took the approach of simulating many "disks" of QD distributions throughout the PCWG volume, with the same averaging method used to calculate the trapping efficiency in the rod array. The resulting trapping efficiency of each "disk" is shown in Table 4.1.

Quantum Dot Location	**Trapping Efficiency** (%)	**Purcell Factor**
TIR Only; in waveguide	74.13	1
RA; at Substrate Interface	92.56	2.2
HA; in PCWG center	95.36	3.26
HA; 58 nm above substrate	93.82	3.33
HA; 638 nm above substrate	93.82	3.34
HA; 579 nm above substrate	91.80	3.24
HA; at air interface	82.50	2.64
HA; at substrate interface	84.16	2.62
HA; infill full hole volume	92.30	3.2
HA: infill 58-638 nm	93.32	3.3

Table 4.1: Trapping efficiency and Purcell factor as a function of Q location in hole array (HA) and rod array (RA) photonic crystal waveguides

Moving the QD location towards the substrate or air interface of the PCWG caused the light trapping to fluctuate in proportion to the fraction of light emitted in the escape cone of the substrate. The maximum achieved trapping is that of a QD disk located in the maximum symmetry point of the PCWG where we see a trapping efficiency of 93.56% with a Purcell factor of 3.26. The QD behavior becomes more interested upon moving the disk throughout the volume of the 694 nm *z* plane. When moving the QD 232 nm from the center in the positive or negative direction, the trapping efficiency drops from 95.36% in the center to around 91.5%. However, when moving to even further from the center, the trapping efficiency increases to 93.82% for both heights. When QDs are located closer to the top or bottom of the photonic crystal, at the air or substrate interfaces, light trapping in the photonic crystal plane remains nearly constant, however the fraction of light in TIR modes of the substrate increases. Moreover, when QDs are located at a height of 115 nm above the substrate interface, approximately 85% of the emitted light stays within the photonic crystal. We observe similar behavior when we move the QD downward to 58 nm above the substrate interface. Likewise, for both QD placements, about 11% of the light travels out of the photonic crystal into the substrate. However, when the QD is located at a height 115 nm above the substrate, 44% of that light is lost via the substrate escape cone, whereas only 22% the light in the substrate is lost via the substrate escape cone for the QD placed 58 nm above the substrate. This fluctuation therefore proves advantageous as the TIR modes of the substrate makeup for loss mechanisms caused by the broken symmetry of the QD placement within the PCWG.

This decrease in trapping efficiency is most apparent when the QD is placed at the edge of the PCWG at either the air or substrate interface. Light trapping for QDs at the air interface decreases to 82.5% and the light trapping efficiency decreases to 84.16% for QDs located at the substrate interface. The trapping is slightly higher at the substrate interface due to the coupling into the TIR modes of the substrate, unavailable to the emission at the air interface. When accounting for a random distribution of QDs throughout the entire volume of the hole, the trapping efficiency is 92.3% with a Purcell factor of 2.9. If we assume that the polymer layer near the top and bottom interfaces is devoid of QDs, so that QDs are located only at heights from 58 to 636 nm, the trapping efficiency increases to 93.3%with a Purcell factor of 3.2. If we lower the optical density of the QDs, allowing a lower volumetric QD concentration, we can concentrate the QDs in a thin disk located in the center of the holes with the majority of the volume infilled with polymer. This results in the highest possible trapping efficiency of 95.4% with a Purcell factor of 3.26. Figure 4.8 shows the trapping profile of such a hole array.

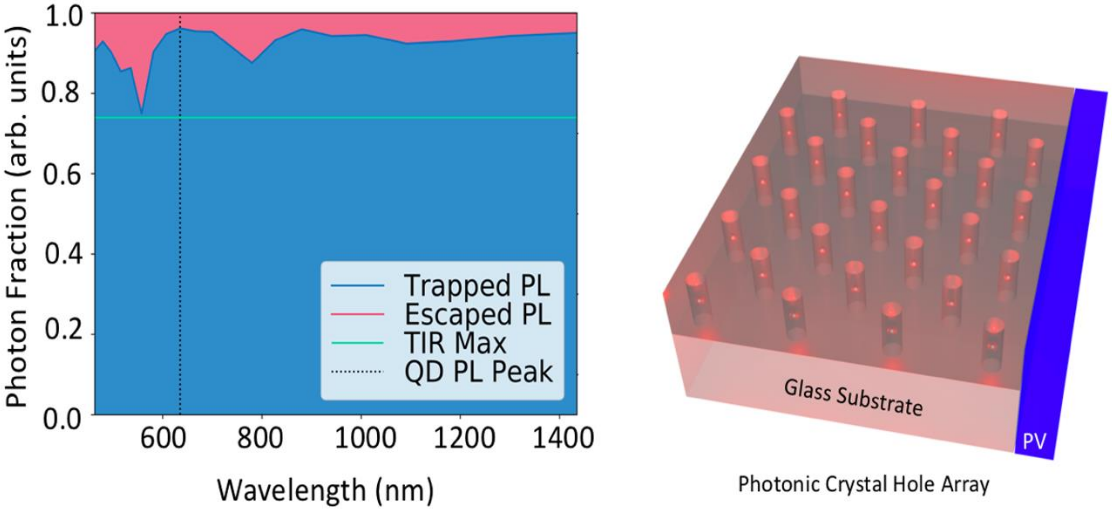

Figure 4.8: The left shows the trapping emission profile of a QD coupled to a PCWG hole array. 95.4% of the emission is trapped with a QD disk in the center of the holes. The green line shows the TIR maximum for a polymer waveguide with an index of refraction of 1.44.

While we do not consider the photonic band gap in our figure of merit for PCWG performance, the difference between the TE and TM band structures shown in Figure 4.4 becomes quite clear in the trapping profile and mechanisms of the rod and hole arrays. The difference in the Purcell factor is notable. In the rod array, the Purcell factor from the *x* and *y* dipole emission are low due to the rod array's preference for a TM photonic bandgap. In the hole array, the *x* and *y* dipole emission profiles show higher Purcell enhancement which boosts the overall Purcell factor achieved when spherically averaging the dipole emissions. Since the rod array favors the *z*-oriented dipole emission, the trapping efficiency could be improved by properly oriented quantum rods whose emission profiles best resemble a *z*-oriented dipole. Furthermore, the rod array demonstrates robust trapping across a wide range of wavelengths, extending throughout the near-infrared to infrared region. This is in part due to its greater effective index caused by both the fill fraction and the increased index of refraction of the QD dispersion media within the holes. To summarize, we have presented a two PCWG designs, a rod array and a hole array, that demonstrate trapping efficiencies above 92% with a Purcell factor of approximately 2 in the rod array and approximately 3 in the hole array.

4.4 Concentration Factor Analysis

In Chapter 2, we discussed the LSC metric of concentration factor. In order to contextualize our PCWG designs with metrics used in the LSC community, we analyze how the trapping efficiencies effect concentration factor of the LSC module. Although concentration factor as a metric has its limitations, it is the most commonly used standard across the LSC community so it makes sense to frame nanophotonic research in these terms. Concentration factor represents the achievable enlargement factor of active PV area for an LSC[31]. LSC designs aim to achieve high concentration factors in order to minimize the required PV active area within the LSC. There are many ways to define concentration factor. For the purposes of this analysis, we will be using Equation 4.6, where η_{abs} is the device absorbance, η_{WG} is the waveguiding efficiency, η_{PL} is the QD PLQY, and η_{trap} is the waveguide trapping efficiency.

$$concentration\,factor\ =\ \eta_{abs}\times\eta_{WG}\times\eta_{PL}\times\eta_{trap}\times GG \tag{4.6}$$

Equation 4.6 sets the concentration factor as a function of geometric gain (GG), or the ratio of the LSC area to the area of the photovoltaic cell. Analysis of the concentration factor as a function of geometric gain allows us to provide a more generic figure of merit, independent to the individual photovoltaic used or the photovoltaic location/orientation in the module. The device absorbance is defined in Equation 4.7 and refers to the fraction of incident light that is absorbed by the luminophores. R is the coefficient of reflection at the air/glass interface (R = 0.04), α_1 is the absorption coefficient of CdS at 450nm, and d is the waveguide thickness.

$$\eta_{\ abs}\ =\ (1-R)(1-e^{-(\alpha_1\times d)}) \tag{4.7}$$

Waveguide efficiency is the fraction of QD emission that reaches the photovoltaic material and is defined by Equation 4.8 where β is the fitting parameter set to 1.4 (typical value in concentration and quality factor analyses), α_2 is the absorption coefficient for CdSe at 635 nm, and L is the length of the waveguide.

$$\eta_{WG} = \frac{1}{(1+\beta\times\alpha_2\times L)} \tag{4.8}$$

While the CdSe/CdS QDs have a PLQY of beyond 99% in solution, when dispersed in a suspending waveguide medium, the PLQY decreases to 95%[25,29,30,32]. Since we ultimately want to analyze a module with as realistic parameters as possible, we opt to set η_{PL} to 95%. The trapping efficiency is the fraction of QD emissions trapped within the TIR modes, and so for the purposes of our analysis, this will be the trapping efficiencies calculated in the previous section. Figure 4.9 shows the results of our concentration factor calculations.

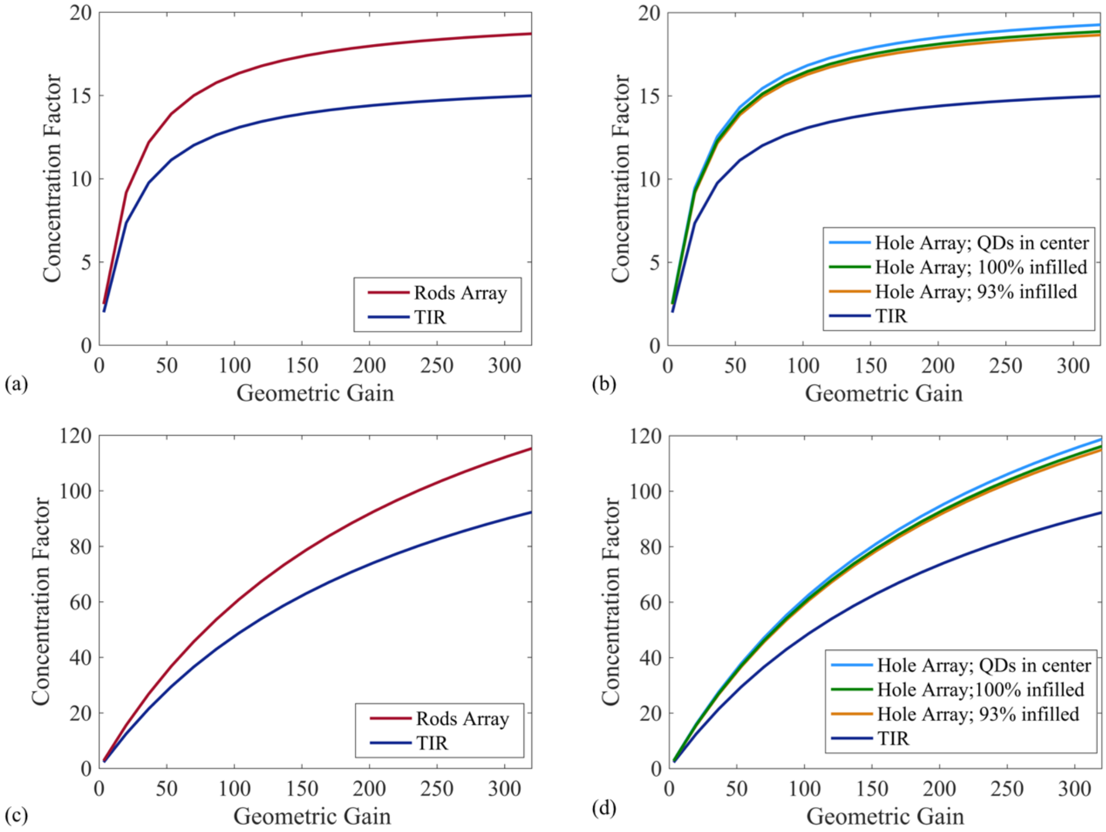

Figure 4.9: Plots by Megan Phelan. Concentration factor vs geometric gain for an edge-lined LSC using CdSe/CdS QDs. We show the concentration factor performance in comparison to TIR for the proposed (a) rod array and (b) hole configurations with varied ways of filling the QDs in the holes, assuming a realized Stokes ratio of 100. Figures (c) and (d) display the concentration factor performance for each the rods and holes, respectively, for an idealized CdSe/CdS quantum dot with a Stokes ratio of 1000.

In Figure 4.9, we demonstrate that concentration factor improves when employing both a rod and hole array PCWG as the waveguiding mechanism in the LSC. We discuss Stokes ratio in Chapter 2, but in the case of our analysis it refers to the ratio of α_1 to α_2. Figure 4.9 (a) and (b) show the achievable concentration factors using the realistic Stokes ratio of 100. Figure 4.9 (c) and (d) show the achievable concentration with idealized CdSe/CdS QDs with a Stokes ratio of 1000. The difference between the rod and hole array concentration factors is clearly an effect of the increased trapping efficiency of the hole array. In the case of the hole arrays, it is promising that the there is little difference between the resulting concentration factor when the hole volume is infilled versus when the hole is only filled with QDs at the optimal point of symmetry, maximizing the trapping emission trapping efficiency. This provides an easier path for fabrication. Since the trapping efficiencies of all of these designs are >92%, each of these configurations has the potential to improve on a traditional QD waveguide by nearly 30%, which is consistent with the results of Rousseau and Wood[7].

4.5 Initial Fabrication Steps

Given the higher performance and potentially simpler QD integration path of the PCWG hole array, we opt to only peruse fabrication of the hole array. To fabricate the rod array, we would have to first deposit the QD layer. With the hole array, the QD layer is added post fabrication making it easier to fine tune fabrication steps without wasting QDs. Furthermore, though concentration factor is comparable, the Purcell enhancement generated in the hole array is stronger, therefore has a greater effect on the QD performance which can result in more efficient LSC modules. The first step in fabricating a PCWG is to of course first fabricate the photonic crystal itself. Since we are still using a-SiC:H as the PCWG material, the PECVD process described in Chapter 3 is the same deposition method used for the PCWG as well[24]. In order to conserve material, the fabrication optimization was begun on samples with a a-SiC:H thickness of 150nm, since that is the standard wafer thickness we received for the spectrally selective HCG. The 700nm disk will be used after successful optimization. While there is potential for the etch recipe to vary when increasing the thickness by a factor of 4.67, the lithography parameters can be finalized on the thinner samples.

In order to write the pattern into the a-SiC:H layer, we again opt for e-beam lithography, given the small feature sizes of the holes (diameter = ~120nm). Since we are etching holes instead of rods, we opt for a positive tone resist, specifically ZEP 520A. ZEP 520A does not suffer from the same adhesion difficulties as MaN-2403, so we are able to spin-coat directly after a quick rinse of the sample in acetone followed by IPA. We spin-coat the ZEP 520A for 1 minute at 3000 rpm for a resist thickness around 250nm. We then cure the resist by placing it on a hot-plate at 180 degrees Celsius for 3 minutes. One note about ZEP 520A is that it can be very difficult to remove even before being cured. If the ZEP 520A coats unevenly, you can remove by spraying or sonicating with acetone and soaking the sample for about 5 minutes. In order to remove the ZEP 520A after the polymer is cured, it is recommended to use an O_2 plasma step such as the one outlined in the resist removal step in Chapter 3. Since the hole array is also fabricated on the insulating quartz, we repeat the charge layer step described in Chapter 3. After depositing the charging layer, we write the pattern with a Raith 5200 electron beam writer with and electron source set at 100kV and a current of 5nA. The dose of the beam is considerably less with ZEP 520A, set at 180μC/cm^2. To etch these samples, we start with the same pseudo-bosch recipe used in Chapter 3 to etch the rod arrays. While we do not expect that the recipe will match perfectly, given that the materials are the same we expect the recipe to be a variation of the same pseudo-bosch building blocks. However, we discover that when etching feature sizes on the order of 120nm, the etch becomes unreliable. At varying pressures, temperatures, and adhesion methods, the resulting photonic crystal exhibits misshapen and unwritten features. This issue does not appear when writing holes with a diameter of 240 nm. Figure 4.10 shows the difference between the fabricated hole arrays with diameters of 120nm and 240nm using comparable pseudo-bosh etching parameters. To accurately etch the smaller features in the optimized hole array, we will likely require a more advanced etch recipe such as a cryo-etch.

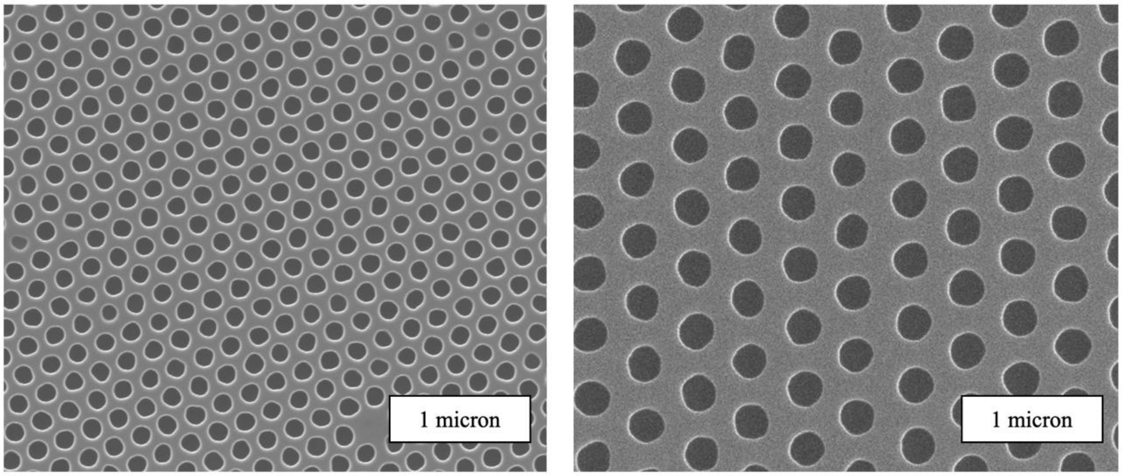

Figure 4.10: The left is a SEM image of a hole array with feature sizes on the order of 120nm, but an uneven and unreliable etch. The right is a SEM image of a hole array with feature sizes larger by a factor of 2, but with a much more even etch.

We therefore opt to fabricate holes at a diameter of 240 nm, using a pseud-bosch gas mixture at a pressure of 8mtorr and temperature of negative 5 degrees Celsius for 120 seconds, for the proof of concept QD integration test. This is also advantageous from an emission trapping perspective as we will not be using the highly efficient CdSe/CdS QDs at this design test phase. We instead opt to use InAs/ZnSe QDs with an emission peak at 950 nm. InAs/ZnSe are less efficient but less expensive QD alternatives to the CdSe/CdS QDs. Given their emission at 950nm, a PCWG with hole diameters of 240 nm will have a higher trapping efficiency than a PCWG with a hole diameter of 120 nm since the geometric parameters of an optimized PCWG scale linearly with the maximum trapping wavelength.

To integrate the QDs at this stage, we aim for a method that is not wasteful of the QDs, and does not require a curing step. Our main goal at this stage is to see if the QDs are integrable with the hole array PCWG. For full device fabrication, it seems likely that the QDs dispersed in polymer will be integrated with the PCWG then cured in order to keep them in place to ultimately be incorporated into a greater LSC module. First, we have to make sure we are able to deposit the QDs within the holes. This is not straightforward as we are working with liquid mediums and PCWG arrays with nano-scale features. We opt to use confocal microscopy as our method to evaluate if the QDs coupled into the hole of the PCWG array.

Via confocal microscopy, we can image the location of where the luminescence occurs. If the luminescence pattern matches the pattern written lithographically (i.e a hexagonal array), then we will know integration was successful. A limitation of confocal microscopy, is the resolution size. The designed hole array has a pitch of approximately 475 nm with holes on the order of 240 nm in diameter. In order for the luminescence from the hole arrays to resolve in the confocal image, we increase the pitch of the holes to 2 μm. At this pitch, the hole array becomes invisible. To overcome this so we can isolate the location, we use previously established 240n m diameter patterns with a pitch of 475nm to create a box around the array with a 2 μm pitch. A schematic of this is shown in Figure 4.11.

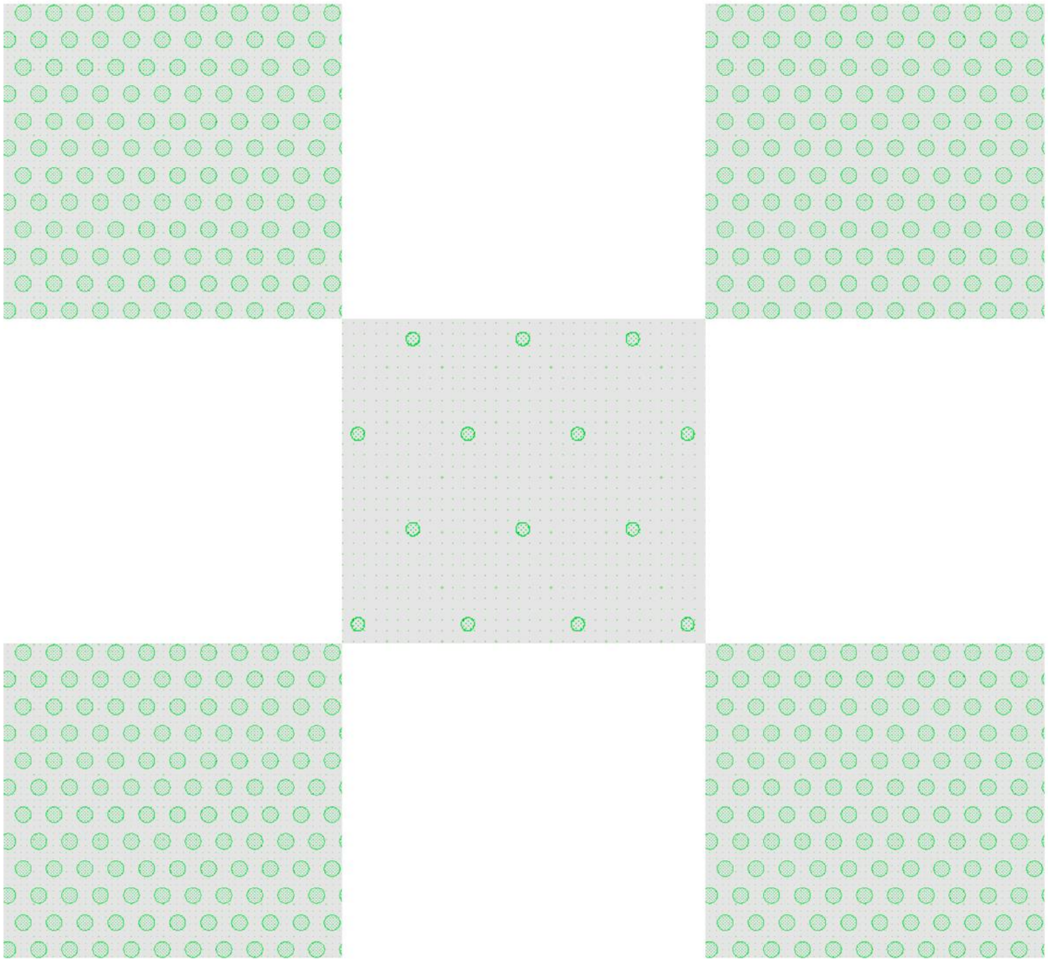

Figure 4.11: A CAD schematic of the array with a 2 μm pitch surrounded by established patterns acting as visible markers for the 2 μm pitch array.

To integrate the QDs, we start with a method presented by Yi Cui *et al* in which capillary forces induced during the evaporation of the QD suspension medium allow nanocrystal integration with lithographically written patterns[33].

4.6 Discussion

We have demonstrated that PCWGs are a single layer alternative to trapping QD emission for LSCs. We analyzed two-dimensional hexagonal hole arrays and rod arrays and found that both architectures can be designed to trap over 90% of QD emission. Furthermore, these designs produce record breaking concentration factors in LSCs.

While both the rod and hole array can produce trapping efficiencies above 90%, we opt to pursue fabrication of the hole array due to a move straightforward QD integration process and trapping efficiency maintained across a wider range of wavelengths. Furthermore, we can achieve the necessary optical density of the QDs more easily in the hole array. Initial fabrication of hexagonal hole arrays has begun and is reliably reproducible. Next steps are to integrate the QDs.

References

1. Yablonovitch, E. “Inhibited Spontaneous Emission in Solid-state Physics and Electronics,” *Physical Review Letters* **1987** 5, 8(20), 2059–2062.

2. Liu, J.; Xu, H.; Yang, Z. *et al.* “A Research of Magnetic Control Ferrite Photonic Crystal Filter,” *Plasmonics* **2017** *12*, 971–976.

3. Dudley, J., Taylor, J. “Ten Years of Nonlinear Optics in Photonic Crystal Fibre”. *Nature Photonics* **2009** *3,* 85–90.

4. Akahane, Y., Asano, T., Song, B. et al. “High-Q Photonic Nanocavity in a Two-Dimensional Photonic Crystal.” *Nature* **2003** *425*, 944–947.

5. Andalib P. and Granpayeh,N. "All-optical Ultracompact Photonic Crystal AND Gate Based on Nonlinear Ring Resonators," *Journal of the Optical Society of America B* **2009** *26,* 10-16.

6. Kurosaka, Y., Iwahashi, S., Liang, Y. et al. “On-chip Beam-steering Photonic-crystal Lasers,” *Nature Photonics* **2010** *4,* 447–450.

7. Rousseau, I. and Wood, V. "Nanophotonic Luminescent Solar Concentrators," *Applied Physics Letters* **2013** *103*, 131113.

8. Peters, M.; Goldschmidt, J. C.; Lö per, P.; Blasi, B.; Gombert, A.¨ The Effect of Photonic Structures on the Light Guiding Efficiency of Fluorescent Concentrators," *Journal of Applied Physics* **2009**, *105*, 014909.

9. Joannopoulos, J. D.; Johnson, S. G.; Winn, J. N.; Meade, R. D." Photonic Crystals: Molding the Flow of Light," 2nd ed.; Princeton University Press: Princeton, **2008.**

10. McDowall, S.; Butler, T.; Bain, E.; Scharnhorst, K. and Patrick, D. "Comprehensive Analysis of Escape-cone Losses from Luminescent Waveguides," *Applied Optics* **2013** *52*, 1230-1239.

11. Ding, Y.; Magnusson, R. "Band Gaps and Leaky-Wave Effects in Resonant Photonic-Crystal Waveguides," *Optics Express* **2007**, *15*, 680− 694.

12. Johnson, S. G. and Joannopoulos, J. D. "Block-iterative Frequency-domain Methods for Maxwell's Equations in a Planewave Basis," *Optics Express* **2001** *8*, no. 3, 173-190.

13. Johnson, S. G.; Fan, S.; Villeneuve, P.; Joannopoulos, J. D. and Kolodziejski, L. "Guided Modes in Photonic Crystal Slabs," *Physical Review B* **1999** *60*, no. 8 5751–58.

14. Purcell, E. "Spontaneous Emission Probabilities at Radio Frequencies," *Physics Rev*iews **1946**, *69 (11-12)*, 674.

15. Novotny, L.; Hecht, B. "Principles of Nano-Optics", Cambridge, U.K., **2006**.

16. Kuttge, M.; Garcia de Abajo, F.; Polman, A. "Ultrasmall Mode Volume Plasmonic Nanodisk Resonators," *Nano Letters* **2009** *10* (5) 1537-1541.

17. Jiao, X.; Blair, S. "Optical Antenna Design for Fluorescence Enhancement in the Ultraviolet," *Optics Express* **2012** *20* 29909-29922.

18. Kristensen, P. T.; Hughes, S. "Modes and Mode Volumes of Leaky Optical Cavities and Plasmonic Nanoresonators," *ACS Photonics* **2014** *1* (1) 2-10.

19. Englund, D.; Fattal, D.; Waks, E.; Solomon, G.; Zhang, B.; Nakaoka, T.; Arakawa, Y.; Yamamoto, Y.; Vuckovic, J. "Controlling the Spontaneous Emission Rate of Single Quantum Dots in a Two-Dimensional Photonic Crystal," *Physics Review Letters* **2005,** *95,* 013904.

20. Lodahl, P., Floris van Driel, A., Nikolaev, I. et al. “Controlling the Dynamics of Spontaneous Emission from Quantum Dots by Photonic Crystals” *Nature* **2004** *430*, 654–657.

21. Einstein, A. “Strahlungs-Emission und -Absorption nach der Quantentheorie,” *Verhandlungen der Deutschen Physikalischen Gesellschaft* **1916** *18* (13/14). 318–323.

22. Bukowsky, C. R., “Scalable Nanophotonic Light Management Design for Solar Cells,” Thesis, California Institute of Technology, **2019.**

23. Meinardi, F., Bruni, F. & Brovelli, S. “Luminescent Solar Concentrators for Building-integrated Photovoltaics”. *Nature Review Materials* **2017** *2***,** 17072.

24. Boccard, M.; Holman, Z. C. “Amorphous Silicon Carbide Passivating Layers for Crystalline-silicon-based Heterojunction Solar Cells,” *Journal of Applied Physics*. **2015**, 118 (6), No. 065704.

25. Hanifi, D. A.; Bronstein, N. D.; Koscher, B. A.; Nett, Z.; Swabeck, J. K.; Takano, K.; Schwartzberg, A. M.; Maserati, L.; Vandewal, K.; van de Burgt, Y.; Salleo, A.; Alivisatos, A. P. “Redefining Near-Unity Luminescence in Quantum Dots with Photothermal Threshold Quantum Yield,” *Science* **2019**, *363*, 1199−1202.

26. Bae, W. K.; Park, Y. S.; Lim, J.; Lee, D.; Padilha, L. A.; McDaniel, H.; Robel, I.; Lee, C.; Pietryga, J. M.; Klimov, V. I. “Controlling the Influence of Auger Recombination on the Performance of Quantum-Dot Light-Emitting Diodes,” *Nature Commuications.* **2013**, *4*, 2661.

27. Likovich, E.M., Jaramillo, R., Russell, K.J., Ramanathan, S. and Narayanamurti, V., “High-Current-Density Monolayer CdSe/ZnS Quantum Dot Light-Emitting Devices with Oxide Electrodes,” *Advanced Materials*, **2011** *23*: 4521-4525.

28. Caruge, J., Halpert, J., Wood, V. *et al.* “Colloidal Quantum-dot Light-emitting Diodes with Metal-oxide Charge Transport Layers,” *Nature Photonics* **2008** *2***,** 247–250.

29. Needell D.R. *et al* “Design Criteria for Micro-Optical Tandem Luminescent Solar Concentrators,” *IEEE Journal of Photovoltaics*, **2018** *8* 1560-1567.

30. Bronstein, N. D.; Yao, Y.; Xu, L.; O’Brien, E.; Powers, A. S.; Ferry, V. E.; Alivisatos, A. P.; and Nuzzo, R. G. “Quantum Dot Luminescent Concentrator Cavity Exhibiting 30-fold Concentration,” *ACS Photonics*, **2015**, *2, 11*, 1576-1583.

31. Klimov, V.I.; Baker, T. A.; Lim, J.; Velizhanin, K.A. and McDaniel, H. “Quality Factor of Luminescent Solar Concentrators and Practical Concentration Limits Attainable with Semiconductor Quantum Dots,” *ACS Photonics* **2016** *3* (6), 1138-1148.

32. Meinardi, F., Colombo, A., Velizhanin, K. *et al.* “Large-area Luminescent Solar Concentrators Based on ‘Stokes-shift-engineered’ Nanocrystals in a Mass-polymerized PMMA Matrix,” *Nature Photonics* **2014** *8* 392–399.

33. Cui, Y., Bjork, M.T., Liddle, A., Sonnichsen, C., Boussert, B., Alivisatos, A.P “Integration of Colloidal Nanocrystals into Lithographically Patterned Devices,” *Nano Letters* **2004**, 4, 6, 1093-1098.

Chapter 5

LUMINESCENT SOLAR CONCENTRATORS FOR SPACE SOLAR APPLICATIONS

5.1 Introduction to Space Based Solar Energy

While terrestrial photovoltaics can achieve high efficiencies at low costs, they are still only able to collect and convert incident sunlight during the day time. This limits the utility of photovoltaics modules in areas that are cloudy or that experience only a small window each day during which the sun is out. While LSCs can be employed in areas with more diffuse conditions, they are still ultimately limited by output power under non-ideal terrestrial solar conditions. Space based solar energy offers an alternative that bypasses many of the atmospheric limitations of photovoltaic technologies. Space-based solar power (SSP) is a broad term to refer to technology that aims to collect solar power from space and transfer the collected energy for use on Earth. By operating in space, SSP collects incident solar energy continuously as there is no atmospheric or geologic limitations from the Earth's rotation. In short, by deploying photovoltaic technologies in space, we can access an uninterrupted power source[1]. At Caltech, the Space Solar Power Project (SSPP) aims to collect solar energy using PV modules supported by ultra-light structures to reduce weight and cost. The collected power will then be converted to radio-frequency that is wirelessly transferred back to receivers on Earth via a steerable beam.

As members of the PV branch of SSPP, we must design a photovoltaic module that is efficient and lightweight. For terrestrial applications on a grid scale, the common figure of merit for solar power in addition to the power conversion efficiency is the levelized cost of energy, which can be generalized to the lifetime cost of a photovoltaic module divided by its energy output. Units for the levelized cost of energy are generally given in \$/kWh or \$/MWh depending on the operating timeframe used in the calculation. While the levelized cost of energy is an important calculation when deploying PV modules to orbit, the main figure of merit for SSP is the specific power. Specific power is defined as the power per weight of the photovoltaic module. A SSP module is only viable if its specific power is above 1kW/kg[1,2]. Therefore a module's efficiency and cost are severely undercut if the module is heavier. Lastly, the materials sent to orbit must be radiation tolerant as photovoltaics modules are exposed to significantly more solar radiation in orbit than they do on earth where the solar intensity is mitigated by atmospheric filters (gases, water vapor, clouds, etc.) and the Earth's rotation. Therefore, in SSP a PV module must be efficient, lightweight, and comprised of space-grade radiation tolerant materials. Current SSP modules that surpass the 1kW/kg threshold include InP thin films and GaInP/GaAs/GaInAs tandem modules[3,4]. It is herein our goal to design the first LSC for SSP applications with a viable specific power.

5.2 The Case for LSCs in Space Solar Power

We present LSCs as a photovoltaic module for SSP applications. To our knowledge, there has been no prior work on LSCs for SSP. LSCs are a promised, though unexplored technology for SSP applications due to their versatility in material adaptation. LSCs can work with a variety of PV materials and luminophores[5-7]. Furthermore, at single-junction LSCs can be extremely lightweight due to the small area percentage of the PV material. In early 2023, the SSP team at Caltech will be launching the first LSC to be tested for SSP applications. The LSC will operate in low-Earth orbit. For this first iteration, we will be launching LSCs coupled to two different photovoltaic materials: GaAs and Si. The QDs will be $CuInS_2/ZnS$ instead of the previously discussed CdSe/CdS QDS due to their NIR emission. While PLMA is not a space standard polymer like CP1, we opt to disperse the QDs in a PLMA waveguide due to its known compatibility with the QDs[8-12]. Furthermore, initial radiation tests showed that PLMA is durable to the exposure the module will have in orbit. In order to further minimize damage, the waveguide is placed between two quartz slides. For this first iteration, rather than opt for a co-planar cell array as demonstrated in Chapter 2, we edge line the waveguide with the respective PV material. This more traditional LSC set up is also easier to fabricate for an initial test. Additionally, by avoiding the co-planar interconnects, we minimize components that could potentially contribute to damage or loss. The edge-lined photovoltaics are applied with epoxy and silver paint to prevent emission loss from the corners of the waveguide. In order to minimize escape cone losses, the LSC is surrounded by two reflectors: a silver reflector on the bottom of the LSC and a short pass reflector on the top of the LSC. The LSC is then connected to a circuit integrated to the payload software. This initial prototype include six LSC modules. Three modules are attached to Si PV cells and three are attached to GaAs PV cells. The aim of this first launch will be to analyze the efficiency and durability of the LSC. If successful, we will then begin optimization of the specific power through ultra-light LSCs.

5.3 Photonic Crystal Waveguides for Space Solar Power

For future launches, we aim to create an even thinner and lighter LSC module. In order to achieve this it is important to remove components from the LSC that add to the weight, thickness, and cost. By transitioning to PCWG LSCs, we can create a single-layer LSC, further reducing the weight from additional mirrors and thicker waveguides operating in the ray-optical realm.

To start, we again opt to design a hole array as opposed to a rod array. We do this for both ease in QD integration and overall fabrication ease, as highlighted by the initial PCWG fabrication in Chapter 4. At this iteration, we opt to use a-SiC:H as we have for previous PCWG designs. While this material has yet to undergo radiation testing via electron, proton, or ultraviolet exposure, it remains the best material for trapping emission while maintaining a high index of refraction. The photovoltaics used in SSP generally have band edges in the NIR as opposed to the visible spectrum band edge of the InGaP cells from the previous chapters. Not only does this alter the overall design of the PCWG, but also opens the possibility for other PCWG materials if the a-SiC:H is not radiation tolerant in future tests. However, given the current durability of a-SiC:H, it remains a promising first step[9,13].

We currently remain agnostic to the specific QDs as QDs have not generally undergone much radiation testing. Furthermore, QD dispersion methods have yet to be explored in space-approved polymers like high-index CP1. Given that we want to design an optimal PCWG, we are going to assume QDs dispersed in CP1. We aassume the PV material is InGaAs microcells with a band edge at 1100nm. While not affecting our initial analysis, it is important to note that we plan to orient the InGaAs microcells co-planarly. This method will allow for higher efficiencies as the geometric gain can be increased causing less escaped light or light loss via radiative recombination. Lastly, in order to further reduce the weight and thickness of the module we consider a different substrate. Rather than assume the PCWG will be patterned on quartz, we assume a polymer substrate. CP1 films can be fabricated as thin as 2 microns. Furthermore CP1 has an index of refraction of n = 1.6 which is slightly higher than the index of refraction of quartz, n = 1.55[14]. Figure 5.1 Shows a schematic of such a PCWG design with co-planar microcells.

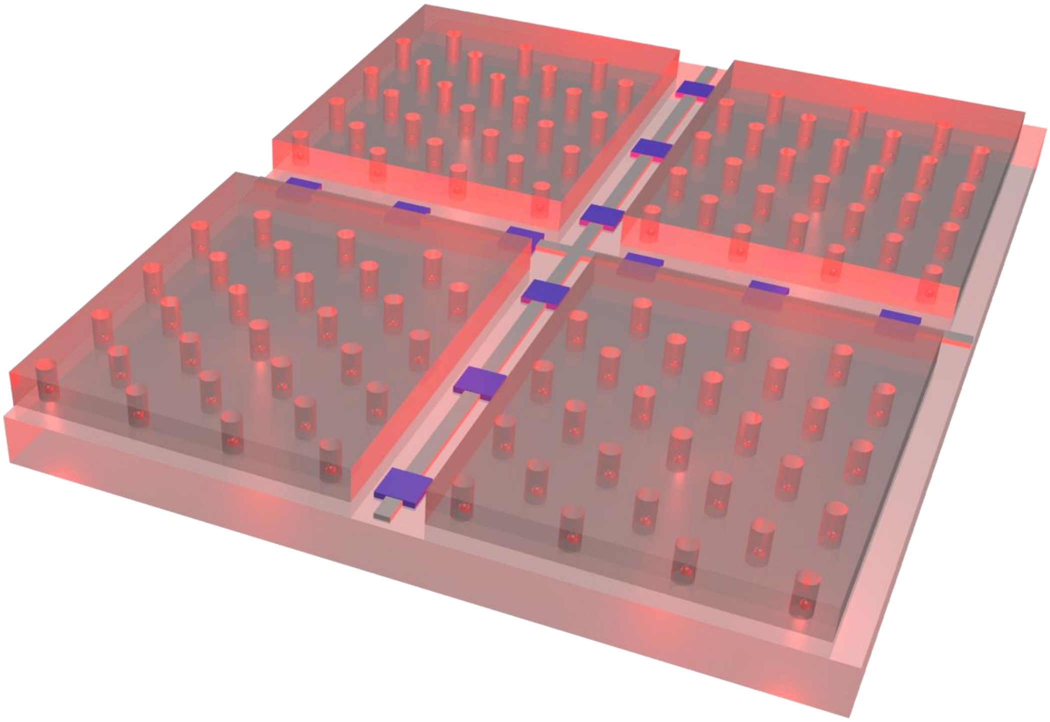

Figure 5.1: Schematic of an ultra-light photonic crystal waveguide for space based solar power. The InGaAs are co-planar with the a-SiC:H hole array which is deposited onto a CP1 substrate.

As in Chapter 4, we analyze trapping potential of such a PCWG via a python script connected to Lumerical that accounts for emission travelling through each region of the PCWG and surrounding material. The only change is that we set the substrate and the hole index to n = 1.6 to best approximate the trapping of CP1, and the wavelength of maximum trapping is set to 1100nm to best approximate high external quantum efficiency region of InGaAs microcells[14-16]. We find fairly consistent results with the previous hoe arrays where we are able to trap 92.6% of QD emission withing the PCWG. This result is shown in Figure 5.2. Given the longer trapping wavelength, the geometric feature sizes scale accordingly. The optimized radius, pitch, and thickness are 100 nm, 401nm, and 1203 nm, respectively. The generated Purcell factor remains 2.9 which is advantageous considering many QDs with NIR emission profiles suffer from lower PLQYs causing further decreases in overall module efficiency.

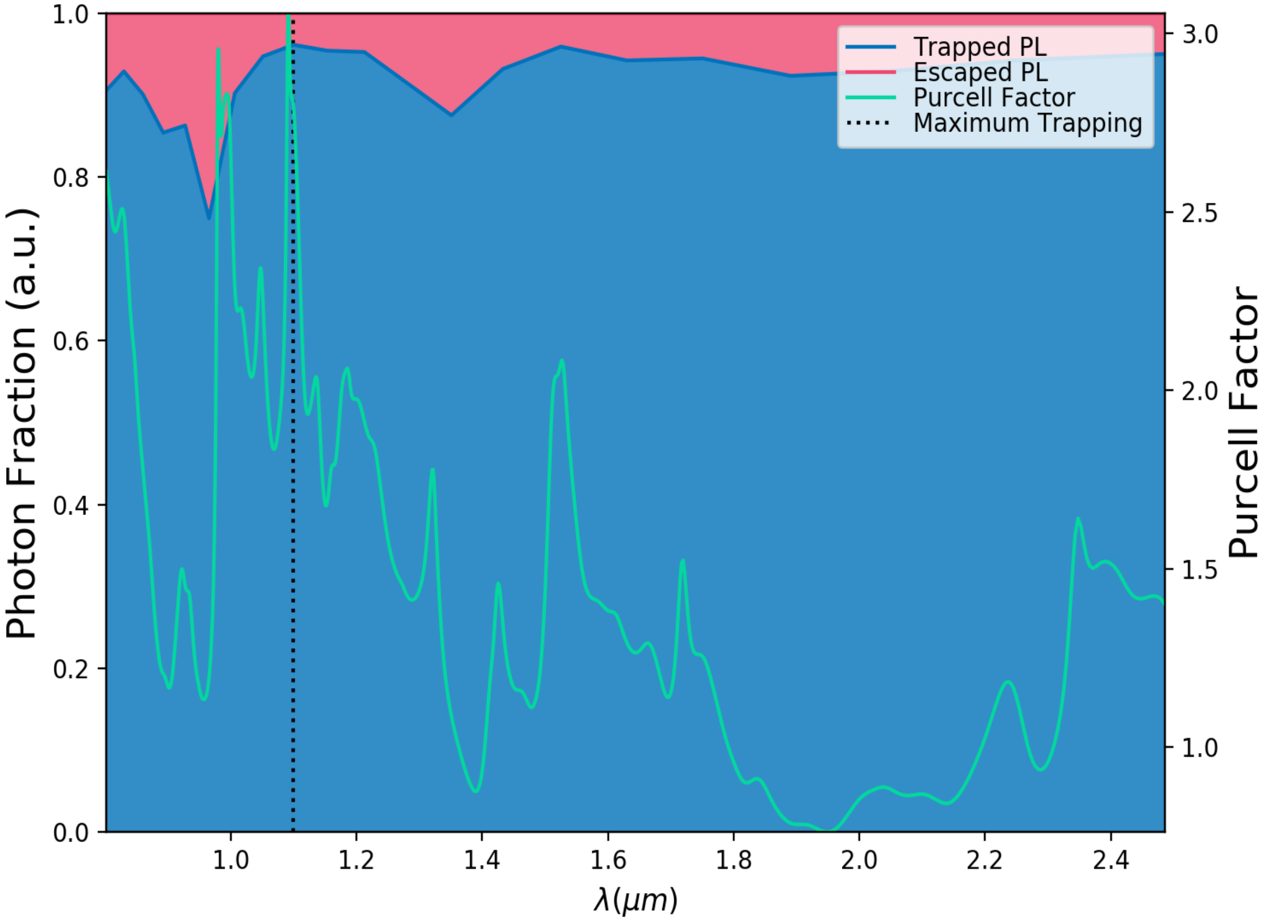

Figure 5.2: Trapping profile of a photonic crystal hole array optimized for maximum trapping at the band edge of InGaAs.

As discussed previously, the figure of merit for SSP modules goes beyond simply efficiency. We must also consider weight, thickness, and in turn, specific power. To analyze weight, we make the following assumptions. We assume the optical density of the QDs is 3.0 and the micro-cells are assembled with a geometric gain of 20 which translates to 5% of the overall

PCWG area. We assume a CP1 substrate thickness of 2 microns. While this is a lower limit on substrate thickness, such films have been fabricated so are still possible as substrates, though more analysis should be performed on durability, radiation, and assembly. Table 5.1 shows each parameter considered in thickness and weight calculation. Calculations include not only the materials making up the PCWG, but also the PV materials an necessary interconnects necessary for the PV architecture. Given each component, we find the total thickness to be 4 microns and the total weight of the PCWG to be 11.503 g/m^2.

	Dimensions	Weight (g/m^2)
InGaAs Cells	2 µm thickness, GG = 20	5.1
Interconnects (Cr/Al)	200 nm	0.0013
Bus Bars (Cr/Al)	200 nm	0.00176
a-SiC:H Hole Array	1.2 µm thickness, 60% fill fraction with 40% CP1 infill	3.3
CP1 Substrate	2 µm thickness	3.1
Total	4 µm	11.503

Table 5.1: Thickness and weight analysis of an ultra-tine PCWG LSC for SPP

Table 5.1 shows that, regardless of efficiency, the PCWG LSC can be designed as an ultra-thin, lightweight alternative to the thicker and heavier single-junction LSC tested on the first launch in 2023. To analyze specific power, we will take a more theoretical approach as there are still many unknowns for LSC SSP performance. We aim to provide a maximum theoretical limit to the specific power figure of merit. We assume the theoretical maximum PLQY of 1. Using a Monte Carlo ray trac model that accounts for the trapping efficiency of the PCWG. We find a maximum theoretical efficiency of 9.8%. This translates to a power output of 13.23 mW/cm^2 using Equation 5.1 and solar input in orbit which is 135 mA/cm^2.

$$Output\ Power = Efficiency * Input\ Power$$

Taking the calculated power and weight, we can solve for specific power. We find a theoretical maximum specific power of 11.5 kW/kg. This makes such a PCWG a promising technology for space solar applications. Such a high specific power ceiling also gives flexibility in the inevitable imperfections in the actual assemble of a PCWG as the calculated specific power far exceeds the viability threshold of 1 kW/kg.

5.4 Discussion

By deploying space-based solar modules, we can gain undisturbed access to continuous solar energy. This area of research is still relatively unexplored from an experimental standpoint due to the prohibitively high launch costs. The Caltech SSP team will be conducting a launch of various SPP technologies in early 2023. This mission will carry the first known LSC sent to orbit.

Looking ahead, we set forth the goal of designing an ultra-thin LSC that could potentially achieve record breaking specific powers. We demonstrate that by replacing a thick waveguide and spectrally selective filters with a PCWG, we can design a module with a specific power of 11.5 kW/kg. Next steps in this work of course include analyzing the results of the first launch and further optimizing PCWG fabrication begun in Chapter 4. Then we should begin testing the stability of each component in the full PCWG LSC design for space readiness.

References

1. P. E. Glaser, "Power from the Sun: Its Future," *Science* **1968** 162, 3856, 857–861.
2. P. E. Glaser, O. E. Maynard, J. Mackovciak, and E. L. Ralph, "Feasibility Study of a Satellite Solar Power Station," *Technology Report February 1974*, **1974.**

3. K.-T. Shiu, J. Zimmerman, H. Wang, and S. R. Forrest, “Ultrathin Film, High Specific Power InP Solar Cells on Flexible Plastic Substrates,” *Applied Physics Letters*, **2009 ,** 95, 223503.

4. D. Cardwell, A. Kirk, C. Stender, A. Wibowo, F. Tuminello, M. Drees, R. Chan, M. Osowski, and N. Pan, “Very High Specific Power ELO Solar Cells (<3 kw/kg) for UAV, Space, and Portable Power Applications,” *2017 IEEE 44th Photovoltaic Specialist Conference (PVSC),***2017,** 3511–3513.

5. Needell, D.R., Bukowsky, C.R., Darbe, S., Bauser, H., Ilic, O., Atwater, H.A. “Spectrally Matched Quantum Dot Photoluminescence in GaAs-Si Tandem Luminescent Solar concentrators,” *IEEE Journal of Photovoltaics”* **2019** 9, 2, 397-401.

6. Bett, A.W., Dimroght, R., Lockenhoff, R., Olivia, E., Schubert, J. “III-V Solar Cells Under Monochromatic Illumination,” *2008 33rd IEEE Photovoltacis Specialists Conference* **2008** 1-5.

7. M. G. Debije and P. P. C. Verbunt, “Thirty Years of Luminescent Solar Concentrator Research: Solar Energy for the Built Environment,” *Advanced Energy Materials*, **2012** 2, 1, 12–35.

8. Fay, C. C., Stoakly, D.M., Clair, A.K. “Molecularly Oriented Films for Space Applications,” *High Performance Polymers* **1999.**

9. Wyrsch, N. *et al* “Ultra-Light Amorphous Silicon Cell for Space Applications,” *2006 IEE 4th World Conference of Photooltaiv Energy Conference* **2006** 1785-1788.

10. Finckenor, M.M., Rodmen, L., Farmer, B. “Analysis of Fluorinated Polymides Flown on the Materials International Space Station Experiment,” *NASA/TM* **2015.**

11. Needell D.R. *et al* “Design Criteria for Micro-Optical Tandem Luminescent Solar Concentrators,” *IEEE Journal of Photovoltaics*, **2018** *8* 1560-1567.

12. Bronstein, N. D.; Yao, Y.; Xu, L.; O’Brien, E.; Powers, A. S.; Ferry, V. E.; Alivisatos, A. P.; and Nuzzo, R. G. “Quantum Dot Luminescent Concentrator Cavity Exhibiting 30-fold Concentration,” *ACS Photonics*, **2015**, *2, 11*, 1576-1583.

13. Zhang, Y., Ishimaru, M., Varge, T., Oda, T., Hardiman, C., Xue, H., Katoh, Y., Channon, S., Weber, W.J. “Nanoscale Engineering of Radiation Tolerant Silicon Carbide,” *Royal Society of Chemistry Journal of Physical Chemistry and Chemical Physics* **2012**, 14, 13429-13436.

14. Naqavi, A., *et al* “Extremely Broadband Ultralight Thermally-Emissive Optical Coatings,” *Optics Express* **2018**, 26, 14, 18545-18562.

15. Lumb, M.P. *et al* “Development of InGaAs Solar Cells for >44% Efficient Transfer-Printed Multi-Junctions,” *2014 IEEE 40th Photovoltaic Specialist Conference (PVSC)* **2014** 0491-0494.

16. Schmeider, K.J. *et al* “Micro-Transfer Printer-Assembled Five Junction CPV Microcell Development,” *2019 IEEE 46th Photovoltaic Specialists Conference (PVSC)* **2019** 0277-0280.

Chapter 6

PHOTONIC CRYSTAL THERMAL CONCENTRATORS

6.1 Introduction to Solar-Thermochemical Energy Conversion

Beyond photovoltaics, we must create net-zero carbon emission fuel production in order to further decrease fossil fuel dependence. This necessitates the design of net-zero carbon synthesis routes for renewable generation of chemical fuels[1-3]. Solar-driven processes under mild conditions present a sustainable alternative to conventional fossil fuels for energy production[2]. By using incident sunlight to generate the conditions necessary for chemical fuel productions, we can replace large-scale industrial production processes that typically operate under high temperatures and elevated pressures[2,4,5]. Common reactions to produce chemical fuels include Sabatier and Haber-Bosch reactions, which operate at temperatures above 573 K and at pressures elevated to 30 atm[6-8]. However, there are also many lower temperature reactions that can generate useful fuels and products as well. For example, a water-gas shift reaction can produce hydrogen at temperatures as low as 315 K[3,9-12]. Furthermore, processes producing plastics, oil additives, or gasoline like ethylene oligomerization can occur at mild temperatures as low as 325 K[13,14].One common method to increase heat using direct sunlight radiation is through the use of geometric concentrating systems, such as the apparatus at the Ivanpah Solar Electric Generating System in Nipton, CA[15]. However, this technology is limited due to its large footprint, need for high direct solar irradiance limiting its location, and geometric limitations which results in a need for active solar trackers [15,16]. We therefore propose the concept of a large scalable planar photonic crystal waveguide as a thermal concentrator to activate temperatures which enable the production of common chemical fuels.

Chapters 4 and 5 have discussed the methods by which we are able to trap emission in the visible spectrum and the NIR range via PCWGs. By simply scaling PCWGS, we can engineering structures that trap at any wavelength. It stands then that we should be able to trap emission in the form of heat as well by scaling the geometric parameters accordingly. Photonic crystals have been proposed for thermal and carbon reduction applications before as both thermal mirrors, and as a method to slow photon travel for solar fuel reactions[17,18]. Furthermore, historically photonic crystals have been studied for their potential to manipulate energy in long wavelengths including out to the microwave wavelength range[19,20]. Therefore, they prove to be potentially scalable to trap and guide emission in the atmospheric window of heat between 8-15 um[21]. Though there are many architectures of PCWG, for this study we will focus on the two-dimensional photonic crystal, shown in Figure 6.1, due to its previously shown trapping efficiency and potential ease and scalability of the fabrication process[22,23].

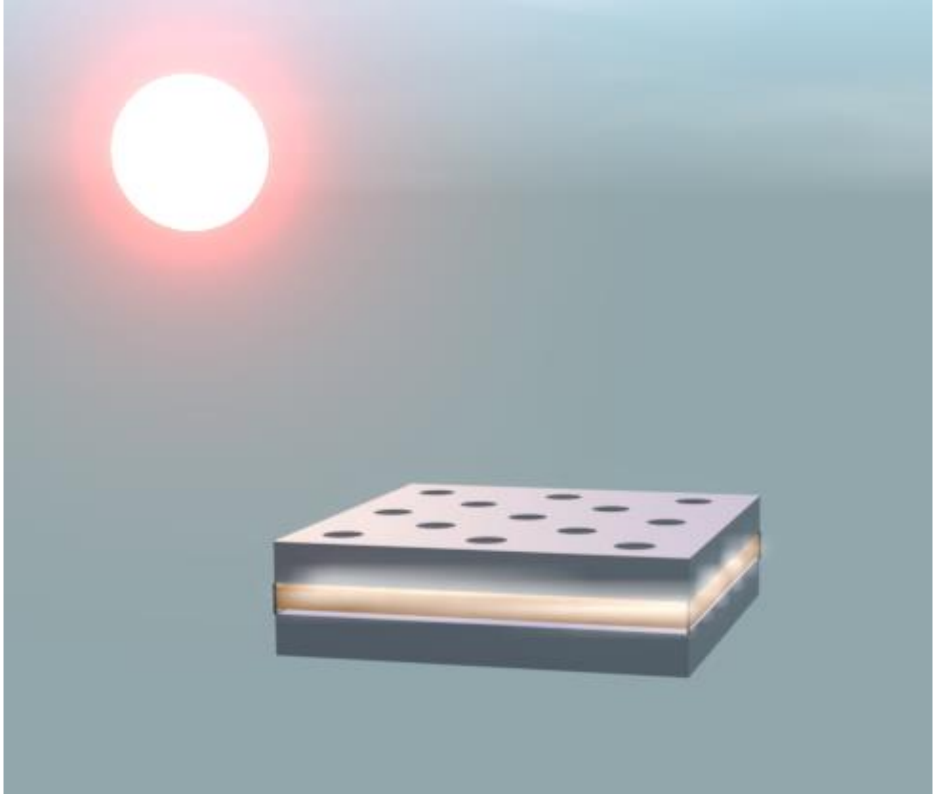

Figure 6.1: Schematic of a germanium hole array photonic crystal thermal concentrator, where the thickness is equal to the pitch of the holes. The thermal concentrator absorbs incident sunlight and traps the generated heat.

6.2 Designing a Photonic Crystal Thermal Concentrator

In designing a thermal photonic crystal, we first must choose a material that has experimentally realizable properties in the region of interest. As is the case in previous chapters, the ideal photonic crystal materials have a high index of refraction and low absorption coefficient in the region of interest[23]. Working in the atmospheric window eliminates the potential to use many common PCWG materials such as Si or TiO2 due to the polariton modes at long wavelengths that cause erratic jumps in optical behaviors, and the overall lower indices of refraction that limit overall emission trapping potential[22-25]. We therefore opt to use lightly doped germanium as the medium for the PCWG instead. Germanium is a promising material for such thermal concentrators due to its high index of refraction (n = 4) and previous investigations into germanium for use in thermal applications[25,26]. While two-dimensional photonic crystal rod and hole arrays have both demonstrated high trapping efficiencies, for this study we opt for a hexagonal germanium hole array[25]. The hole array is optimal for a thermal concentrator because previous work has shown that the hole array demonstrates a more robust trapping profile across a wider range of wavelengths whereas the rod array is more specific with its trapping wavelengths[22]. Given that the atmospheric window spans across 8–15 µm, it is preferable to find a design that is capable of trapping across many wavelengths of emission[21]. Also, hole arrays allow for the use of dispersal mediums for the emitters. Some catalytic reactions for solar fuels and their respective byproducts occur in solution[5,27]. Catalysts in heterogenous and homogenous systems can be dispersed into the hole array for efficient transfer of heat from the photonic crystal to the reactive catalyst. Furthermore, this increased index of refraction in the holes of the PCWG array contributes to an overall increase in the effective index of the PCWG and therefore increases the broadness of the trapping potential[22]. The last overall design consideration is the substrate; in order to maximize versatility of the design, we propose a PCWG with no substrate. This will allow the PCWG to be used in a variety of gas diffusion electrodes or solar thermochemical reactor cell. By assuming no substrate, we also allow a design in which reactive gas can be cycled through the device, flowing through the holes of the PCWG to interact with the catalysts[28,29].

The absorption profile of the photonic crystal thermal concentrators were calculated using a Lumerical FDTD simulation, similar to the one describe to analyze the reflection of spectrally-selective HCGs described in Chapter 3. The same code described in Chapter 4 and Chapter 5 was used to analyze the trapping potential of such thermal PCWGS. Each simulation to evaluate trapping potential is done by placing the emission at a single location in the photonic crystal. In order to best estimate a dispersion of heat emission throughout the volume of the holes and throughout the solution within the holes, we repeat the simulation for a variety of locations throughout the *x*, *y*, and *z* planes of the hole and average the trapping across all locations. In the simulation, the physical parameters are set via normalized units with respect to the pitch. The radius of the holes is set to a quarter of the size of the pitch. This is based on previous work and internal tests showing that this is an ideal ratio for trapping emission[22,23]. Given that we are aiming to trap emission in the micron range, the dimensions of the hole array will be substantially larger than the designs for nanophotonic applications. Prior studies have shown that a height of three times the pitch is ideal for energy trapping in holey PCWGs[22], and therefore we analyze that geometry as a starting point. Given the fabrication difficulty in creating a Ge film on the order of 10s of microns, we also simulate a relatively thin PCWG, with a thickness instead equal to the pitch. Lastly, we assume the emitter will be in some medium with a refractive index greater than air (n=1), either via submersion or via byproducts or moisture produced in the catalytic reaction. We therefore evaluate trapping potential at each thickness with both a hole index refraction of n=1.3 and n=1.5. An index of 1.3 best approximates emitters dispersed in water[30]. This also accounts for any moisture in the catalytic reaction. An index of 1.5 best approximates polymer or chemical solutions such as toluene which has been shown to be an effective dispersal medium for Ni based catalysts for applications such as oligomerization of solar fuel reaction byproducts[31,32] After the simulation is run in Lumerical, the results are analyzed via a python script. In the python script, we can set the desired wavelength of max trapping and from there the script will provide the physical parameters that will result in maximum trapping at the desired wavelength. Given that these designs trap over a wide wavelength range as opposed to optimizing around a single wavelength, we repeat that process across all desired wavelengths of trapping at 1 micron intervals. After obtaining a range of physical parameters and their respective trapping efficiencies, we linearly interpolate across the desired wavelength range of 8-15 um and weight the respective trapping efficiencies according to the blackbody spectrum at 373K. We repeat this process for each emission location in order to best simulate how heat is trapped throughout the entire volume of the holes. We then average across the volume to find the ideal physical parameters for maximum trapping. This process is outlined in Figures 6.2-6.6.

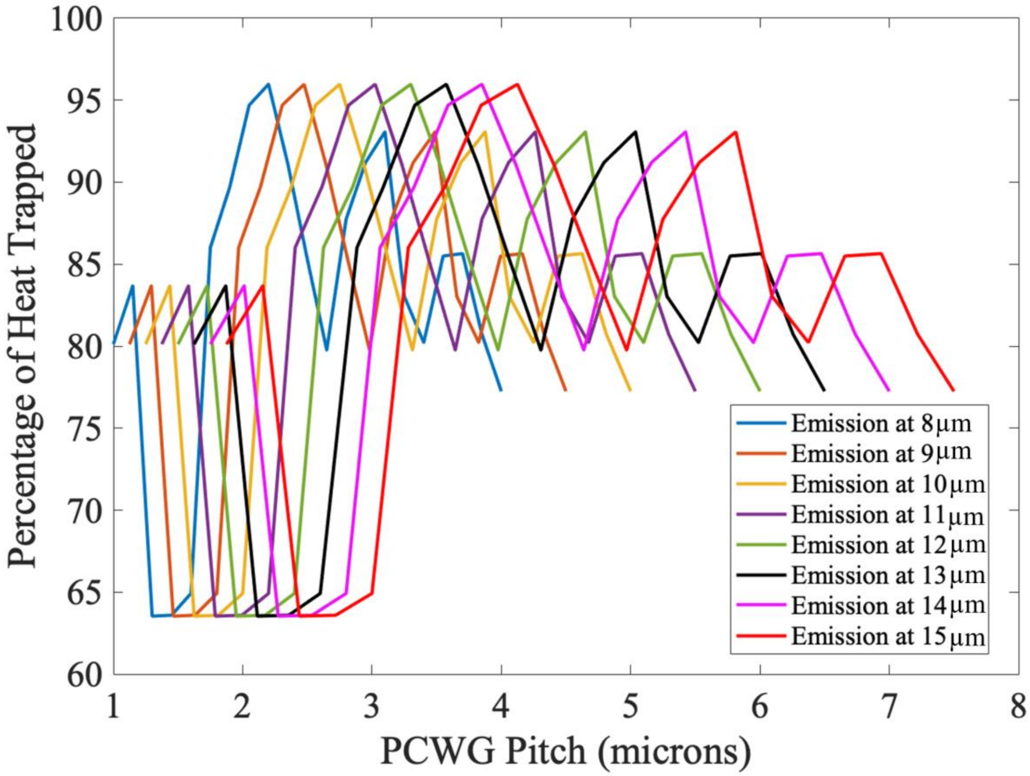

Figure 6.2: An example of trapping across all wavelengths of the atmospheric window as a function of photonic crystal waveguide pitch for a design with a hole index of n=1.3 and a thickness equal to that of the pitch. This simulation was performed with an emitter in the absolute center of the hole array.

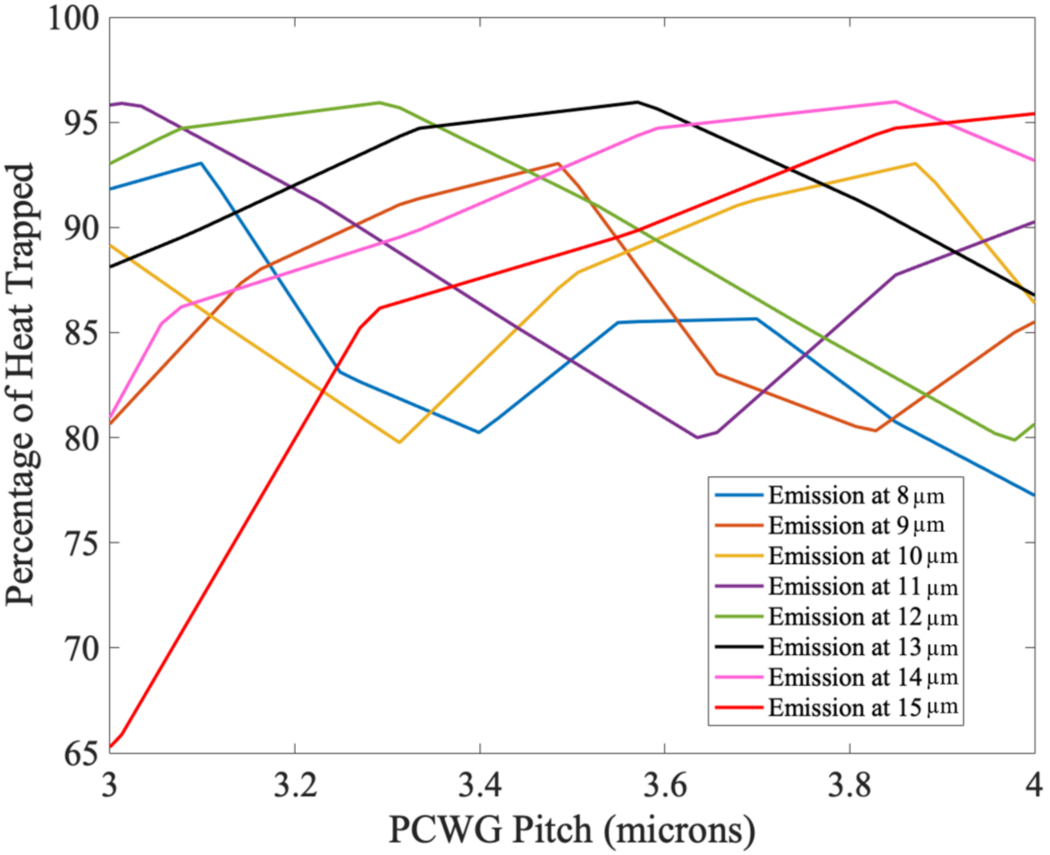

Figure 6.3: Isolation of the overlapping design regions to trap heat emission across all wavelengths of the atmospheric window as a function of photonic crystal waveguide pitch for a design with a hole index of n=1.3 and a thickness equal to that of the pitch. This simulation was performed with an emitter in the absolute center of the hole array.

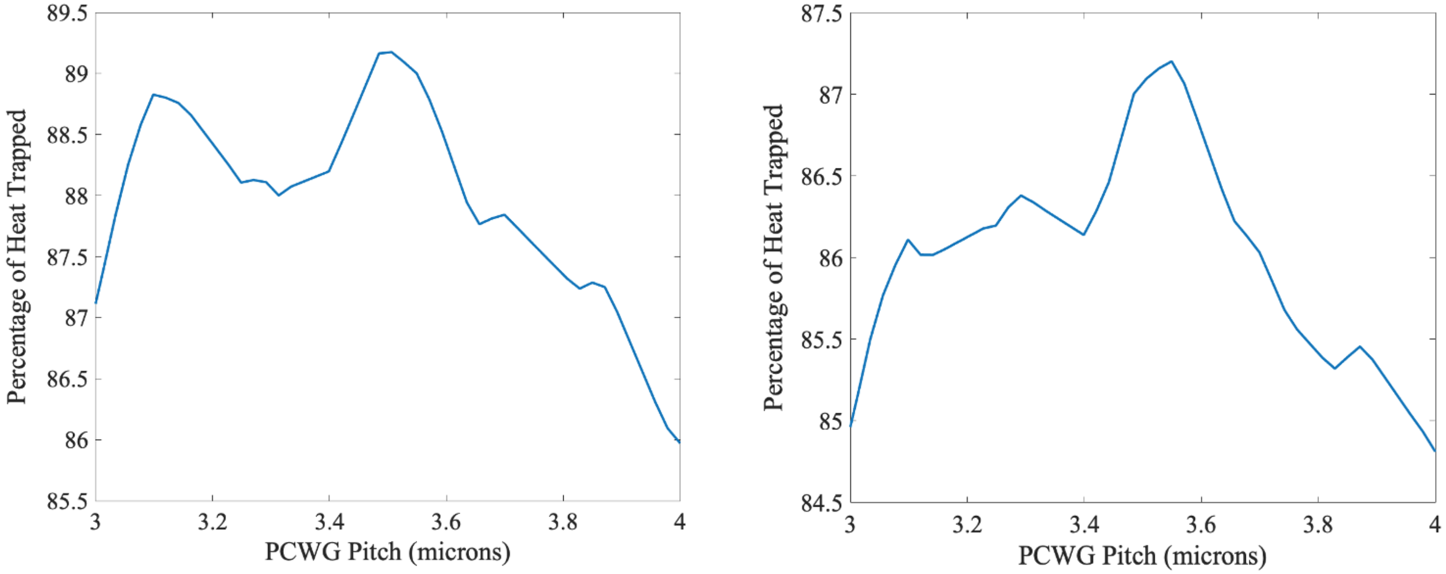

Figure 6.4: Linear interpolated average of the trapping percentage at each wavelength to get an overall analysis of trapping potential across the atmospheric window as a function of photonic crystal waveguide pitch. The left plot shows the trapping behavior assuming emission in the center of the hole array in the *x*, *y*, and *z* plane. The right plot shows trapping behavior assuming emission in the center of the *z* axis of the hole, but the edge of the hole. From this data, we integrate to determine the trapping of emission in a disk at the respective *z* location.

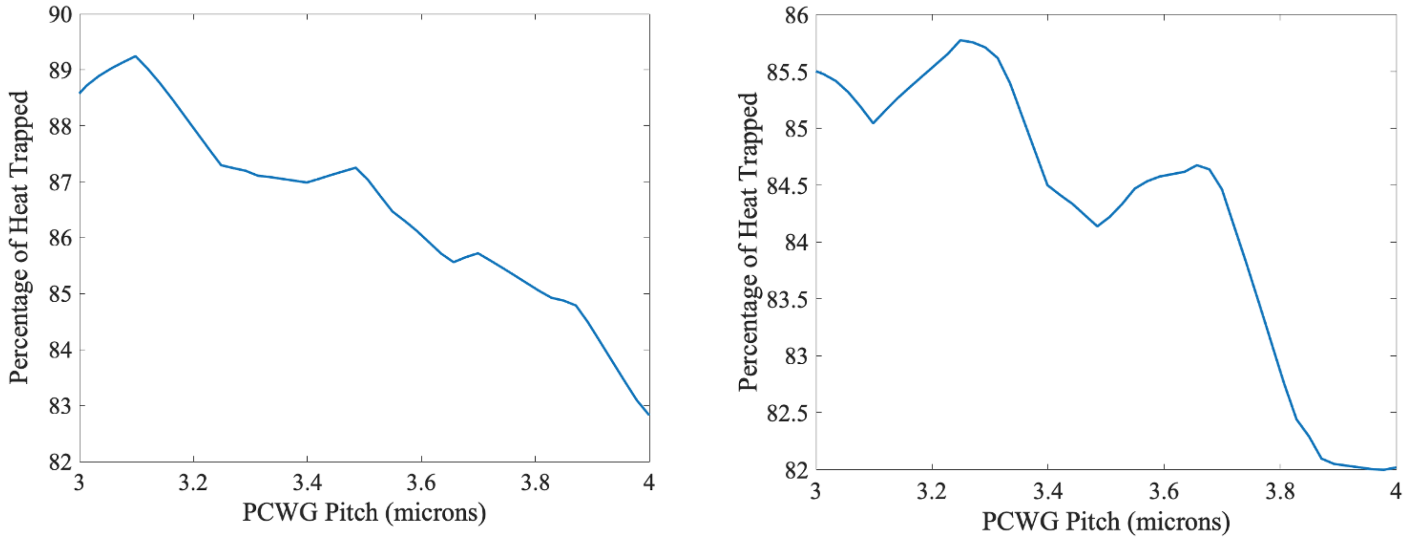

Figure 6.5: Linear interpolated average of the trapping percentage at each wavelength to get an overall analysis of trapping potential across the atmospheric window as a function of

photonic crystal waveguide pitch. The left plot shows the trapping behavior assuming emission in the center of the hole array in the *x* and *y* plane, but at the at the midpoint of the center and top of the hole in the *z* direction. The right plot shows trapping behavior assuming emission in the same location across the *z* plane, but along the edge of the *x* plane against the edge of the hole. From this data, we integrate to determine the trapping of emission in a disk at the respective *z* location. We repeat this calculation across the *z* direction to best approximate trapping throughout the hole volume.

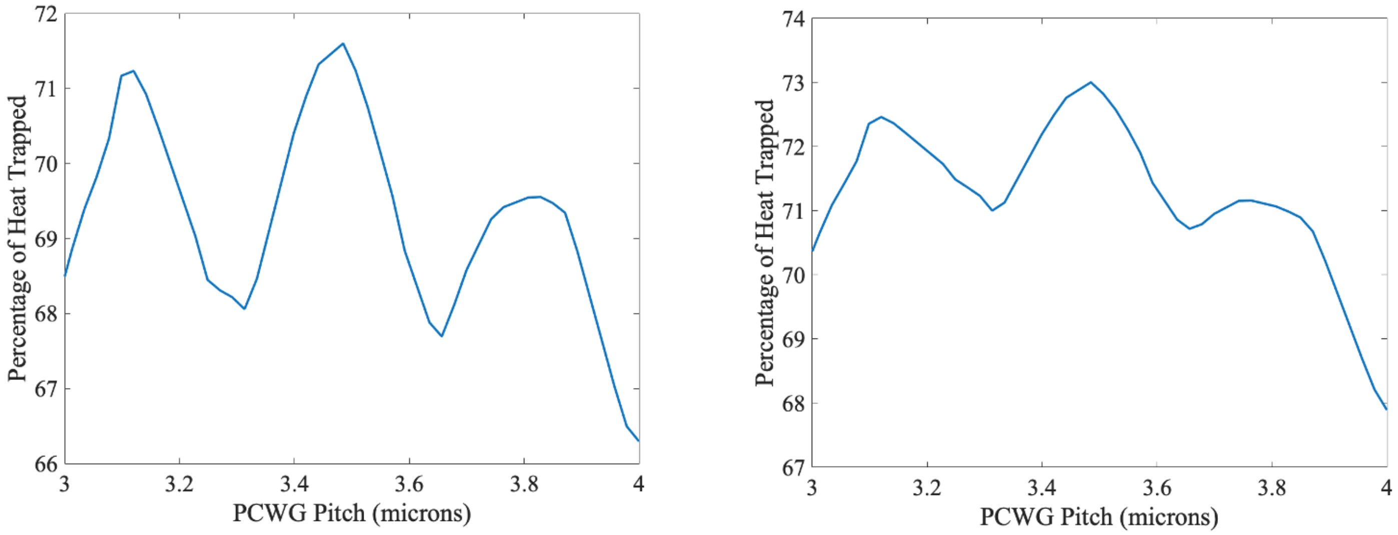

Figure 6.6: Linear interpolated average of the trapping percentage at each wavelength to get an overall analysis of trapping potential across the atmospheric window as a function of photonic crystal waveguide pitch. The left plot shows the trapping behavior assuming emission at PCWG-to-air boundary, at the center of the *x*, *y* plane. The right plot shows trapping behavior assuming emission in the same location across the *z* plane, but along the edge of the *x* plane against the edge of the hole. This is the extreme boundary of the trapping data, as it has the least amount of PCWG symmetry.

From the steps shown in Figures 6.2-6.6, we are able to construct an optimized PCWG, taking into consideration heat throughout the volume of the PCWG, trapping across wavelengths, and how each wavelength is disctributed across the plackbosy spectrum .We demonstrate in Figure 6.7 that if we assume an index of refraction of 1.3 inside the holes and optimize for maximum heat trapping, a PCWG with a pitch of 3.1 µm, thickness of 3.1 µm, and radius of 0.775 µm is able to trap 83.8% of heat across the atmospheric transmission window. In Figure 6.8, we show that upon repeating the simulations for an index of refraction of 1.5 inside the holes of a PCWG with the same physical dimensions, we achieve a trapping potential of 84.7%.

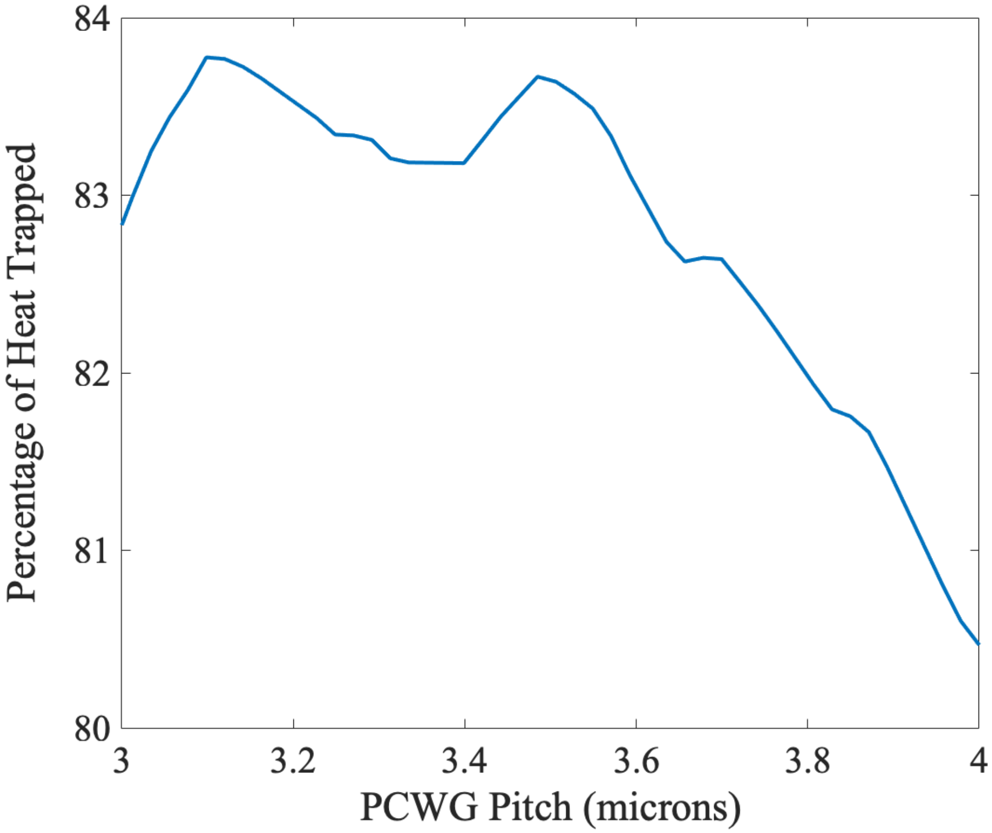

Figure 6.7**:** Percentage of heat trapped within the plane of a photonic crystal with a hole index of refraction *n* = 1.3 as a function of pitch where thickness is equal to the pitch. The trapping potential is averaged across the atmospheric transmission window (8 – 15 µm).

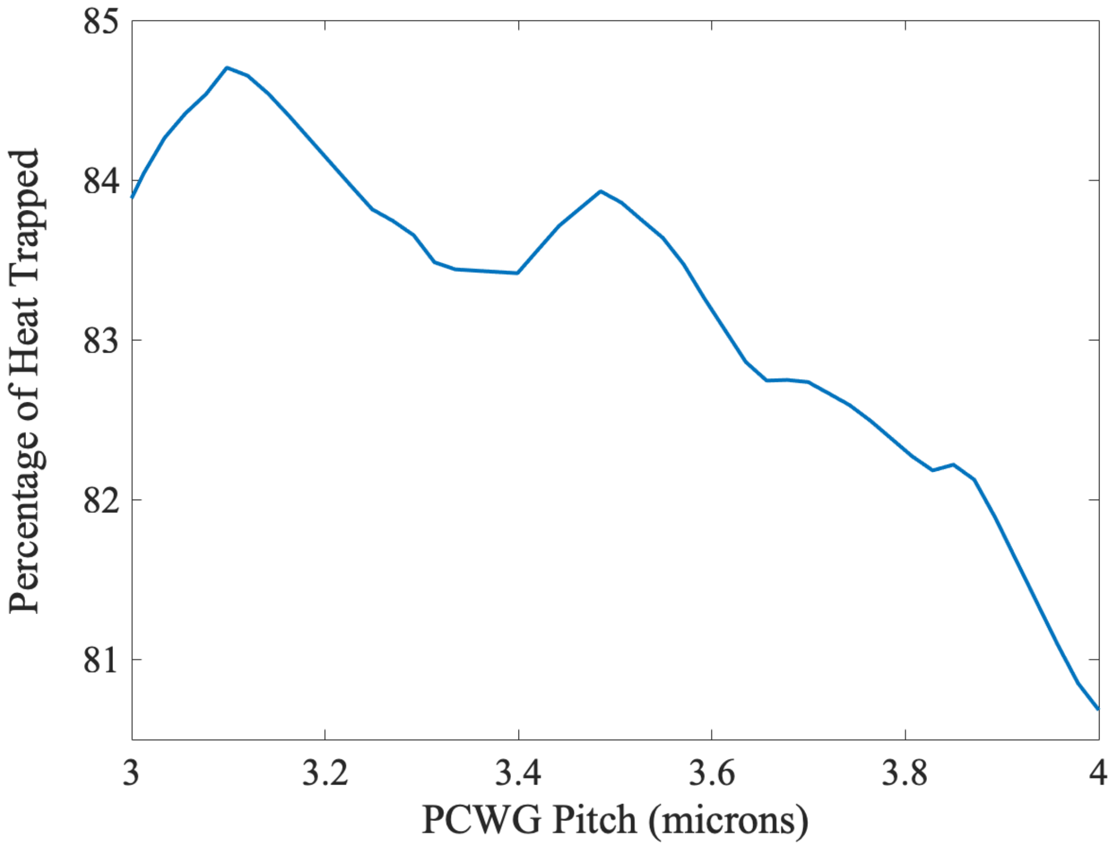

Figure 6.8**:** Percentage of heat trapped within the plane of a photonic crystal with a hole index of refraction *n* = 1.5 as a function of pitch where the thickness is equal to the pitch. The trapping potential is averaged across the atmospheric transmission window (8 – 15 μm).

6.3 Heat Trapping and Temperatures

Upon demonstrating the heat trapping efficiency, we must characterize that in terms of actual generated temperature within the PCWG to determine which solar fuel processes can be achieved in the PCWG. We define a thermal power balance to calculate the maximum achievable temperature within the PCWG taking into account the absorption of incident sunlight, loss of heat through radiative emission, and loss of heat through non-radiative processes with the environment. The power flux is defined as the following:

$$P_{net} = P_{sun} - P_r - P_{conv,cond} \tag{6.1}$$

From Equation 1, we define

$$P_{sun} = A \int_0^{\infty} I_{AM1.5}(\lambda) \epsilon_{PCWG}(\lambda, \theta_{sun}) d\lambda \tag{6.2}$$

as the total solar energy absorbed as a function of the PCWG emissivity ε_{PCWG}, and

$$P_r = 2\pi A \int_0^{\frac{\pi}{2}} \int_0^{\infty} I_B(\lambda, T_{PCWG}) \epsilon_{PCWG}(\lambda, \theta) \sin\theta \cos\theta \, d\lambda d\theta \tag{6.3}$$

as the thermal radiative emission as a function of ε_{PCWG} and the PCWG temperature T_{PCWG}, where

$$I_B = \frac{2hc^2}{\lambda^5} \frac{1}{e^{\frac{hc}{\lambda k_B T}} - 1} \tag{6.4}$$

is Planck's blackbody radiation law. Finally, we describe the non-radiative power flux as a first-order relationship with respect to temperature difference between the PCWG and its environment

$$P_{conv,cond} = qA(T_{PCWG} - T_{Ambient}) \tag{6.5}$$

where q is a non-trivial non-radiative heat coefficient which describes the combined effects of conductive and convective heat transfer between the environment and the PCWG, and $T_{Ambient}$ is the ambient temperature, set at 300 K. From Equations 1–5, we see that by solving for the case where $P_{net} = 0$, we can calculate the maximum temperature of the PCWG under any operating conditions, given its emissivity response.

In order to provide the absorption inputs for the thermal analysis, we used Lumerical FDTD with a planar wave light source with a wavelength range of 0.3 – 30 µm, a wavelength regime which covers both the AM1.5 solar spectrum and most of the blackbody radiation contribution above 300 K.. To do this, we set periodic boundary conditions around the hexagonal unit cell because we can assume uniform periodicity throughout the photonic crystal. Monitors are placed both above and below the photonic crystal in order to calculate the reflected and transmitted light. To calculate the absorptivity/emissivity of the PCWG, we then subtracted the sum of the reflection and transmission from unity.

Referring back to Equation 6.5, we analyze temperature as a function of q. If we set $q = 0$, we will get an absolute maximum theoretical temperature achievable by the PCWG based on optical properties alone. For the chosen reactor model under vacuum, we calculate a non-radiative heat transfer coefficient of $q = 1.7$ W/m2K. As an upper limit on non-radiative heat loss, we also use $q = 6$ W/m2K which is near the high end of the range commonly reported in literature for conductive/convective heat transfer on surfaces with basic thermal insulation design[33-37]. This range of q values is used to demonstrate the limits of the thermal performance of the PCWG under different possible operating conditions. We lastly consider solar illumination. 1 sun illumination refers to a PCWG accumulating heat from incident sunlight alone. 3 sun illumination refers to a PCWG surrounded by non-tracking mirrors. 3 sun is still quite scalable since there are not geometric concentrators or general tracking apparatuses needed. Performing the thermal analysis, we find that when q = 0 W/m2K, the PCWG reaches a maximum theoretical temperature of 662.3 K (389.2 °C) under 1 sun illumination. Repeating this process with 3 sun illumination, we find that the PCWG reaches a maximum theoretical temperature of 833.6 K (560.5 °C). Using our modeled q = 1.7 W/m2K, we find that the PCWG can still achieve temperatures of 507.3 K (234.2 °C) and 729.4 K (456.3 °C) under 1 sun and 3 sun illumination, respectively. For q = 6 W/m2K, the PCWG reaches temperatures of 376.8 K (103.7 °C) and 525.5 K (252.4 °C) under 1 sun and 3 sun illumination, respectively. Figure 6.9 shows the emissivity of the PCWG as calculated from Lumerical FDTD with the AM1.5 solar spectrum and blackbody curves for 662.3 K (389.2 °C) and 833.6 K (560.5 °C) overlaid.

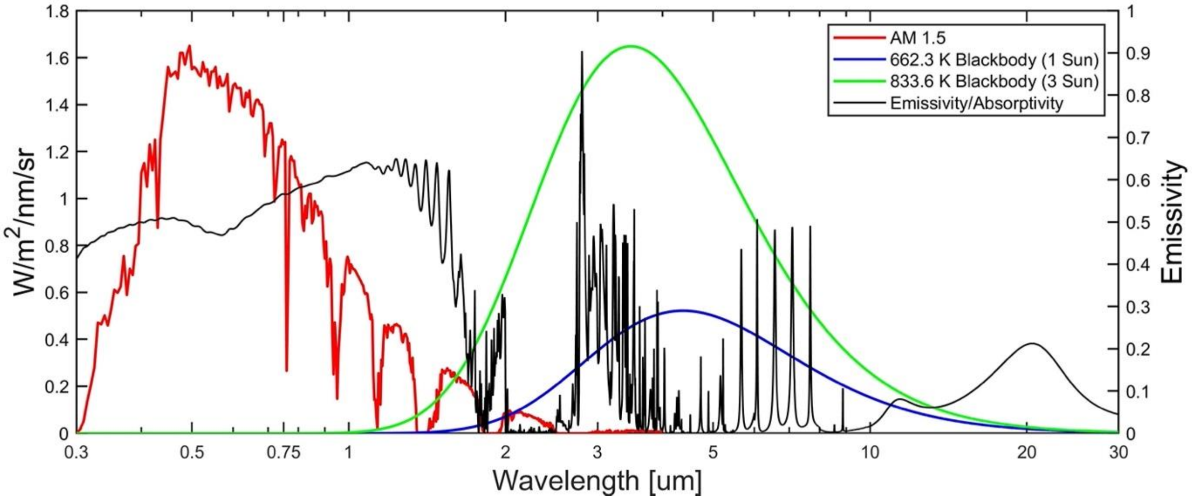

Figure 6.9**:** Emissivity of a germanium-based photonic crystal waveguide throughout the visible and infrared wavelength regime overlayed with the incident solar spectrum (AM1.5) and the Blackbody spectrum of the maximum theoretical achievable temperatures of the photonic crystal waveguide under both 1 sun and 3 sun illumination with $q = 0$ W/m^{2}K.

From the thermal analysis, we demonstrate that the PCWG is able to provide temperatures necessary to facilitate a wide range of solar thermochemical reactions. Most promising of our demonstrated temperatures is the path towards PCWGs for Fisher Tropsch reactions. Fischer-Tropsch reactions, which use nCO to produce methane, propane, or ethane are of particular interest because although they require elevated temperatures on the order of 475 – 630 K, they can occur at atmospheric pressure[5,9,10,38,39]. Furthermore, Fischer-Tropsch processes can be coupled to an electrochemical system that produces both CO and H2[40]. These qualities make the Fischer-Tropsch reaction an ideal candidate for a solar thermochemical fuel production module[39,41]. Fischer-Tropsch reactions generally occur in a gas-liquid process as opposed to in solution as analyzed in this paper. However, given the range of temperatures produced for both q = 1.7 W/m2K and q = 6 W/m2K, the slight decrease in light trapping from moving to n = 1 within the PCWG will not decrease to a point where the temperature will no longer reach the range of Fischer-Tropsch processes.

6.4 Initial Fabrication Ideas

The dimensions of the photonic crystal thermal concentrator pose some challenges from a fabrication standpoint. The previous photonic crystal fabrication methods are not easily translated to such a system. The first challenge is the thickness of the proposed thermal concentrator. Fabrication of a film on the order of >1 µm eliminates many deposition methods. To fabricate a 3 µm layer of Ge, the optimal method is sputtering from multiple targets. This spreads the power across targets therefore alleviating the power and duration applied to a single target to achieve the goal thickness. However, supplying a sputterer with multiple Ge targets is an investment beyond a simple proof of concept. We therefore opt to use PECVD deposition of a-Si. PECVD deposition is capable of fabricating thicker layers in a shorter period of time compared to other deposition methods such as sputtering or evaporation. a-Si has an index of refraction above 3, so while this is not as high as Ge, it provides a good starting point as a proof of concept. We also opt for a thinner layer (~1 µm) for this proof of concept as a 3 µm layer approaches the limit of the KNI PECVD before maintenance is required on the system. While this theoretically could reduce the overall temperature, that is not a guarantee as in our work we found the thinner PCWGs achieved higher temperatures despite lower trapping efficiencies.

Given that the radius of the holes is >1 µm, patterning via e-beam lithography is not efficient. However, we also opt to avoid conventional optical lithography methods to write the pattern as well. This is due to the thickness of the a-Si film. As we increase the film thickness, a simple pseudo-bosch etch will not be sufficient and instead a cryo-etch will likely be needed. This will require a new parameter sweep in order to optimize the recipe. At this stage of the fabrication, we opt for a more straight-forward fabrication process in place of a scalable industry-standard fabrication. We therefore write the pattern of the hexagonal array via nanoscribe into a negative toned resist deposited on a quartz substrate. The resist will then be developed leaving a “rod array” of resist. The a-Si will then be deposited around the remaining resist. The remaining resist will be cleared with an O_2 plasma leaving behind an a-Si photonic crystal thermal concentrator. Once the pattern in fully optimized, this process can use nanoimprint lithography instead of a nano scribe, increasing the output and scalability of manufacturing.

6.5 Discussion

Solar fuels are an important alternative to fossil fuels. In order for them to make a strong impact on the market, they must become more scalable. It is therefore advantageous to start with making mild catalytic reactions more scalable. We designed a PCWG capable of achieving high temperatures using incident sunlight alone eliminating the need for many structures that limit the scalability of such solar fuel reactors. In vacuum, we can achieve temperatures between 507.3K and 729.4 K opening the possibility for scalable Fischer-Tropsch reactions. Furthermore, temperatures of 525.5K can be achieved in ambient conditions for ethylene oligomerization.

This was a computational study, but the future for fabrication of such PCWGs is promising. Even if fabricated PCWGs are unable to achieve the Fischer-Tropsch conditions, there are many oligomerization and fuel production processes than can be run through the designed architecture. While the initial fabrication steps will be time consuming, once the optimized parameters are established, the fabrication process can be altered to become quite scalable.

References

1. Figueres, C.; *et al.* “Emissions are Still Rising: Ramp up the Cuts,” *Nature* **2018**, 564, 27−30.

2. Davis, S. J. *et al* “Net-zero Emissions Energy Systems,” *Science* **2018** 360,6396.

3. Rogelj, J *et al* “Zero Emission Targets as Long-term Global Goals for Climate Change,” *Environmental Research Letters* 10 **2015** 105007.

4. Rao, C. N. R and Dey, S. “Solar Thermochemical Splitting of Water to Generate Hydrogen,” *PNAS* **2017** 114 (51) 12285-13393.

5. Steinfeld, A. “Solar Thermochemical Production of Hydrogen-A Review,” *Energy* **2005** 78, 5, 603-615.

6. Stangeland, K; *et al* CO_2 “Methanation: The Effect of Catalyst and Reaction Conditions, “*Energy Procedia* **2017** 105, 2022-2027.

7. Vogt, C., Monei, M., Kramer, G.J. *et al* “The Renaissance of the Sabatier Reaction and its Applications on Earth and in Space,” *Nature Catalysis* **2019** 2, 188-197.

8. Smith, C., Hill, A.K., Torennte-Murciano, L. “Current and Future Role of Haber-Bosch Ammonia in a Carbon-free Energy Landscape,” *Energy and Environmental Science* **2020** 13, 331-344.

9. Mac Dowell, N., Fennell, P., Shah, N. *et al* “The Role of CO_2 Capture and Utilization in Mitigating Climate Change,” *Nature Climate Change* **2017** 7, 243-249.

10. Xu, Y., Li, J., Li, W. *et al”* Direct Conversion of CO and H_2O into Liquid Fuels Under Mild Conditions,” *Nat Communications* **2019** 10, 1389.

11. Zhang, X.*et al.* “A Stable Low-temperature H_2-Production Catalyst by Crowding Pt on α-MoC,” *Nature* **2020,** 589**,** 396–401.

12. Yao S. *et al* “Atomic-layerd Au Clusters on α-MoC as Catalysts for the Low-temperature Water-gas Shift Reaction,” *Science* **2017** 357, 389-393.

13. Finiels, A., Fajula, F., Hulea, V., “Nickel-based Solid Catalysts for Ethylene Oligomerization – a Review,” *Catalytic Science and Technology.*, **2014**, 4, 2412-2426.

14. Goetien, T. A., Zhang, X., Liu, J., Hupp, J.T., Farha, O.K.” Metal-organic framework supported single site chromium (III) catalyst for Ethylene Oligomerization at Low Pressure and Temperature,” *ACS Sustainable Chemistry and Engineering* **2019**, 7 (2) 2553-2557.

15. Boretti, A., Castelletto, S., Al-Zubaidy, S. “Concentrating Solar Power Technology: Present Status and Outlook,” *Nonlinear Engineering* **2019** 8, 10-31.

16. Phillips, S., Bett, A.W., Horowitz, K., Kurtz, S., “Current Status of Concentrator Photovoltaic (CPV) Technology,” *ISE and NREL* **2015** .

17. Low, J., Zhang, L., Zhu, B., Liu, Z., Yu, J. “TiO_2 Photonic Crystals with Localized Surface Photothermal Effect and Enhanced Photocatalytic CO_2 Reduction Activity,” *ACS Sustainable Chemical Engineering* **2018** 6, 15653-15661.

18. Rostami, M., Talebzadeh, N., O’Brien, P.G., “Transparent Photonic Crystal Heat Mirrors for Solar Thermal Applications,” *Energies* **2020** 13, 1464.

19. Ozbay, E. “Layer-by-layer Photonic Crystals from Microwave to Far-infrared Frequencies,” *Journal of the Optical Society of America B* **1996** 13, 1945-1955.

20. Ozbay, E., Temelkuran, B., Bayindir, M., “Microwave Applications of Photonic Crystals,” *Progress in Electromagnetics Research* **2003** 41, 195-209.

21. Li, W. and Fan, S. “Radiative Cooling: Harvesting the Coldness of the Universe,” *Optics and Photonics News* **2019** 30, 32-39.

22. Bauser, H.C., Bukowsky, C.R. *et al “*Photonic Crystal Waveguides for >90% Light Trapping Efficiency in Luminescent Solar Concentrators,” *ACS Photonics* **2020** 7, 2122-2131.

23. Joannopoulos, J. D.; Johnson, S. G.; Winn, J. N.; Meade, R. D. “Photonic Crystals: Molding the Flow of Light,” 2nd ed.; Princeton University Press: Princeton, **2008.**

24. Novotny, L.; Hecht, B. “Principles of Nano-Optics,” Cambridge, U.K., **2006**.

25. Li, H.H. “Refractive Index of Silicon and Germanium and its Wavelength and Temperature Derivatives,” *Journal of Physical and Chemical Reference Data* **1980** 9, 561.

26. Thomas, N. H., Chen, Z., Fan, S., Minnich, A.J. “Semiconductor-based Multilayer Selective Solar Absorber for Unconcentrated Solar Thermal Energy Conversion,” *Scientific Reports* **2017** 7, 6362.

27. Montoya, J.H., Seitz, L., Chakthranont, P. *et al “*Materials for Solar Fuels and Chemicals,” *Nature Materials* **2017** 16, 70-81.

28. Higgins, D., Hahn, C., Xiang, C., Jaramillo, T.F., Weber, A.Z., “Gas-Diffusion Electrodes for Carbon Dioxide Reduction: A New Paradigm,” *ACS Energy Letters* **2019** 4, 317-324.

29. Cheng, W., Richter, M.H., Sullivan, I., Larson, D.M., Xiang, C., Brunschwig, B.S., Atwater H.A.A. “CO_2 Reduction to CO with 19% Efficiency in a Solar-Driven Gas Diffusion Electrode Flow Cell under Outdoor Solar Illumination,” *ACS Energy Letters* **2020** 5, 470-476.

30. Zajac, A., Hecht, E. “Optics”, Fourth Edit. *Pearson Publishing* **2003.**

31. Myers, T.L., Tonkyn, R.G., Danby, T.O., Taubman, M.S., Bernacki, B.E., Birnbaum, J.C., Sharpe, S.W., Johnson, T.J. “Accurate Measurement of the Optical Constants n and k for a Series of 57 Inorganic and Organic Liquids for Optical Modeling and Detection,” *Applied Spectroscopy.* **2018** 72, 535-550.

32. Cooley, N.A., Green, S.M., Wass, D.F., Heslop, K. Orpen, A.G., Pringle, P.G. "Nickel Ethylene Polymerization Catalysts Based on Phosphorus Ligands," *Organometallics* **2001** 20, 23, 2769-4771.

33. Test, F. L., R. C. Lessmann, and A. Johary. "Heat Transfer During Wind Flow Over Rectangular Bodies in the Natural Environment," *Heat Transfer* **1981** 103, 262-267.

34. Sharples, S., and Charlesworth, P. S. "Full-scale Measurements of Wind-induced Convective Heat Transfer from a Roof-mounted Flat Plate Solar Collector," *Solar Energy*, **1998** 62(2), 69-77.

35. Hossain, M. M., and Gu, M. "Radiative Cooling: Principles, Progress, and Potentials," *Advanced Science*, **2016** 3(7), 1500360.

36. Zhao, D., Aili, A., Zhai, Y., Lu, J., Kidd, D., Tan, G.,Yang, R. "Subambient Cooling of Water: Toward Real-world Applications of Daytime Eadiative Cooling," *Joule*, **2019,** 3(1), 111-123.

37. Zhao, D., Aili, A., Zhai, Y., Xu, S., Tan, G., Yin, X., & Yang, R. "Radiative Sky Cooling: Fundamental Principles, Materials, and Applications," *Applied Physics Reviews*, **2019,** 6(2), 021306.

38. Jahangiri, H., Bennett, J., Mahjoubi, P., Wilson, K., Gu, S. "A Review of Advanced Catalyst Development for Fischer-Tropsch Synthesis of Hydrocarbon from Biomass Derived Syn-gas," *Catalytic Science Technology* **2014,** 4, 2210-2229

39. Wu, H., Zhang, F., Li, J., Tang, Z. Xu, Y. "Photo-driven Fischer-Tropsch Synthesis," *Journal of Materials Chemistry A* **2020** 8.24253-24266

40. Li, X., Anderson, P, Jhong, H. M., Paster, M., Stubbins, J.F., Kenis, P.J.A. "Greenhouse Gas Emissions, Energy Efficiency, and Cost of Synthetic Fuel Production Using Electrochemical CO_2 Conversion and the Fischer-Tropsch Process," *Energy Fuels* **2016** 30, 7, 5980-5989.

41. Rytter, E., Souskova, K., Lundgren, M.K., Ge, W., Nannestad, A.D., Venvik, H.J., Millestad, M. "Process Concepts to Produce Syngas for Fischer-Tropsch Fuels by Solar Thermochemical Splitting of Water and/or $CO_{2,}$"*Fuel Processing Technology* **2016** 145, 1-8.

Chapter 7

SUMMARY AND OUTLOOK

In the presented work, we have discussed nanophotonic strategies to manipulate incident sunlight for uses in a variety of net-zero emission technologies. In Chapter 1, we provided an overview of the current climate landscape as well as a brief discussion on the principles of photovoltaic and solar-thermochemical energy. We also covered some of the important nanophotonic concepts relevant to understanding the presented work in the following chapters. The references in Chapter 1 provide great resources for further in-depth readings on the field of nanophotonics and the building blocks upon which we analyze how light interacts with various mediums.

In Chapter 2, we introduced a novel architecture for luminescent solar concentrators. While LSCs are not a new concept, recent advances in luminophores via highly efficient and high Stokes shift quantum dots open the potential for record breaking LSC efficiencies. In order for the co-planar architecture in the tandem LSC to achieve the theoretical efficiencies found via Monte Carlo ray trace simulations, substantial effort will have to be applied on the engineering side of the fabricating the co-planar micro-cell array. To apply the number of micro-cells needed for the optimal geometric gain, we need industrial methods as opposed to research lab methods. By optimizing the fabrication of each individual component of the LSC, higher efficiencies are within reach.

In Chapter 3, we aimed to improve the efficiency and scalability of LSCs by designing and fabricating a spectrally selective HCG filter. HCGs consist of a single layer of material patterned onto a substrate at a sub-wavelength thickness. We first pursued AlSb as a HCG material. Upon finding we were unable to fabricate lossless AlSb films, we pivoted to using a-SiC:H as a HCG material. We were able to achieve reflectivity above 94% in the visible spectrum. To our knowledge this is the first demonstration of a-SiC:H as a material for high index contrast nanophotonics. Furthermore, to our knowledge, this is the first demonstration of such high reflectivity in the visible spectrum using a spectrally selective HCG reflector. I believe this work is relevant both for LSCs, and the broader nanophotonics community via phase change metasurface and display technology applications. There are many exciting directions to take this work going forward. The first is to perform a full analysis of reflectivity as a function of angle of incidence. While previous work has shown that HCGs generally do not suffer from the blue-shifting demonstrated by Bragg filters, it would be valuable to perform a full in-lab analysis of this property. In order to do so, the HCG arrays will have to be larger in area to be analyzed in an integrating sphere. This will require some troubleshooting with e-beam lithography techniques. I made some progress on this using the Multipass function, but there is still more optimization to cover. Second, fabricating such a HCG via nanoimprint lithography would open the possibility for scalable manufacturing for such a HCG. The NILT tool in the KNI is capable of fabricating a 6 inch wafer of a spectrally selective HCG reflector. Lastly, I believe it is of use to try and fabricate a spectrally selective reflector on a polymer like CP1 to explore HCGs as a light weight reflector for space based solar power applications.

In Chapter 4, we designed photonic crystal waveguides as nanophotonic luminescent solar concentrators. We showed that both two-dimensional rod and hole arrays are capable of trapping over 90% of emission when coupled to quantum dots and achieving record-breaking concentration factors above 100. Furthermore, the added Purcell enhancement generated by the increased local density of states available for the QD can increase the photoluminescent quantum yield of the QDs. We then fabricated hole arrays informed by the simulated PCWGs. The next step is to integrate the QDs into the hole array. Further exploration can be done here with both QDs in solution via the capillary force method outlined in the chapter, and spin coating and curing polymers with suspended QDs. The next step after QD dispersion is to test the trapping by coupling the system to a PV. There is additionally potential challenges in the etching process that may arise when repeating the hole array fabrication in thicker samples, especially given the high aspect ratio caused by the difference between the radius and thickness. It might be advantageous to switch to a hard mask fabrication proves to protect the structure of the PCWG.

In Chapter 5, we discussed the exciting new potentials for LSCs as a space based solar power technology. In 2023, Caltech will launch the first LSC into orbit. This current LSC design will be a test of both efficiency and viability of many of the LSC materials that have not undergone extensive testing for durability in orbit. We then analyzed how PCWGs can help push the theoretical maximum achievable specific power for space-based LSCs. We found that by coupling a PCWG to a CP1 substrate with a co-planar micro-cell array, we achieve specific powers as high as 11.5 kW/kg. Many of the furfure directions outlined in previous paragraphs are precursors for advancement in the fabrication of PCWGs for SSP applications.

Finally in Chapter 6, we discussed how PCWGs can be scaled to act as thermal concentrators for solar-thermochemical production of solar fuels. We demonstrated that Ge PCWGs are able to trap 83.8% of heat absorbed by the PCWG. This translates to temperatures as high as 729.4K under vacuum and 3 sun illumination. In ambient conditions, the thermal concentrator can reach temperatures up to 525.5K under 3 sun illumination. These temperatures can foster a catalytic environment for many low-temperature solar fuel and oligomerization processes including Fischer-Tropsch reactions that are of great interest in CO_2 reduction. The thermal concentrator is an exciting step towards scalable solar-thermochemical catalysis. There are still many fabrication steps necessary to realizing such a structure. It is recommended to use a nano-scribe for a first iteration as a proof of concept. The thick nano-scribe resists will allow the user to avoid any etching step that will add a substantial time to the troubleshooting process.

Through continued work, the presented optical designs are experimentally realizable. This work has demonstrated the value of nanophotonic solutions in the fight for scalable net-zero energy productions both terrestrially and in orbit.

APPENDIX: A NANOFABRICATION GUIDE FOR ALL LEVELS

A.1 Introduction to Nanofabrication

Nanofabrication has been a focus of mine throughout my work towards this thesis. Nanofabrication broadly refers to techniques necessary to make structures on the nanoscale. I have found that a lot of nanofabrication expertise does not necessarily get transferred between years and cohorts. Part of this is due to the specific nature of many nanofabrication recipes. However, I still believe part of my responsibility in publishing a thesis is to share nanofabrication lessons I have learned over the years. This section is adapted from a presentation and contains an overview of common nanofabrication tools, analysis techniques, and general tips learned over the years. My aim is for this chapter to help everyone from new lab members wanting to learn what different tools actually do, to more advance users trying to overcome snags in their processes. While most of the information in this section is relevant for all nanofabrication labs, I performed all of my work in the Kavli Nanoscience Institute so some statements may be more specific to equipment in that lab. Additional resources can be found on the **Kavli Nanoscience Institute Wiki.** This has been **the most** valuable resource for me during all of my nanofabrication work and will have more tool specific detail than this appendix.
Before you enter the lab, I would suggest considering the following:

- What equipment is available to me and what are the limitations of the equipment?
- Have previous researchers used similar methods before?
- Are there components that I should order or outsource to a different lab or company?
- Is what I am trying to do physically possible?

The following sections should also help you answer those questions if you are currently unsure.

A.2 Deposition Methods

Evaporation

The two primary physical vapor deposition methods that you will find in lab are Evaporation and Sputtering. Evaporation is done either via electron beam (e-beam) or thermally. Thermal evaporations systems and e-beam systems are fairly similar in applications and capacity, but thermal evaporation tends to be slower and dirtier. E-beam evaporation is used to deposit metals and metal oxides. When deposition a metal oxide, it is generally preferable to use a steady O_2 gas flow rather than evaporate from an oxide source. This gives the user more reliable control of the stoichiometry. The thickness of evaporated films is usually on the order of 10s to 100s of nanometers. Evaporation is not an ideal technique for deposition conformal thin films over intricate structures.

Sputtering

The other common physical vapor deposition method is Sputtering. Sputtering is more flexible in deposition capacity as you can use a sputterer to deposit dielectrics, metals, metal oxides, and chalcogenides. Furthermore, the user has a lot of recipe control in sputter systems. Making it a good option for making alloys and co-deposited materials. Furthermore, user control allows for substantially better step coverage over intricate structures. Better step coverage can also be achieved by slowing down your deposition rate. Sputtered film thickness can range from a few nanometers to 100s of nanometers. The only real limitation in thickness is the target limitations. Lightweight targets are typically more sensitive to high power exposure over long periods of times. By trying to sputter more than a target is capable or, you can shatter the target which compromises the whole system.

Atomic Layer Deposition

Atomic Layer Deposition (ALD) is ideal for the fabrication of high quality very thin films (<10s of nms). ALD is also generally considered to have the best step coverage of any deposition system so is ideal for depositing nanometers of material on intricate structures. ALDs are used to deposit TiO_2, SiO_2, Al_2O_3, other metal oxides, occasionally metals, and rarely nitrides.

Plasma Enhanced Chemical Vapor Deposition

Plasma Enhances Chemical Vapor Deposition (PECVD) is used for Si, amorphous Si, silicon carbides, silicon nitrides, and SiO_2. PECVD is ideal for the deposition of thick layers on the order of 100s of nanometers and even into the micron range. Fabricable recipes depend on the gases available for your process. For example, in Chapters 3 and 4 we discussed collaborating with ASU because their PECVD has H_2 capabilities that the Caltech PECVDs do not.

Metalorganic Chemical Vapor Deposition

Metalorganic Chemical Vapor Deposition (MOCVD) is primarily used for semiconductor growth. This is how materials like InGaP, GaAs, InP, etc. are grown. Molecular beam epitaxy is used to grow II-VI semiconductors, but that tool is outside of the scope of my work. This is one of the more challenging tools to use. People dedicated their entire careers to MOCVD growth. So my personal advice for if you ever have to grow a III-V or any other material requiring an MOCVD is to find an outside collaborator for this step.

A.3 Lithography

Lithography is a term derived from ancient Greek meaning “to write in stone.” Simply, lithography is the broad term for the method by which you write your desired pattern onto your sample. Figure 3.15 gives an example of a lithographic process. Generally in lithography, you apply some chemical resist, apply a mask with you desired features, espies your sample to some energy that affects the solubility of your resist, develop the pattern washing away unwanted resist, then etch the exposed pattern. Resists that you write your pattern into are generally characterized as positive or negative. A positive resist is one where the region of your pattern exposed to the energy source become soluble. A negative resist is one where the region of your pattern unexposed to the energy source becomes soluble. A diagram of this is given in Figure A.1 In this section, I will give an overview of the two common lithography techniques: Photolithography and E-Beam lithography. I will also cover some of the e-beam lithography tips I have learned over the years. The e-beam section will be more detailed as that is where I have spent more of my time.

Figure A.1: The left two figures show the result of a positive tone resist used to write a pattern. The right two figures show the result of a negative tone resist used to write a pattern.

Photo/Optical Lithography Overview

Photolithography (also called optical lithography) is a great pattern writing method for larger features on the order of 10s-100s of microns. The energy source imprinting your pattern into the resist is UV light. For photolithography you start by making your mask in a CAD software of your choice. You then send your pattern to a photomask supplier to make the physical mask of your patter. Photolithography masks are generally either chrome or FeO. FeO masks are generally preferred because they are transparent making alignment in the tool much easier. It is still recommended to make markers on your sample if the pattern alignment is important to your sample. When performing photolithography, it is important to keep all steps in one room as changes in humidity can affect the performance of the resist and changes an light can potentially affect your process by exposing your resist too early.

The following formula is the method by which you calculate exposure time. The dose will be determined by the machine and the resist you use so check the manufacturing sheet for the resist.

$$exposure\ time = \frac{dose}{power}$$

(A.1)

Below is a list of common photolithography resists along with their respective developers, separated by whether the resist is positive or negative.

Positive:

- S1813, develop with MF-319
- AZ 5214-E, develop with AZ 917-MIF
- AZ 9260, develop with AZ 400k
- AZ P4620, develop with AZ400k/water mix 1:3 ratio
- nLoF 2070, develop with AZ 726

Negative:

- NR9-1000PY, Develop with RD6
- AZ 5214-E, develop with AZ 917-MIF
- SU-8, develop with PGMEA

E-Beam Lithography Overview

E-beam lithography is the method you will need to write any patterns with feature sizes on the order of the nanoscale. With e-beam lithography, you can also make large patterns with features on the order of microns to nanometers. E-beam lithography involves a lot of finer details that are typically not covered in training. Before you start e-beam lithography try and learn as much as you can about the process. In this section, I will try to cover some of the general tips and need-to-knows before you being a process.

The first thing you will do in an e-beam lithography process is build your structure in CAD. Make sure you do this before your training. You will then put that CAD file in a process flow on the Layout BEAMER computers in the KNI. This process flow will involve importing your CAD file then converting it into a file format that the e-beam computer can read (.gpf). In this process flow, above all else I recommend beginning with a Proximity Effect Correction (PEC). This will help you with weird patterning issues from the start. It prevents pattern and write overlaps and unpatterns edges of your sample. You build it based on depth simulations with your resist, resist thickness, substrate thickness, and film thickness. This will be covered a bit in training. However, my secondary use for a PEC is as a periodicity function. Rather than making a large pattern in CAD, I instead make a pattern that is 20 microns in width and height. I then use the periodicity function in the PEC builder to make large patterns. This prevents the beamer software from crashing as it tends to do if you have a very large CAD file. This allows for fast processing of my .gpf file needed for the e-beam computer.

Another very important component in layout beamer is the fracturing of your beam. Do not ever use default fracturing. Fracturing is adjusted in the "export gpf" phase of developing your process flow. Default fracturing, no matter what shapes you are trying to make, will mess up your pattern. Generally the default fracturing mode is "large rectangle fine trapezoid" which tries to find shapes in your pattern. Conventional fracturing has a similar result. Both of these are shown in in Figure A.2. This does not work if you have rounded edges, but I would argue that it is a liability regardless of the shape you are trying to make. It is better to opt for either Sequence or Shape Detection Mode that use smaller beam shots to more accurately build your structures. In Figure A.1, you can see that the pattern made using Shape Detection Mode is much cleaner and reliable. You will have to adjust the beam resolution and step size in the export in the gpf section in order to get the beams to form a perfect spiral in your gpf.

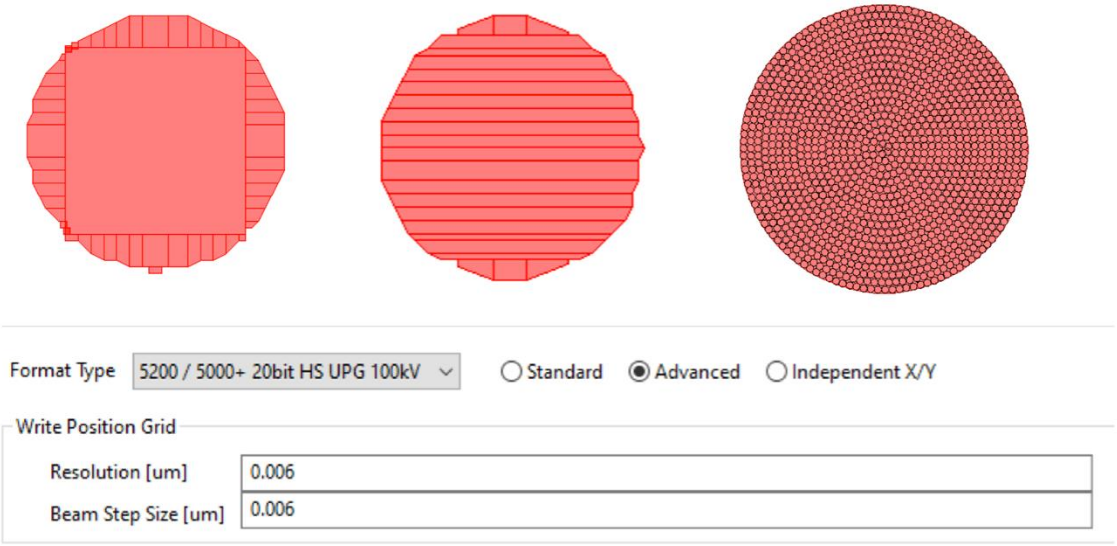

Format Type: 5200 / 5000+ 20bit HS UPG 100kV

○ Standard ● Advanced ○ Independent X/Y

Write Position Grid

Resolution [um]: 0.006

Beam Step Size [um]: 0.006

Figure A.2: Demonstration of the importance of proper beam fracturing. The top left image is using "large rectangle fine trapezoid" fracturing. The top middle is using conventional fracturing. The top right is using shape detector with a spiral writing of the beam shots. The bottom shows the resolution and beam step size that the user has to adjust in order to generate a perfect spiral of beam writes into their pattern.

Once you have converted your CAD file into a gpf, you can make adjustments in the actual beam write. The first step is deciding a current along with an aperture. Current can affect your feature size and run time. Larger spot sizes than you need can result in feature errors, but you also do not want a current so low that it drastically increased your run time. Balance is important here.

The next important setting is the dose of the beam. The first thing you should do when starting a new write is to run a dose array. Generally your resist data sheet will have a rough guideline for recommended beam dosing. However, I have found that a lot of these guidelines do not include the high accelerating voltage (100keV) that the KNI EBPG tools operate with. Dosing should always be your **first step** when optimizing parameters for lithography. Dosing can override the feature size you set in CAD if you do not choose properly, as shown in in Figure A.3. I recommend running a sweep across doses and checking under optical microscopy if possible to make sure your feature size is as expected.

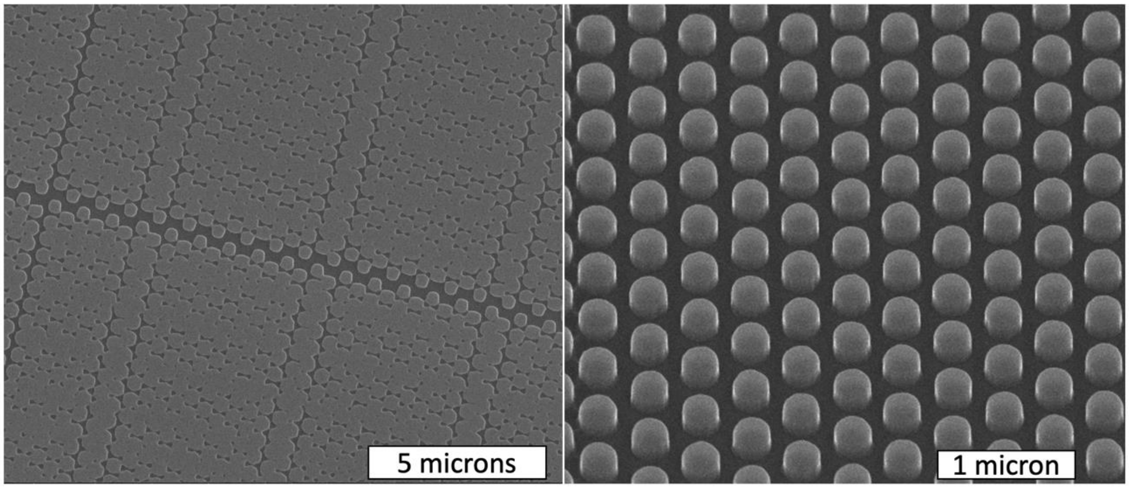

Figure A.3: The 5 micron scale image shows a pattern over-dosed at 600 uC/cm^2. The 1 micron scale image shows the same pattern properly dosed at 380 uC/cm^2.

Below is a list of common e-beam lithography resists along with their respective developers, separated by whether the resist is positive or negative.

Positive:

- PMMA, develop with MBK/IPA
- ZEP 520A, develop with ZEP-RD, N50, or SD
- SML, develop with MBK/IPA

Negative:

- HSQ, develop with 25% TMAH
- ma-N 24xx, develop with MF 319

In my work, I spent a lot of time working with dielectrics and glass. These materials are insulators. This means that when we expose them to a strong accelerating voltage like the one in an e-beam pattern generator, the charge builds up and accumulates on the surface. This leads to warping of your pattern. Figure A.4 demonstrates how this buildup of charge affects a pattern.

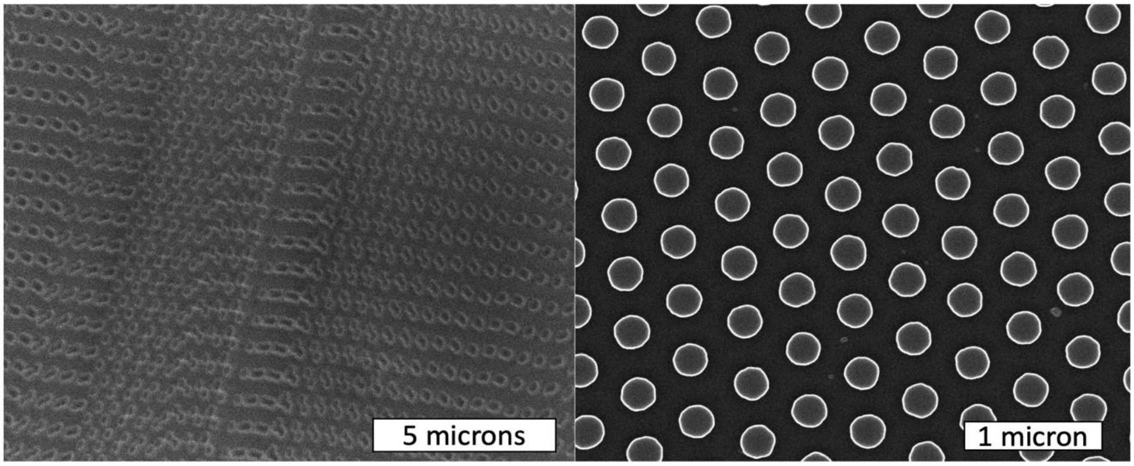

Figure A.4: The left SEM shows a pattern with charge accumulation. The right SEM shows a pattern properly written without charge accumulation.

Fortunately, the solution to overcome such charge buildup is simple, though slightly different depending on your resist. In order to remove charge buildup, you need to add a conductive layer to wick away charge that warps your sample. Below are the steps to do this for both base developing and non-base developing resists

Positive Resist/Solvent developer:

1. Spincoat your resist onto your sample.
2. Evaporate about 10nm of Al directly on the resist.
3. Expose pattern directly after prior step to avoid Al oxidation that diminishes the metal's conductivity.
4. Before developing, wash the Al off the sample with TMAH.
5. Proceed to develop as normal.

Negative Resist/Base developer:

1. Spincoat your resist onto your sample.
2. Spincoat PSS (a mix of 99% poly(4-stryenesulfonic acid) and 1% Triton X-100 surfactant) for 1 minute at a rpm of 3000.
3. Bake PSS for 5 minutes at 90 degrees Celsius.
4. Evaporate about 10 nm of Au on sample.
5. Expose pattern.

6. Remove PSS and Au layer with 1 minute water bath.
7. Proceed to develop as normal.

General Tips and Tricks with Resists

It is always important to clean your sample. Not only can an unclean sample lead to unwanted errors on your desired pattern, but improper cleaning can also affects your resist adhesion which will lead to a very frustrating troubleshooting process. Here are some generally cleaning guidelines

Cleaning Glass:
Sonicate with acetone for 5 minutes followed by an IPA wash and N_2 dry. In order to get resists to adhere, do not use O_2 plasma to clean glass followed directly by a resist deposition step.

Cleaning Si:
Beyond the most basic clean of acetone and IPA in a spincoater, there are a few other common glass cleaning methods. The first is Piranha which consists of H_2SO_4 and H_2O_2 at a 5:1 ratio. To clean in Piranha, dip the sample in the piranha form 15 minutes then rinse with water, then acetone, then IPA. Another option is to use nanostrip which also removes organics from your substrate. You can lightly heat the nanostrip and rinse your sample for 15 minutes. Be careful to never boil nanostrip as the fumes generate from that are incredible toxic, flammable, and overall dangerous. The most intensive cleaning is RCA cleaning. It is the most time involved, but also the best for removing both organics and inorganics from your surface.

Here are some additional resist tips:

1. Always check the resist manufacturer’s website for proper spincoating and sample prep instructions. They generally have a well written step-by-step procedure.

2. Make sure your resist is evenly coated. If it is not, start over immediately. You do not want to continue your nanofabrication process when the resist is unevenly coated because you will only further complicate your troubleshooting.
3. After developing, always take care to wash off all of the resist. Do not skip any post-development rinsing steps as remaining resist can harm your etch process.
4. A lot of resists like PMMA require a pre-bake before applying the resist. Do not skip this step; it is very important to the adherence of your resist.
5. When heating a chip, put the sample on the hot plate directly, do not put it on glass as glass is insulating and the heat will not fully reach your sample.
6. To attach polymers to glass, HDMS is a good tool. Place some HDMS in a vial cap and place the cap and your sample in a vacuum sealed container. In many cases, this is the only way to get a polymer to stick to glass.
7. I had a lot of trouble with ma-N240r adherence. I found that the best method to get it to adhere was a prebake on my chip for 2 minutes at 180 degrees Celsius before spincoating the resist.

A.4 Etching

Etching is likely the step you will spend the most time perfecting. Etching is often specific to your own samples and desired patterns. Therefore, this section will just be an overview of different etching techniques followed by a list of etching tips and advice.

Etching falls under two categories: wet or dry. Wet etching is cheap and has fewer parameters. This means that the user generally does not have much control over the structures as the only parameters adjusted in a wet etch are the chemical ratios and the time of the etch. If you are making intricate structures at the nanoscale, you will more than likely not be using a wet etch to make your structures. Wet etching is less direct and can also cause stiction, or an adherence of layers within your structure. Common wet etchants are HF (which etches SiO_2 and many semiconductors), KOH (etches semiconductors like Si and GaAs), TMAH (etches metals), EDP (etches Si), and other high concentration acids and bases. When using HF, make sure you have accurately accounted for the buffering percentage as that will drastically affect your etch rate. If you are trying to wet etch intricate structures, depending on the crystallinity of your material, KOH, TMAH and EDP can show some directional preference.

If you are working in nanofabrication, you will be substantially more likely to use a dry etch process. Figuring out the best etch for your structure will likely be a bit time consuming. I would recommend before your training to look up how other people have etched your material. Look into the gases, pressures, etc. to find a good starting point. There are a few common etches. The first is a Bosch process which works via gas switching alternating between etching and protective gases. This helps you make structures with periodicity of non-uniformity in the z-direction. I have primarily used a pseudo-Bosch process where you apply both gases at the same time to get straight sidewalls. The final etch is a cryo-etch. This is typically needed if you are etching thick structures and want to retain uniformity. The cold temperatures provide strong selectivity with lower etch rates. This is also what you will need for tapered structures. When using a dry etch process, the parameters you control are the gases used, flow rate, forward power, ICP power, pressure, and temperature. I have found that colder etches help in creating sleek sidewalls, but this is an upper limit on how cold you go before you start compromising your resist. Same goes for pressure. Lower pressures created better sidewalls, but when I went below 6 mtorr in my process, I would see that the resist was no longer staying resilient in the etch causing tiny structures. You will likely hear people refer to hard masks and soft masks. Soft masks are what I have used in this thesis where I rely on the resist alone to create the properly etched pattern. A hard mask is when you use some type of deposited metal, like Cr, as a resist. This generally will make your structures more durable and is often required if you are etching thick structures or thick structures with narrow features.

Here are some final tips on etching:

- Thin film etch rates and nanostructure etch rates are not the same. A thin film will always etch faster than a pattern.
- Do not get mixed up between a Direct Reactive Ion Etcher (DRIE) and a Plasmatherm Reactive Ion Etcher (RIE). A DRIE has a wider ranges of gases and powers and is the only way to get desired structures and features. RIE is good for O_2 plasma, sample cleaning, and removing layers of uniform material. I also use the RIE to fully clean e-beam resists from my samples.
- Do not try to start an etch recipe from scratch. See if there are similar recipes in the machine as a start point.
- When checking your etch rate, use SEM over AFM. AFM tips cannot always perfectly give a profile when your features are close together.

A.5 Final thoughts for successful nanofabrication

- Always go into lab with a plan. Do not just start working haphazardly.
- When troubleshooting, only change one parameter at a time or else you will not know what went wrong.
- Do not be afraid to reach out for help. Chances are someone has faced a similar issue to you and has ideas on how to help.
- Start over early if you mess up. You do not want to have multiple failure points when optimizing or troubleshooting a process.
- Remember that the application is the cool part. There is no need to forgo all help or outsourcing because you want to do everything yourself. The unique part of your work is what your sample will ultimately do.